The Pennsylvania State University

The Graduate School

Department of Materials Science and Engineering

INVESTIGATION OF REDUCED $(Sr_x,Ba_{1-x})Nb_2O_6$ AS A FERROELECTRIC-BASED THERMOELECTRIC

A Dissertation in

Material Science and Engineering

by

Jonathan A. Bock

Submitted in Partial Fulfillment
of the Requirements
for the Degree of

Doctor of Philosophy

August 2016

The dissertation of Jonathan Anton Bock was reviewed and approved* by the following:

Clive A. Randall
Professor of Materials Science and Engineering
Dissertation Co-Advisor
Co-Chair of Committee

Susan Trolier-McKinstry
Professor of Ceramic Science and Engineering
Dissertation Co-Advisor
Co-Chair of Committee

Gerald D. Mahan
Distinguished Professor of Physics

Roman Engel-Herbert
Assistant Professor of Material Science and Engineering

Venkatraman Gopalan
Professor of Material Science and Engineering

Suzanne Mohney
Professor of Materials Science and Engineering and Electrical Engineering
Chair, Intercollege Graduate Degree Program in Materials Science and Engineering

*Signatures are on file in the Graduate School

ABSTRACT

A comprehensive study of a novel type of thermoelectric – a heavily doped material from a ferroelectric base composition – is presented. Due to the low-lying optic modes and scattering of phonons at domain walls, ferroelectrics make interesting candidates for thermoelectrics. The example of $(Sr_x,Ba_{1-x})Nb_2O_{6-\delta}$ (SBN) is explored in detail due to a report of an impressive thermoelectric figure of merit in single crystals. The goal of this research is to understand the source of the large figure of merit in SBN. In attempts to do this, the electron transport mechanism, the coupling between electron transport and ferroelectricity, the phase equilibria, and the single crystalline thermoelectric properties were investigated under various reduction conditions.

It was found that the electron transport properties of a normal ferroelectric SBN can be well explained by activation of electrons into the conduction band from a localized impurity band. SBN can be shifted between a normal and relaxor ferroelectric by changing the Sr:Ba ratio. This property of SBN was utilized to study the effect of relaxor ferroelectricity on electron transport. Within the relaxor ferroelectric regime, a change in the activation energy for electronic conduction and an abnormal temperature dependence of the Seebeck coefficient were found. These properties are attributed to Anderson localization caused by the relaxor ferroelectricity. This is not thought to be the cause of the large thermoelectric figure of merit.

The electron transport-ferroelectric coupling was also studied in oxygen deficient $(Ba_x,Sr_{1-x})TiO_{3-\delta}$ (BST). A metallic-like to nonmetallic transition occurs at the ferroelectric transition, and the temperature of the metallic-like to nonmetallic transition can be shifted via Sr doping. The temperature shift on Sr doping is equivalent to the shift in the paraelectric-ferroelectric transition temperature in unreduced samples, showing that the ferroelectric transition is the cause of the metallic-like to nonmetallic transition.

The presence of an impurity band in SBN points toward a large carrier concentration which is difficult to justify with oxygen vacancies alone, and this large carrier concentration is thought to provide the enhanced thermoelectric properties. To investigate the cause of the enhanced carrier concentration in reduced SBN, the defect chemistry and phase equilibria of the system under low oxygen partial pressure conditions was studied. A secondary phase of NbO_2 was identified upon reduction, and was found to correlate with an increase in the (Sr+Ba):Nb ratio of the SBN matrix. It will be shown that if the assumption is made that the excess Sr and Ba remain in the SBN lattice, then the (Sr+Ba):Nb ratio of the SBN matrix can accurately predict the amount of NbO_2 which forms. Additionally, the amount of NbO_2 secondary phase decreases on increasing the Sr and Ba concentration of samples. Eventually a phase pure composition is formed when the (Sr+Ba):Nb ratio corresponds to a Sr and Ba site occupancy of 1, $(Sr_{0.6},Ba_{0.4})_{1.2}Nb_2O_6$. Above this, a tertiary phase forms. These findings are consistent with the Sr and Ba sites being filled as a function of reduction. This A-site filling process is thought to be the source of the large thermoelectric figure of merit. To investigate the air-stability, thermogravimetric analysis was used to measure the oxygen absorption upon heating in air. The amount of oxygen which is absorbed was equivalent to the necessary amount to fully compensate the excess Sr and Ba. The resulting samples are insulating.

The thermoelectric properties of and the NbO_2 formation in reduced SBN single crystals were also investigated. The formation of NbO_2 was hindered due to the lack of grain boundaries which act as heterogeneous nucleation sites. The homogeneous nucleation energy prevented bulk NbO_2 formation until 10^{-15} atm pO_2 at 1300°C, two orders of magnitude below the oxygen partial pressure necessary in ceramics. This was overcome using a pre-anneal at 10^{-16} atm pO_2 followed by a re-equilibration at lower pO_2. The highest power factor measured at 600°C was 8.5

µW/cmK^2 resulting in a zT of 0.38 if polycrystalline values of the thermal conductivity are assumed. The previously mentioned low-temperature Seebeck anomaly caused by Anderson localization was found to exist along the polar *c*-axis, but not the non-polar *a*-axis. This further strengthens the idea that perturbations to the electron transport are caused by the ferroelectric polarization.

These results show that the thermoelectric properties found in SBN upon reduction are due to a change from $(Sr_x,Ba_{1-x})Nb_2O_{6-\delta}$ toward $(Sr_x,Ba_{1-x})_{1.2}Nb_2O_{6-\delta}$ and the resulting carrier concentration associated with the additional Sr^{2+} and Ba^{2+} cations on the A-site. Relaxor ferroelectricity perturbs the electron transport, but is not a cause of enhanced thermoelectric properties. This points toward A-site doped tungsten bronze materials in general as interesting thermoelectric materials. Future work revolving around decreasing the octahedral tilt angle, increasing the d-orbital overlap, and determining the necessity of ferroelectric-thermoelectric coupling in relation to thermal conductivity could result in further optimization within this new interesting family of thermoelectric oxides.

TABLE OF CONTENTS

LIST OF FIGURES

LIST OF TABLES

ACKNOWLEDGEMENTS

First, I would like to thank my advisors, Clive Randall and Susan Trolier-McKinstry. Without your help and advice I wouldn’t have been able to obtain this degree. I would also like to thank all of the members of the STM and Randall groups for your prolonged help over the years. I would also like to acknowledge the staff members who have helped me and taught me much – Jeff Long, Steve Perini, Nichole Wondering, Tim Klinger, Maria Dicola, and the rest of the MRI staff.

On a personal level I would like to especially thank Ryan Keech, Lauren Garten, and Charley Yeager for their deep friendship and helping me through difficult times.

I would also like to thank my immediate family. Mom, Dad, David – the environment you provided, the help you have given, the lessons I have learned from you, and the opportunities you have provided me have gotten me to where I am today. I am truly thankful.

This material is based upon work supported by the National Science Foundation, as part of the Center for Dielectrics and Piezoelectrics under Grant Nos. IIP-1361571 and 1361503. Financial support for this research was also provided by the United States-Israel Binational Science Foundation (BSF-Energy) grant number 2011510, and the National Science Foundation grant number DMR-1206518.

Chapter 1
Introduction and Motivation

Thermoelectrics provide the ability to convert heat into electrical power. Whether this heat be in the form of radiative heat of a car exhaust, the heat transfer to and from the ground during the day-night cycle, or from an aluminum smelter, the heat may be converted into electrical power to increase the efficiency of the system or bleed off power for other uses. Optimizing thermoelectrics in the form of increasing the Figure of Merit, zT, has been a long-fought struggle against the physics of electron/hole and thermal transport. This struggle has made many strides from developing techniques to nanostructure materials resulting in lower thermal conductivities to the utilization of band engineering to optimize the thermoelectric power. These strides have opened up applications for thermoelectrics in the spaces of solid state cooling, automotive waste heat recovery, and extraterrestrial energy supply.[1–3] Increased optimization of thermoelectrics will open up further applications in waste energy recovery. This optimization is not limited to increasing the nominal thermoelectric figure of merit, but includes also optimization of the cost per watt-hour and maximum usable temperature. Oxide thermoelectrics aim toward this with the goal of highly stable and low cost materials; key challenges include overcoming the limitation of low figures of merit. Despite the ability of many oxides to make adequate amounts of power from waste heat, the efficiency of oxides has been hindered by their high thermal conductivity. Strategies to overcome the high thermal conductivity of oxides include solid solution formation, introduction of ‘rattler’ ions, interface creation via spinodal decomposition, and more which all have had varying level of success.[4–6] A strategy presented here is the use of ferroelectric oxides. The low-lying optic modes found in many ferroelectric oxides and the scattering of phonons by domain walls may act as an adequate scattering mechanism for decreasing the thermal conductivity for oxides.[7, 8] Although the role of domain walls and optic modes in thermal conductivity has been studied, little is known about the effect of ferroelectricity on the transport of electrons. This is partially a consequence of the large majority of applications for ferroelectrics requiring minimization of the electrical conductivity, or ‘leakage’ as it is pejoratively named. The opposite is clearly required for thermoelectric applications, and here the study of ferroelectrics bathed in a veritable sea of electrons is undertaken. With optimization and ingenuity, ferroelectricity eventually may supply an oxide which allows the flow electrons like a crystal and scatters phonons like a glass. Through this dissertation, this concept will be explored in detail for the example of strontium barium niobate. A material which, along one direction, has reasonable power factors combined with the phonon scattering power of a glass.[9, 10] This combination makes for a formidable combination of properties which is worthy of the in-depth study allowed by an academic dissertation. As this dissertation will show, the physics, phase equilibria, and optimization of strontium barium niobate are nontrivial. The struggle against the physics of electron and thermal transport is accompanied by the clash between ferroelectric coherence and electrostatic screening, the dichotomous need for simultaneous order and disorder, and the difficulties of playing on the edge of stability. If you are entertaining this text, I presume you too are soon to be entwined in these dilemmas. Welcome.

Chapter 2
Background Information

2.1 Electron Transport

Knowledge of the band structure of materials is important for understanding the movement of electrons through a material, and hence it's transport properties. The band structure will help predict the electrical conductivity and Seebeck coefficient of materials and is the backbone of the field of thermoelectrics. In this section, the necessary information to understand electron transport models in d-orbital systems such as $BaTiO_{3-\delta}$ and $(Sr,Ba)Nb_2O_{6-\delta}$ will be discussed.

2.1.1 Band Structures in d-electron Systems

The first successful approaches toward understanding the electronic properties of solids came from the free electron model which assumes electrons do not interact with each other[11, 12]. The free electron model predicts many important aspects of materials such as the Wiedemann-Franz law (see 2.2.1), the temperature dependence of the heat capacity, the shape of the electronic density of states, and Ohm’s law. The free electron model fails in many aspects[13], but the most important here is its failure to predict the presence of band gaps or insulating materials. This is corrected by introducing perturbations which take into account the interactions between the electrons and the periodic potential of the lattice – the nearly-free electron model[14]. This works well for ‘simple’ metals (non-correlated metals) and a wide range of other compounds containing non-transition elements (e.g. silicon, as an important example), but fails in many transition metals and transition metal oxides because the nearly free electron model does not take into account all aspects of electron-electron correlations[15]. A clear way to understand band structures in these correlated electron systems is through the extension of molecular orbital theory.

Molecular orbital theory describes the formation of molecular orbitals from hybridized atomic orbitals. That is, the atomic orbitals of individual atoms hybridize when forming a molecule, and the resulting filled hybridized orbitals, the molecular orbitals, are lower in energy than the individual atomic orbitals. The molecular orbitals can be determined via linear combinations of the atomic orbital wavefunctions. This is shown schematically in Figure 2-1 for a two hydrogen atoms forming an H_2 molecule.

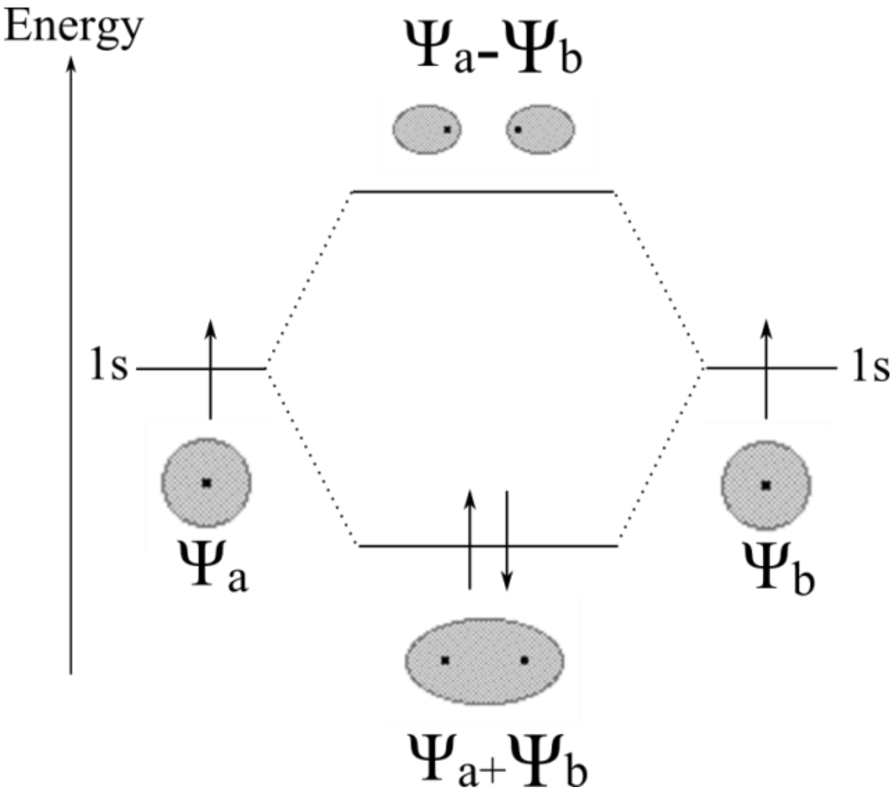

Figure 2-1. A depiction of molecular orbital theory for two hydrogen atoms bonding to form one hydrogen molecule. The molecular orbital which is a sum of the individual wavefuctions is at a lower energy than the individual wavefunctions. (Redrawn from [16])

This idea can be extended to larger molecules, and in this way one can think of a solid as essentially a giant molecule. The evolution from one individual atom with a singular orbital energy toward a bulk solid with increasing numbers of molecular orbitals and, eventually, a band of electronic states is shown in Figure 2-2.

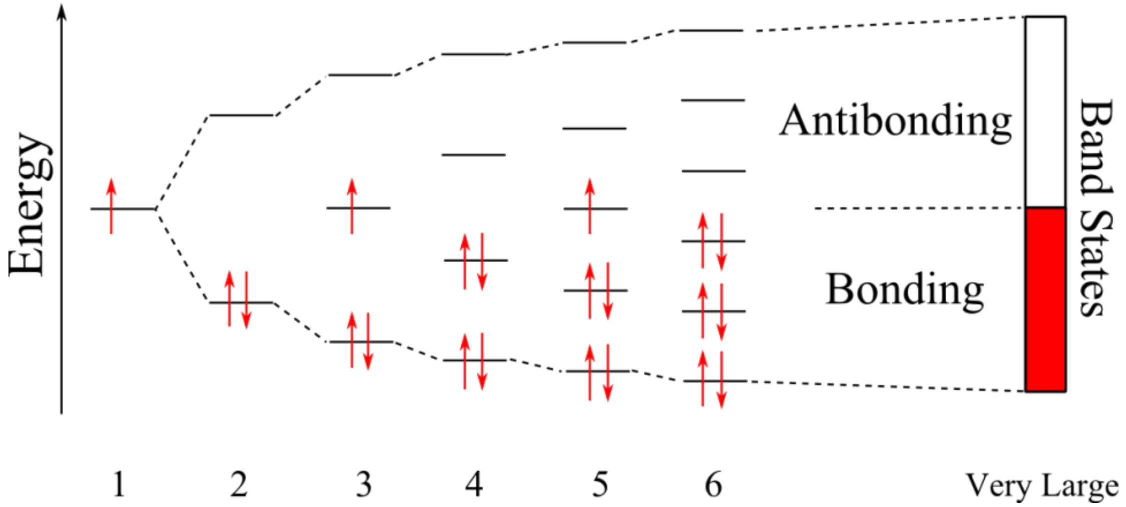

Figure 2-2. A depiction of band formation from a molecular orbital perspective. The number of atoms participating in bonding is shown on the bottom. The extreme case is shown on the right where a very large number of atoms participate in bonding and enough molecular orbitals are formed that a band of states develops. Redrawn from [17]

A given band will be mainly derived from the formation of molecular orbitals from specific atomic orbitals. In other words, a band will have a character of the atomic orbitals it is made out of, such as the 3d band or 2p band. Only orbitals which are close in proximity will hybridize, meaning that orbitals buried within the core of the atom will not hybridize, and so will not participate in bonding.

The bandwidth, W, defined as the energy difference between the highest energy state and lowest energy state in a band, increases with increasing orbital overlap. Because of the relatively small radius of the wavefunction, d-electron systems in general have smaller overlap and narrower bandwidths.[18]

Another important perturbation to transition metal oxide band structures is the fact that the bands are formed under the influence of anisotropic crystal fields, described in detail in [19, 20] and in summary here. For a d-orbital in a gaseous atomic species all of the d-orbital states are of equal energy. This five-fold degeneracy is lifted once the orbitals are placed in a crystal lattice. For a transition metal oxide this is because the metal cation is surrounded by multiple negatively charged ligands. Close proximity of the orbitals to these negatively charged ligands increases the energy of the electrons. As all of the d-orbitals have different shapes, they will have differing proximities to the ligands resulting in different energies, thereby lifting the degeneracy. Figure 2-3 shows the different d-orbitals of a metal cation in octahedral coordination.

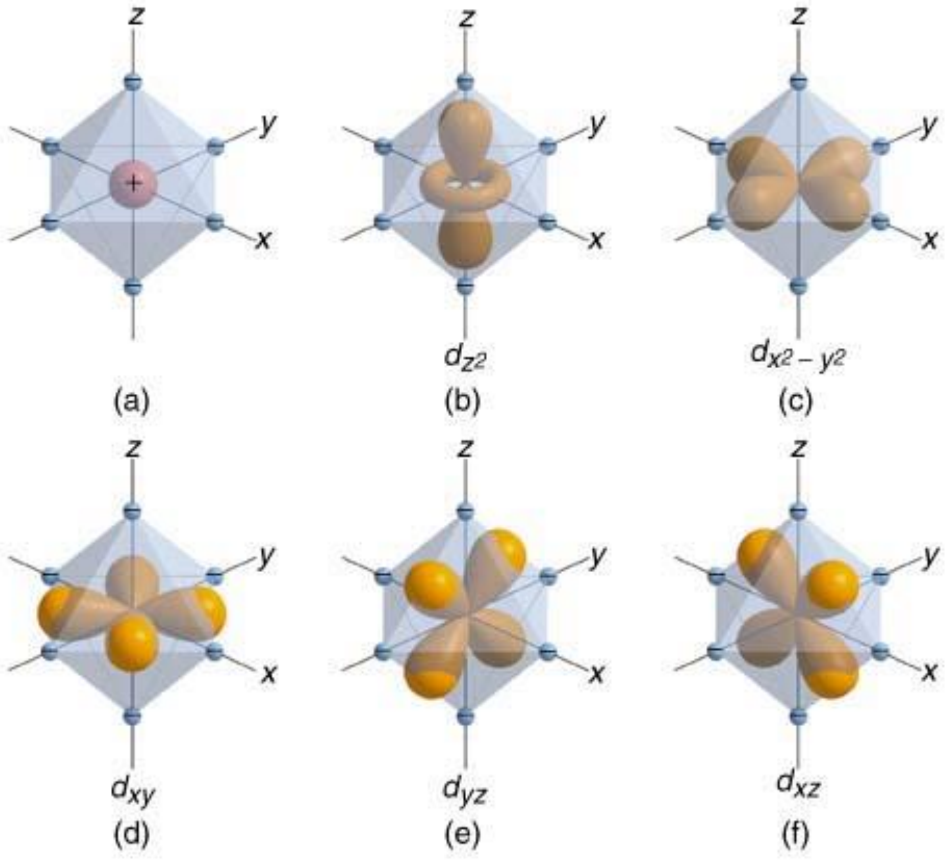

Figure 2-3. Different d-orbital electron clouds placed inside of an octahedral coordination of negative ligands. From Reference [17]

For octahedral coordination, the orbitals with high electron density near the ligands are the d_{z^2} and $d_{x^2-y^2}$ orbitals (Figure 2-3b and c), while the d_{xy}, d_{yz} and d_{xz} orbitals (Figure 2-3d-f) point in-between the negative ligands, resulting in lower energies. This causes an energy difference between the orbitals of Δ as depicted in Figure 2-4. The value of Δ depends on the ligands, the interatomic separation distances, and the geometry.

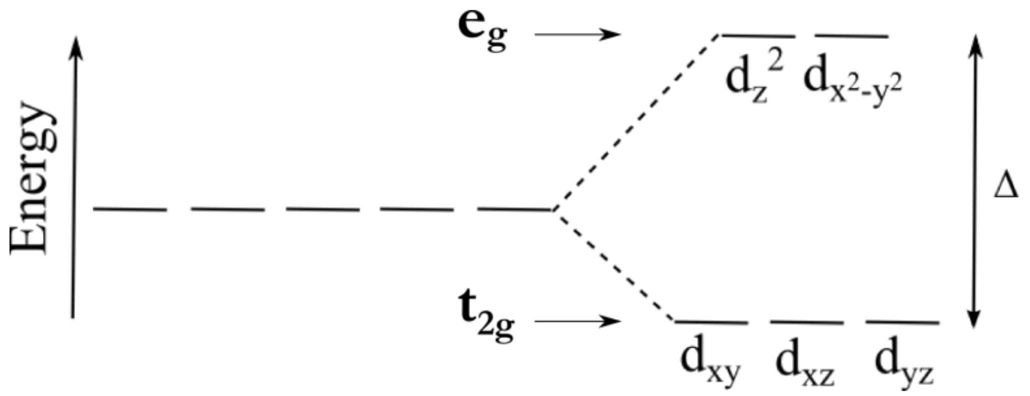

Figure 2-4. Crystal field splitting for octahedral coordination. Redrawn from [17]

This energy splitting manifests itself in the band structure and can split the bands into multiple sections, often labeled by their symmetric similarities, e.g. the – e_g and t_{2g} states in the case of octahedral coordination.

Another affect that becomes important in transition metal oxide systems, and especially systems with narrow bandwidths, are correlated electrons. Correlated electrons are electrons which must alter their motion so as to avoid each other due to their mutual Coulombic repulsion. For most purposes it is appropriate to use an approximation which neglects the repulsion of electrons unless they are on the same atom. That is, the Coulombic repulsion of interest here is between two electrons which occupy the same orbital. This repulsion manifests as an additional energy required to place an electron in an orbital that is already occupied – similar to the idea of Hund's rule of maximum multiplicity. From a band structure perspective this takes a range of electronic states made via an orbital and splits that density of states into two sections separated by an energy U, referred to as the Hubbard U. Normally an electronic band has 2n electronic states where n is the number of orbitals participating in the band formation, but in the case of a Hubbard band only n electronic states are available and a nominally half-filled band will split into a lower filled band and an upper unfilled band, referred to as the Lower Hubbard Band (LHB) and Upper Hubbard Band (UHB), respectively. This means that a normally metallic conductor will become an insulator with an activation energy equal to the gap between the LHB and UHB.[15]

2.1.2 Anderson Localization and Mobility Edges

Anderson localization, named after P. W. Anderson who first explained the phenomenon[21], is associated with the localization of electrons in materials due to disorder. The phenomenon has been shown to be quite general for wave physics and has been identified for many disordered systems[22, 23], this discussion will be limited to the application of Anderson localization to electronic band structures. This discussion is a combination of the discussions from References [24–27].

Consider a set of cations in an ionic solid with no disorder. This ordering means that all of the cations have identical local structure and therefore their associated orbitals have identical energies, including identical crystal field splitting. The cations are close enough in energy and proximity so that the outermost orbitals slightly overlap and hybridize as described in 2.1.1 to form a narrow band as shown in Figure 2-5.

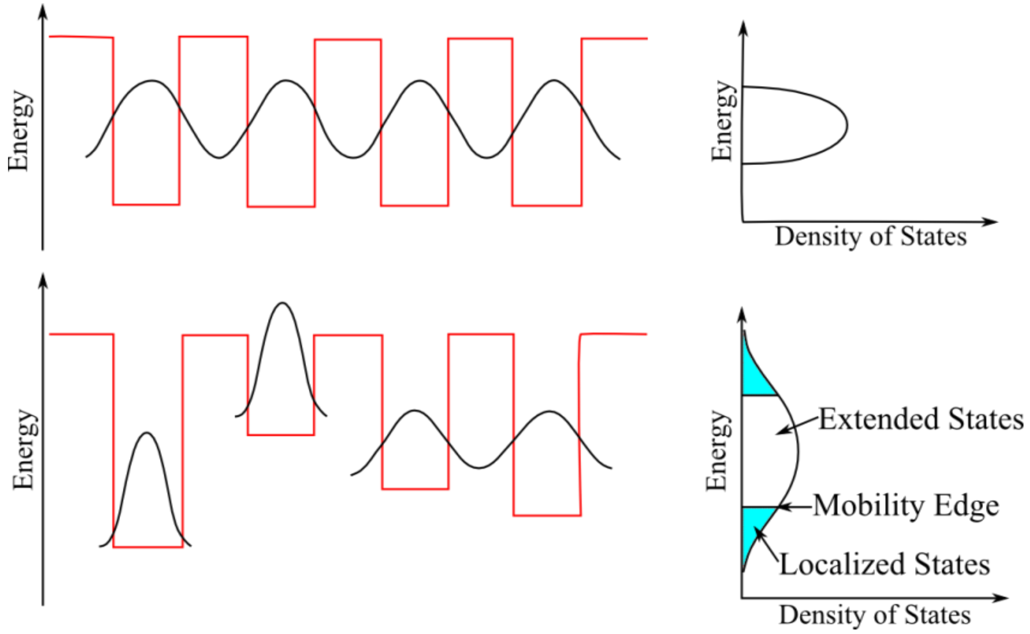

Figure 2-5. Depiction of Anderson localization. (a) Energy wells in an ordered material hybridize to give a parabolic density of states. (b) Energy wells in a disordered material where Anderson localization produces localized states at the edge of the band. Electrons in localized states move via hopping between localized sites, while electrons in extended states are delocalized. These states are separated by the mobility edge. Modified from Ref. [19]

If impurities are introduced into this perfectly ordered crystal, then the size and charge of the impurity will have to be accommodated by the crystal. This occurs via strain and dielectric displacement in the lattice. The cations around the impurity will have a local structure which deviates from the perfect lattice and therefore the orbitals on these cations will have slightly different energies and crystal field splittings. At large impurity concentrations, individual cations may feel the influence from multiple impurities, and the energies of the orbitals will depend on the summation of these multiple perturbations. As impurity density increases, the energy landscape for these orbitals becomes more disordered with larger and sharper peaks and valleys. Hybridization of orbitals can only occur when orbitals are close in proximity and in energy. Orbitals which are heavily perturbed with no surrounding orbitals with similar energies cannot hybridize to form a band, and therefore become localized. That is, once the peaks and valleys of the energy landscape become too different in energy compared to their surroundings they will have no surrounding cations to form bands with and will localize. The density of states is simply the integration of this energy landscape over energy, and from this density of states perspective the increasing disorder results in the broadening of the density of states as depicted in Figure 2-5. The localized orbitals are located near the band edges and their localization is depicted by shading in the density of states.

There exists an energy at which states switch from localized to delocalized. This is called the mobility edge and is a sharp transition at an energy E_m. At low amounts of disorder, localization will occur only at the band tails, but as disorder increases the mobility edge will move inward toward the center of the band.

Electrons below the mobility edge will conduct via hopping conduction between the localized states as described in 2.1.4. Electrons in energy states above the mobility edge will conduct via band conduction and therefore will have much higher mobilities. If the Fermi energy, E_f, is located below the mobility edge, E_m, either in localized states or within a band gap, electronic conduction is often controlled via activation of electrons to the mobility edge by[28]:

$$\sigma = \sigma_{min} exp\left(\frac{-\left(E_m - E_f\right)}{k_b T}\right) \tag{2.1}$$

where σ_{min} is the minimum metallic conductivity and depends on many factors including the distance between impurities and the critical disorder needed for localization. A detailed discussion of σ_{min} can be found in reference [28]. Often the Fermi energy may be pinned to the location of the band edge, as in the case of impurity bands (discussed in 2.1.3). If this is the case, then the activation energy will depend on the temperature dependence of the band gap, and [29]:

$$E_m - E_f = E(0) - \gamma T \tag{2.2}$$

where

$$\gamma = \frac{dE_g}{dT} \tag{2.3}$$

and E_g is the energy of the relevant band gap. An example of this behavior will be shown in Chapter 4 (4.3).

2.1.3 Impurity Bands and the Transition to Metallic Conductivity

The same principal of overlapping orbitals leading to band formation discussed in 2.1.1 can be applied to donor or acceptor dopants. In heavily doped materials, the dopants can be close enough in the lattice so their orbitals overlap and form an electronic band. This may seem odd as 2.1.1-3 discusses effects of *decreased* bandwidth due to the poor overlap of orbitals on ions only a couple lattice sites apart. Unlike electrons in d-orbitals where the majority of the electron density is relatively localized around the ion, the valence electrons of donors can often have large effective radii because the electron of a donor can be screened from the donor ion via the surrounding lattice.[30] The radius of a spherical donor orbital is called the effective Bohr radius, and is given by[30]:

$$a_{eff} = a_o \frac{\varepsilon_r}{m^*} \tag{2.4}$$

where a_{eff} is the effective Bohr radius, a_o is the Bohr radius of hydrogen (53pm), ε_r is the relative permittivity of the host, and m^* is the effective mass of the electrons in the host. Essentially, the effective Bohr radius corrects for the screening and changes to the electron effective mass provided by the lattice.

The permittivity and effective mass in Equation (2.4) should be discussed in more detail for ferroelectrics. The static dielectric constant is normally used for ε_r in Equation (2.4), but the equation is most commonly used for materials where the static permittivity is synonymous with the sum of the ionic and electronic portions.[31] This may not true in ferroelectrics as the ‘static’ dielectric constant in a ferroelectric would include a contribution from dipolar rotation. The static permittivity is, however, used to accurately calculate the effective Bohr radii in $SrTiO_{3-\delta}$ [32], suggesting that the large ionic permittivity of ferroelectrics is the parameter of interest. This can be obtained for ferroelectrics by using broadband dielectric spectroscopy to measure the permittivity once the dipolar contribution has relaxed at high frequencies, e.g. Ref. [33].

For a better understanding of how impurity bands affect electronic conduction, consider the transition from an insulating material to a metallic conductor via an impurity band as a function of carrier concentration, as depicted in Figure 2-6. This will be done for an n-type material with an impurity which provides one ionizable electron.

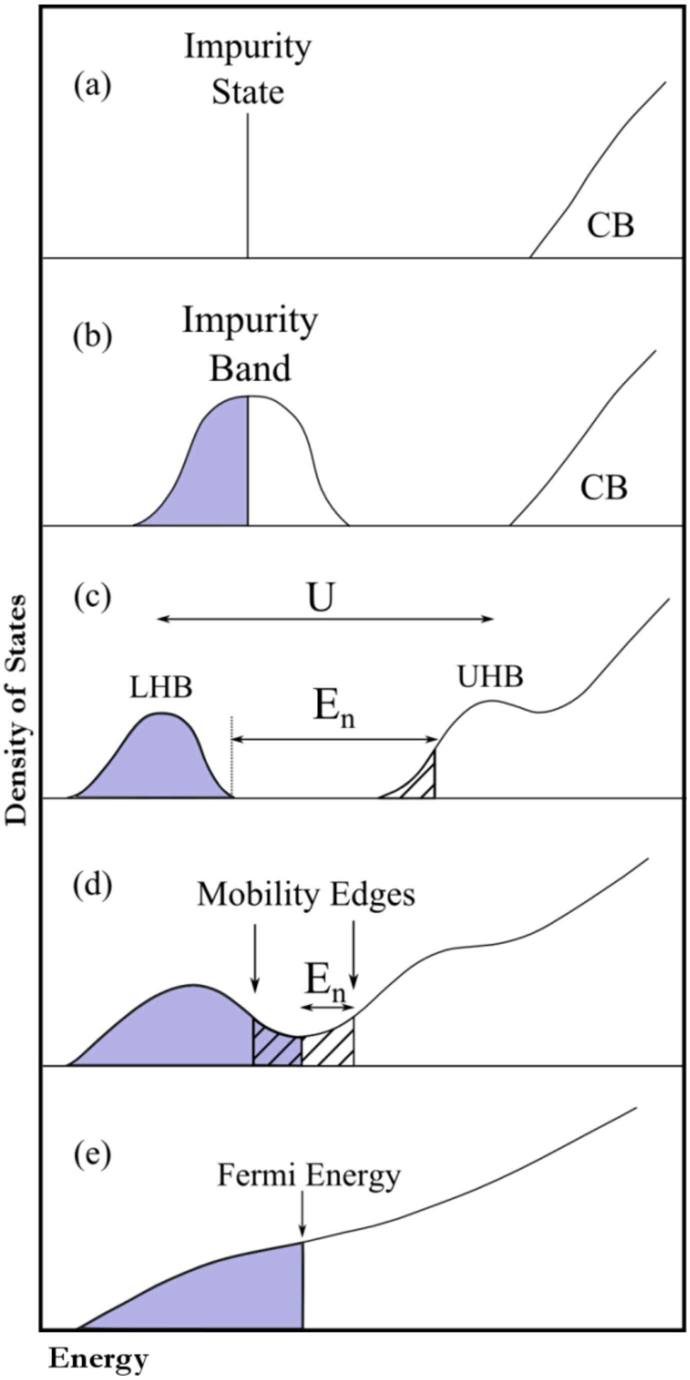

Figure 2-6. Depiction of the transition from insulator to metal as a function of carrier concentration. (a)-(e) are described in the text. Inspired by Ref. [19]

At very dilute impurity concentrations, the impurities are far enough apart that interaction between the different impurities can be ignored. Each impurity will behave independently and will have a very sharp donor energy level (Figure 2-6a). As the impurity concentration increases, the overlap of the donor valence electrons will lead to the formation of an impurity band below the conduction band. Nominally this would be thought of as a half-filled band with the band centered at the donor ionization energy (Figure 2-6b); however, Coulombic interaction between the electrons leads to a Hubbard gap as discussed in 2.1.2. This results in one fully occupied LHB and one unoccupied UHB with a separation of U (Figure 2-6c).

The magnitude of U is difficult to ascertain from first principals for electrons in d-orbitals, although the 'screened' U can be calculated if under certain assumptions [34]. For hydrogenetic orbitals, U can be estimated as [28]:

$$U = \frac{5}{8}\frac{e^2}{\varepsilon * a_{eff}} \tag{2.5}$$

or

$$U = \varphi - \xi \tag{2.6}$$

where φ is the ionization potential and ξ is the electron affinity. For donors a_{eff} is [30]

$$a_{eff} = \frac{e^2}{2\varepsilon E_d} \tag{2.7}$$

where E_d is the donor ionization energy. Comparing Equation (2.7) to Equation (2.5) shows that, for hydrogenetic donor orbitals, the Hubbard U for impurity bands should be on the order of the donor ionization energy. Since the center of the Hubbard bands is located at the donor ionization energy and the UHB is located at roughly U/2 above this energy, the UHB should lay close to the bottom of the conduction band as depicted in Figure 2-6c.

In Figure 2-6c the LHB is completely filled while the UHB is empty, resulting in a Fermi energy lying between the two and, therefore, an insulating state. In this case electrical conduction is thermally activated with an activation energy equal to the difference between the bottom of the UHB and the top of the LHB. If Anderson localization is present, the activation energy would be between the mobility edge and the top of the LHB.

As impurity concentration increases further, the density of states in both the UHB and LHB increase and spread out. The band gap thereby shrinks and the activation energy for electronic conduction decreases. Eventually the UHB and LHB overlap and the Fermi energy is therefore located within electronic states. When the overlap first occurs the states are localized via Anderson localization and therefore the activation energy for conduction continues to be the difference between the mobility edge and the Fermi energy. Since the Fermi energy lies in Anderson localized states, at low temperatures electrical conductivity will be via variable range hopping and at intermediate temperatures conductivity will proceed via polaronic hopping.[35] As impurity concentration increases further again, the mobility edges will move toward the Fermi energy and eventually the Fermi energy will be located in delocalized states as depicted in Figure2-6e. Once this occurs, the material is a metal.

The insulator-to-metal transition is not abrupt, but is manifested as a decreasing activation energy with increasing carrier concentration until the activation energy becomes zero. For example, Figure 2-7 shows the transition from semiconducting to metallic behavior in $La_{1-x}Sr_xVO_3$. As the strontium concentration increases, the activation energy drops until metallic behavior occurs at x~0.2. [36]

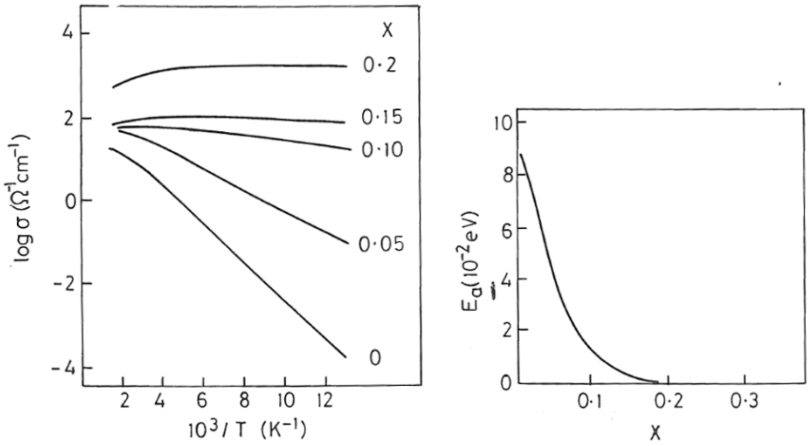

Figure 2-7. (a) Conductivity vs. temperature data and (b) activation energy for $La_{1-x}Sr_xVO_3$. The activation energy at x~0.2 goes to zero, indicating metallic behavior. [36]

The semiconducting to metallic transition, from (d) to (e) in Figure 2-6, can be predicted. In theory, the transition should occur when the donor orbitals overlap a specified amount; this can be estimated by comparing the effective Bohr radius, Equation (2.4), and the distance between donors. Given a three dimensional lattice, the distance between impurities is proportional to the cube root of the concentration[37]:

$$d \propto n^{1/3} \tag{2.8}$$

where d is the distance between the donor ions, and n is the concentration of donors per volume. The necessary amount of orbital overlap was determined empirically and is denoted the 'Mott criterion' for metallic conduction. It is given by[28]:

$$0.26 \sim a_{eff} n^{1/3} \tag{2.9}$$

The universality of this law was shown by Edwards and Sienko [37] and their compiled dataset along with a few additions from recent years is shown below:

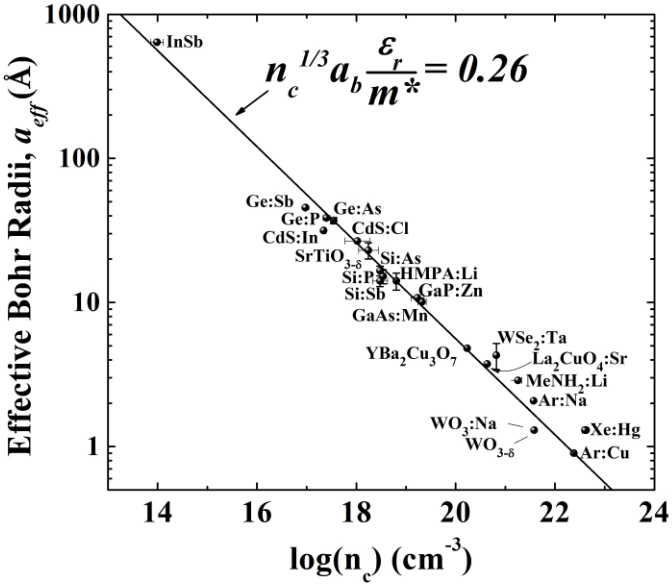

Figure 2-8. The effective Bohr radius and the critical carrier concentration for metallic conduction plotted for a variety of materials. The solid line represents the Mott Criterion, and is shown to fit well for many materials. $WO_{3-\delta}$[38]; $SrTiO_{3-\delta}$[39, 40]; $YBa_2Cu_3O_7$ and $La_{2-x}Sr_xCuO_4$[41]; all other points from Ref. [37]

Difficulties in putting more data points on Figure 2-8 are mainly associated with accurate determination of the effective Bohr radii. For ferroelectric materials specifically, the measurement of the correct relative permittivity can be a problem. That is, the correct relative permittivity will not be the normally measured low frequency relative permittivity, but is more likely the sum of the electronic and ionic contributions. This sum can be measured at high frequencies where the dipolar rotation contribution to the permittivity has relaxed, but must be below the relaxation frequency for phonons. This is sometimes possible with THz spectroscopy, e.g. see Ref. [42]

2.1.4 Polaronic Hopping

In ionic materials, electrons will often be localized by deformation of the surrounding lattice caused by the charge carrier. Although materials with large carrier concentrations and small band gaps are often controlled by band conduction as discussed in previous sections, at low temperatures and at low carrier concentrations polaronic hopping may be of importance. This section explains how polaron formation and hopping occur, along with ways to identify polaronic hopping and its impact on electronic transport in oxides.

Consider an ionic material in which all of the ions are on their proper lattice sites but are pinned so they may not move. Now consider the introduction of an 'impurity' electron placed into the material. This electron is not necessarily associated with an ion as is commonly portrayed (e.g. Ti^{3+} on a Ti^{4+} site), but is a free electron. In the surrounding area the neighboring ions will feel a Coulombic force from this negatively charged impurity electron, but will not move due to this force because they are pinned to their perfect lattice sites. If a test charge is placed at a radius of distance r away from the negatively charged ion, the potential energy, V, which acts on the test charge would be[31]:

$$V(r) = \frac{e^2}{\varepsilon_\infty r} \tag{2.10}$$

where ε_∞ is the high-frequency relative permittivity of the material. Only the electronic polarizability is included in ε_∞ as ionic motion is frozen. Now if the ions are allowed to relax, then the positive ions will move toward the negatively charged impurity electron and negative ions will move away. A series of dipoles aligned radially around the impurity electron form. Stabilization of the system in this way lowers the electron into a potential well, thereby stabilizing this state. If Equation (2.10) is re-evaluated given the relaxed lattice then ε_s, the static relative permittivity, must be used instead of the high-frequency relative permittivity. The electron therefore forms a potential well for itself given by:

$$V(r) = \frac{e^2}{r}\left(\frac{1}{\varepsilon_\infty} - \frac{1}{\varepsilon_s}\right) \qquad (2.11)$$

where ε_s is the static relative permittivity. Normal theory assumes ε_s includes only the electronic and ionic portions of the permittivity, but, as discussed previously, this may be modified for ferroelectrics. The presence of this potential well means that if the impurity electron tries to move away from its current position, it will have to overcome the potential barrier described by Equation (2.11). In materials with low ionicity, the dipoles formed during lattice relaxation are small, the potential barrier is therefore small, and this scenario is best described by an increased effective mass of the impurity electron. The impurity electron combined with the resulting lattice deformation is known as a 'polaron'. In the case presented where the potential barrier is small, it is known as a 'large polaron'[31]. 'Large' here refers to spatial extent, since the small ionicity requires a large distance to completely screen the negative impurity charge. If the iconicity is large, then the potential well is large and the electron becomes trapped on the site. As the electron itself is what causes the formation of the surrounding dipoles in the ionic lattice, it has in essence 'dug its own hole' to form this trap. Since the electron is trapped to a single site and the lattice deformation is small in spatial extent, this is known as a 'small polaron'. Small polaron formation is facilitated in materials with highly polarizable lattices and narrow bandwidths. These trends can be understood as follows. In a small polaron, the localized electron is stabilized by the ionic polarization by roughly the depth of the potential well of Equation (2.11) which increases with increasing ionic permittivity. The stabilization energy gained by an electron entering a band is the energy difference between the atomic orbital energy and the energy of the electron at the bottom of the conduction band – roughly W/2, where W is the bandwidth. Out of these two scenarios the one which lowers the energy of the electron the most will occur. Therefore, highly ionizable lattices will push toward polaronic formation via the increase in magnitude of Equation (2.11), and narrowing the bandwidth will push toward small polaron formation as W/2 decreases.[43] As ferroelectricity tends to occur in some highly polarizable oxides, all references to polarons from here on in this thesis will refer to small polarons. For more information on large polarons, an interested reader can refer to Ref. [44].

Both the electron and the corresponding lattice deformation must move for movement of the small polaron to occur. To better understand this, it is key to consider the timescale at which electrons and lattices move. Electrons move at much faster speeds than ions, as is easily seen in the different relaxation times for the electronic and ionic portions of the permittivity, for example. From the perspective of timescales important to electron motion, the lattice is a static object (and therefore the trapping potential, Equation (2.11), is static). From the perspective of timescales important to lattice motion, the time-averaged position of the electron will be at the center of the potential well. Movement of the small polaron is therefore not often facilitated by the electron itself, but by deformations in the local lattice due to phonons or by excitement of the electron via optical means.

The polaronic potential well can be perturbed by phonons in the material, some of which will decrease the potential well to a degree where the electron can escape via thermal excitation. This process is shown schematically in Figure 2-8, adapted from Ref. [44].

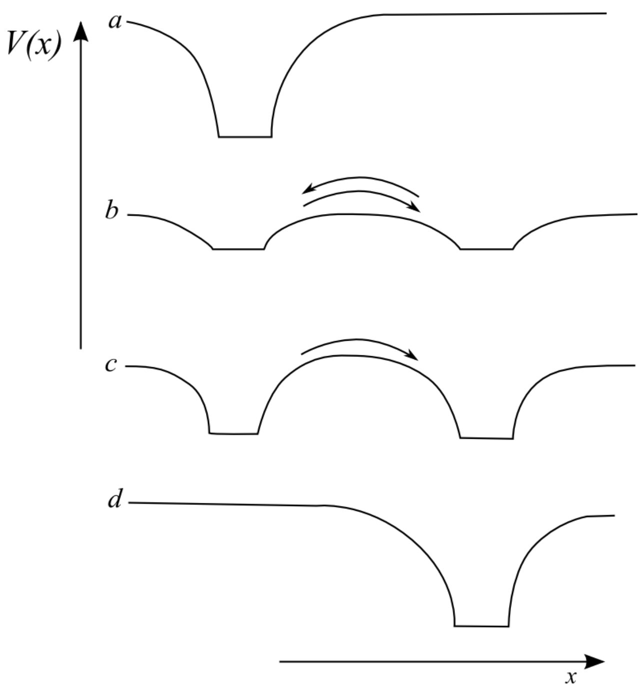

Figure 2-9. Polaronic potential wells (a) before hopping (b) during adiabatic hopping (c) during non-adiabatic hopping and (d) after hopping. After Reference [44].

Figure 2-9a shows a schematic representation of an electron trapped in the polaronic potential well. A transient phonon can perturb the lattice, thereby decreasing the polaronic potential well and often creating a potential well on a neighboring site as depicted in Figure2-9bc. The electron can therefore hop from one site to the other via thermal activation or tunneling. If the length of time the transient phonon is located near the small polaron is long compared to the length of time it takes for the electron to thermally activate into the neighboring potential well, then the electron will hop between its current position and the neighboring site multiple times before the transient phonon leaves, as depicted in Figure 2-9b.[45] This condition is called the adiabatic condition. If the activation energy between the two neighboring sites is large and the electron only has time to hop into the neighboring potential well, but not back and forth multiple times, then a nonadiabatic state is reached as is depicted in Figure 2-9c.[45] If once the transient phonon leaves the electron is located on a different lattice site, the full polaronic potential well will reform around the electron as depicted in Figure 2-9d and electrical conduction has occurred.

The thermally activated electron mobility is a defining feature of small polaronic conduction. Thus, the experimental procedures used to determine if small polaronic conduction dominates (as opposed to band conduction) are aimed at determining if thermal activation in the electrical conductivity is due to thermal activation of new electronic carriers or due to the thermal activation of the mobility of those carriers.

The mobility of a small polaron is thermally activated and given by[31]:

$$\mu = \frac{A}{T^n} exp\left(\frac{-E_{Hop}}{k_b T}\right) \tag{2.12}$$

where n=1 or 3/2 for the adiabatic and non-adiabatic conditions, respectively. Wide band gap materials, such as many oxides, have a temperature independent carrier concentration and therefore the temperature dependence for electrical conductivity will follow the form of Equations (2.12) or (2.13). In these cases, polaronic conduction can be determined via the linearity of ln(σT) vs $(k_b T)^{-1}$ plots. This temperature independent carrier concentration is also the cause for the temperature-independent Seebeck coefficient as will be discussed in 2.4.2. In materials with temperature dependent carrier concentrations, the identification of polaron formation is more difficult. However, it can often be done by comparing the Seebeck coefficient and electrical conductivity of a material. The activation energy for electronic conductivity, E_σ, is the summation of the activation energy for carrier creation and the activation energy polaron mobility[46]:

$$E_\sigma = E_n + E_{Hop} \tag{2.13}$$

where E_σ is the activation energy for electronic conductivity, E_n is the activation energy for new carriers (often the activation energy for donors or the band gap), and E_{Hop} is the activation energy for polaron mobility from Equation (2.12) . E_n can be obtained from Equation (2.54) and

E_σ from Equation (2.12), and any difference between the two is therefore associated with a finite E_{Hop} and indicates small polaron formation.

It is key to note that Equation (2.12) is only valid at temperatures above $\sim\frac{1}{2}T_{Debye}$[47]. This is because phonons are necessary for the movement of the electron out of the polaronic potential well, and below T_{Debye} phonon modes start to become deactivated. The polaronic potential well can be perturbed by either a single phonon or by the absorption of multiple phonons whose sum performs the same function, and if necessary followed by an emission of a phonon to dissipate the excess energy. This is depicted in Figure 2-10. These multi-phonon processes are the first mechanism to relax out below the Debye temperature; the result of this is deviation from Equation (2.12).

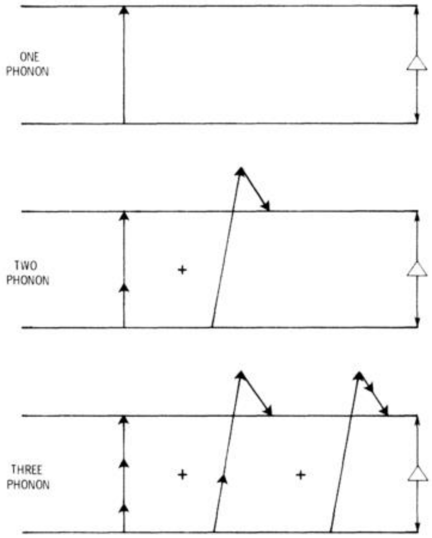

Figure 2-10. Schematic representation of different phonon absorptions leading to electronic hopping, including multiphonon absorption processes. From Ref. [47]

This is discussed in detail by Emin[47], and the result is a conductivity similar to Variable Range Hopping (VRH) (discussed below) with a similar characteristic $T^{-1/4}$ behavior at temperatures below $\sim\sim\frac{1}{2}T_{Debye}$.

Variable Range Hopping (VRH) is another important mechanism via which localized electron transport occurs. As opposed to traditional hopping conduction, where an electron will hop to the *nearest neighbor* site, hopping will occur over a variety of ranges in VRH. The envelope of the wavefunction for an electron in disordered states decays over some distance. Within that distance multiple sites may be available for hopping, but sites closer in distance and closer in energy are more favorable.[48] In a disordered material, the sites which are spatially close are not necessarily energetically similar, and therefore electrons may hop to a site that is further away but energetically similar, as depicted in Figure 2-11.

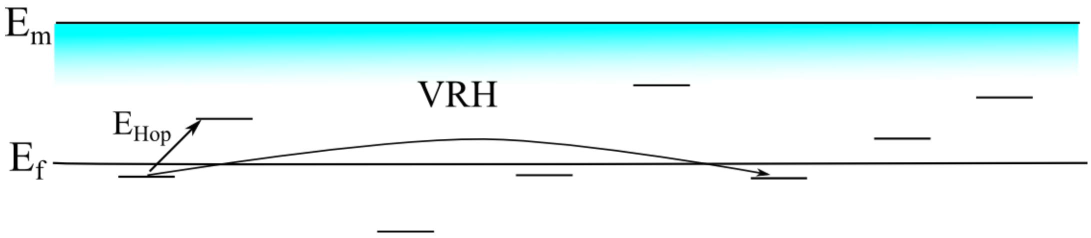

Figure 2-11. Schematic representation of Variable Range Hopping (VRH) compared to nearest neighbor hopping (E_{Hop}). All states below the mobility edge, E_m, are localized, as depicted by shading. After Ref. [49]

Due to the temperature dependence of the average hopping distance, the temperature dependence for this type of behavior follows[50]:

$$\sigma = Aexp\left(-T_oT^{-1/4}\right) \tag{2.14}$$

where A and T_o are constants.

2.2 Thermal Conductivity

The main mechanisms of thermal transport in dense materials are transport via electrons, phonons, or photons. Thermoelectrics are necessarily electrical conductors, typically making them opaque, which limits the mean free path of photons. The total thermal conductivity can therefore be broken down as:

$$\kappa = \kappa_l + \kappa_e \tag{2.15}$$

where κ is the thermal conductivity, κ_l is the lattice thermal conductivity (phononic transport), and κ_e is electronic portion of the thermal conductivity. When designing a thermoelectric, it is imperative to have enough electronic carriers to sustain a large power factor and therefore the electronic portion of thermal conductivity is necessary, but the lattice portion of thermal conductivity should be minimized.

To better understand thermal conductivity, it is instructive to derive the equation for thermal transport due to a set of particles and then consider the different cases for particles – electrons and phonons. The derivation presented here is taken from reference [51]. First, consider a gas where the temperature is a function of distance x so that $T=T(x)$. Now consider a plane in this volume at a constant x_p. The mechanism of heat transport will be via the movement of molecules across this plane. If $\frac{dT}{dx} > 0$ at this plane, then heat will travel in the direction of x, because the net energy of molecules crossing x in the positive direction is larger than the net energy of molecules crossing x in the negative direction. If a volume contains η molecules per unit volume (η is used so as not to confuse the value here with the electronic carrier concentration, n, although these will be an equivalent quantity when electronic thermal conductivity is discussed), then roughly one third of the molecules will have a velocity in the x direction as opposed to z or y. Roughly half of those will have a velocity in the $+x$ direction as opposed to the $-x$ direction. Therefore 1/6th of the molecules will be crossing the plane in the $+x$ direction at any time. Quantitatively, the number crossing the plane at x_p will be $\frac{1}{6}\eta v$ where v is the mean speed of the molecules. Since the temperature is a function of x, the energy of the molecule last equilibrated at x will have an energy $E = E(x)$. The energy of a molecule crossing this plane will therefore be determined by the location x of the previous collision of the molecule. Molecules crossing the plane have had a previous collision within one mean free path of the plane, and this means that molecules crossing the plane at x_p will have an energy $E = E(x_p \pm l)$ where l is the mean free path of the molecules. The net flux of energy over the plane at x_p, J_x, is therefore

$$J_x = \frac{1}{6}\eta v(E\left(x_p - l\right) + E\left(x_p + l\right))=\left(E\left(x_p - l\right) + E\left(x_p + l\right)\right) = \frac{1}{6}\eta v(\left(E(x) - l\frac{dE}{dx}\right) - \left(E(x) - l\frac{dE}{dx}\right)) \tag{2.16}$$

and

$$J_x = \frac{1}{6}\eta v\left(-2l\frac{dE}{dx}\right) = -\frac{1}{3}\eta vl\frac{dE}{dT}\frac{dT}{dx} \tag{2.17}$$

since $C_\eta = \frac{dE}{dT}$ where C_η is the specific heat *per molecule*. Equation (2.17) can be compared to the definition of thermal conductivity:

$$J_x = -\kappa\frac{dT}{dx} \tag{2.18}$$

from which the thermal conductivity of a dilute gas is:

$$\kappa = \frac{1}{3}C_\eta \eta vl \tag{2.19}$$

This formalism works well not only for thermal conductivity of gases but other particles or quasi-particles such as electrons and phonons. One simply has to switch out the heat capacity, number density, speed, and mean free path of the gas molecules with the equivalent values for electrons or phonons. Working through this formalism, it is also easy to grasp the different ways to control thermal conductivity, namely by engineering the different variables in Equation (2.19).

2.2.1 Electronic Thermal Conductivity

Electronic thermal conductivity is the portion of thermal conductivity which is transported via electrons. To determine the magnitude of heat transported via electrons, Equation (2.19) can be evaluated assuming the free electron model. In this case[52]:

$$v = v_f \tag{2.20}$$

$$ʆ = v_f * \tau \tag{2.21}$$

and

$$C_\eta * \eta = \pi^2 N_e k_b^2 \frac{T}{m^* {v_f}^2} \tag{2.22}$$

where v_f is the Fermi velocity, $ʆ$ is the mean free path of electrons, τ is the mean free time between scattering events, and N_e is the density of states.

Plugging the above equations into (2.19), the electronic portion of the thermal conductivity, κ_e, is found to be[53]:

$$\kappa_e = \frac{1}{2} {v_f}^2 \tau \pi^2 N_e k_b^2 \frac{T}{m^* {v_f}^2} = \frac{\pi^2}{3} k_b^2 \tau n \frac{T}{m^*} \tag{2.23}$$

Using the Drude formula[54]

$$\sigma = \frac{n \tau e^2}{m^*} \tag{2.24}$$

to substitute the electrical conductivity into Equation (2.23), yields:

$$\frac{k_e}{\sigma T} = \frac{\pi^2}{3} \frac{k_b^2}{e^2} \equiv L \tag{2.25}$$

where L is the Lorenz Number, 2.44x10^{-8} $\frac{V^2}{K^2}$. This relation between the electrical conductivity and thermal conductivity is called the Weidmann-Franz Law and works well for a wide variety of metals.

The Wiedemann-Franz law is very useful for metals, but breaks down if the free electron model is not applicable, as in the case in correlated metals or in nondegenerate electron gasses. Additionally, the Wiedemann-Franz law assumes that the relaxation times τ in (2.23) and (2.24) are identical, which is only true if electrons undergo elastic scattering events, and at low temperatures, inelastic scattering will occur and the Wiedemann-Franz law will be inapplicable.[55] Modification of the Wiedemann-Franz law has been determined for many cases, such as the previously mentioned nondegenerate gas example. The modification comes in the form of a modified Lorenz Number. Given parabolic bands, equalization of relaxation time for electrons and holes, and an energy dependent relaxation time proportional to E^{α} where α is a constant, it can be found that [56]:

$$\frac{k_e}{\sigma T} = \frac{{k_b}^2}{e^2}\left(\left(\frac{5}{2}+\alpha\right)+\left(5+2\alpha+\frac{E_g}{k_b T}\right)^2 \frac{n_e\mu_e n_h\mu_h}{(n_e\mu_e+n_h\mu_h)^2}\right) \tag{2.26}$$

where $n_{e,p}$ and $\mu_{e,h}$ are the carrier concentration and mobilities for electrons (e) and holes (p), respectively. Obviously, different modifications to L are necessary given different assumptions. For thermoelectric materials, it is important to note that a deviation from this treatment exists due to the Seebeck effect. Electrons will flow due to the thermal gradient and modify the Lorenz number. Using the Boltzmann transport equation it can be found [56] that:

$$L' = L - S^2 \tag{2.27}$$

where L' is the modified Lorenz number, L is the Lorenz number from Equation (2.25), and S is the Seebeck coefficient. In metals this is often inconsequential, since the Seebeck coefficient in metals is often only a few μV/K[57] making the square of the Seebeck coefficient roughly three orders of magnitude smaller than the Lorenz number (e.g. for Ag at 300K; $S^2 = 3.8x10^{-12}\frac{V^2}{K^2} \ll 2.44\text{x}10^{-8}\frac{V^2}{K^2} = L$), but for thermoelectric materials with larger Seebeck coefficients, the modification can become significant.

2.2.2 Lattice Thermal Conductivity

Thermal energy can be transported via quantized lattice vibrations known as phonons. Similar to the electronic thermal conductivity, the phonon thermal conductivity can be determined by using the thermal conductivity for a dilute gas and inserting the relevant equations for the individual variables.

To begin, a basic overview of the necessary phonon physics is helpful. The relevant derivations for the dispersion relation can be found in solid state physics texts such as those by Kittel [30] or Ashcroft and Mermin [12]. A schematic dispersion relation for a one dimensional solid with two masses per primitive basis is in Figure 2-12, where the vertical axis is the angular frequency ω and the horizontal axis is the wavevector:

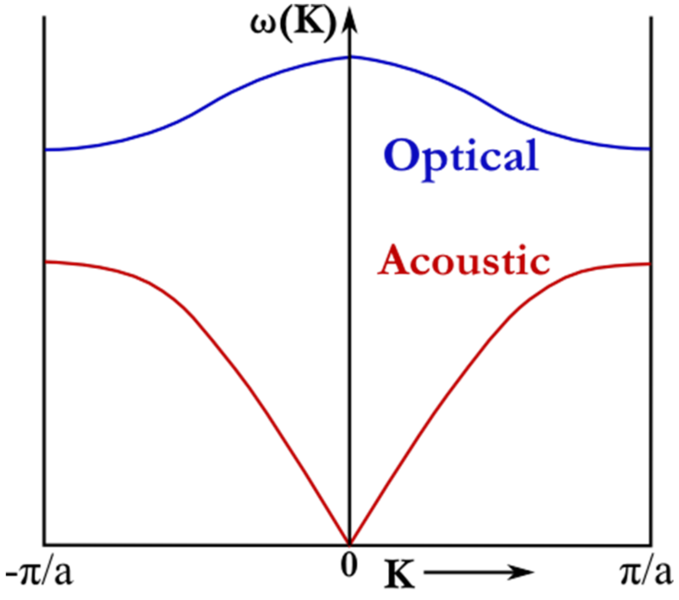

Figure 2-12. Schematic dispersion relation for optical and acoustic phonon branches for a diatomic linear lattice. The lattice parameter is a. The number of branches will increase for 3D materials and for materials with increased number of ions per primitive basis. See Ref [58] for more.

It can be seen that multiple solutions for the dispersion relation are found, each associated with a different type of vibration of the lattice. These different solutions, called ‘branches’ of the dispersion relation, are subdivided into acoustic and optic types as well as transverse and longitudinal types. Acoustic phonons are phonons where all ions vibrate in phase with each other, while optical phonons occur when cations and anions vibrate out of phase with one another. Transverse phonons vibrate transverse to the propagation direction, while longitudinal phonons vibrate along the propagation axis. All materials have 3 acoustic branches – one associated with vibration along the propagation axis and two for the two orthogonal directions – and $3n - 3$ optical branches exist where n is the number of ions per primitive unit cell[58].

The important velocity parameter for thermal conductivity is the group velocity of a phonon, defined as[59]:

$$v_g \equiv \frac{\partial \omega}{\partial K} \tag{2.28}$$

Comparison with Figure 2-12 shows that v_g is the slope of the dispersion relation. From a perspective of engineering thermal conductivity, the phonon dispersion relation is determined via the ionic masses and bond strengths. This means the group velocity is not easily changed within a given composition. Large ions and weak bond strengths tend to lower v_g while small ions with strong bond strengths tend to raise v_g. It is clear from Figure 2-12 that v_g can vary drastically as a function of phonon branch and K. In general, acoustic phonons have a much larger group velocity than optical phonons due to the relatively dispersionless nature of the optical phonons, which results in a low group velocity. This is not to say that optical phonons do not affect the thermal conductivity. The group velocity for optical phonons is finite and therefore they contribute to the thermal conductivity, but to a smaller degree. Optical phonons also may also attenuate the heat flux of acoustic phonons under certain circumstances. For example, materials such as the skutterudies and clathrates often have optical phonon branches with energies similar to acoustic branches. [60, 61] The similarity in energy between the branches causes scattering of the acoustic branches by the optical phonons, thereby decreasing the mean free path of the acoustic phonons and lowering the thermal conductivity. These low-lying optical phonons are the result of filling the large crystallographic sites with ions that have relatively weak bonding to the surrounding lattice.

Although understanding v_g and C is instructive for understanding thermal conductivity, the majority of engineering lattice thermal conductivity comes down to manipulating the mean free path of phonons. In a perfect solid with only harmonic vibrations, no phonons will scatter and the thermal conductivity will be very large. However, in real materials phonons will scatter off any imperfections which cause anharmonicity such as point defects, grain boundaries, phase boundaries, or other phonons. For example, a large number of point defects can be added into a material via forming a solid solution thereby significantly lowering the thermal conductivity as shown below for Si_xGe_{1-x} in Figure 2-13[62]:

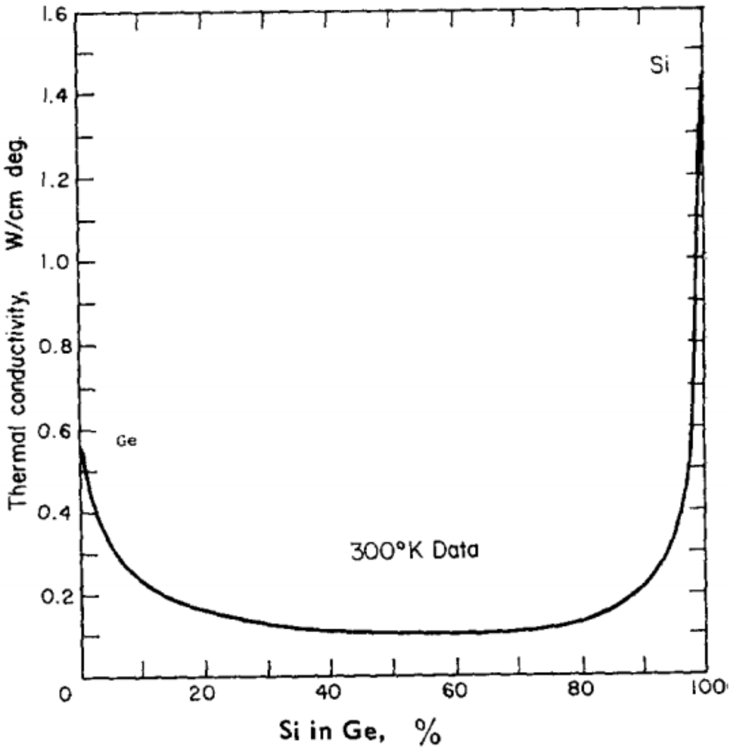

Figure 2-13. Thermal conductivity of Si-Ge solid solutions as a percentage of Si. The thermal conductivity of solid solutions is reduced compared to the pure end members due to impurity scattering. From Ref. [62].

Solid solution creation is a very common technique used to lower the lattice thermal conductivity in thermoelectrics. Other ways to lower the mean free path are by using grain boundaries (e.g. nanograined materials), making amorphous materials, or lowering the mean free path via boundary scattering as is done in nanowires or thin film thermoelectrics. Examples are shown in Figure 2-14 which presents the thermal conductivity of various types of bulk and nanostructured silicon [63].

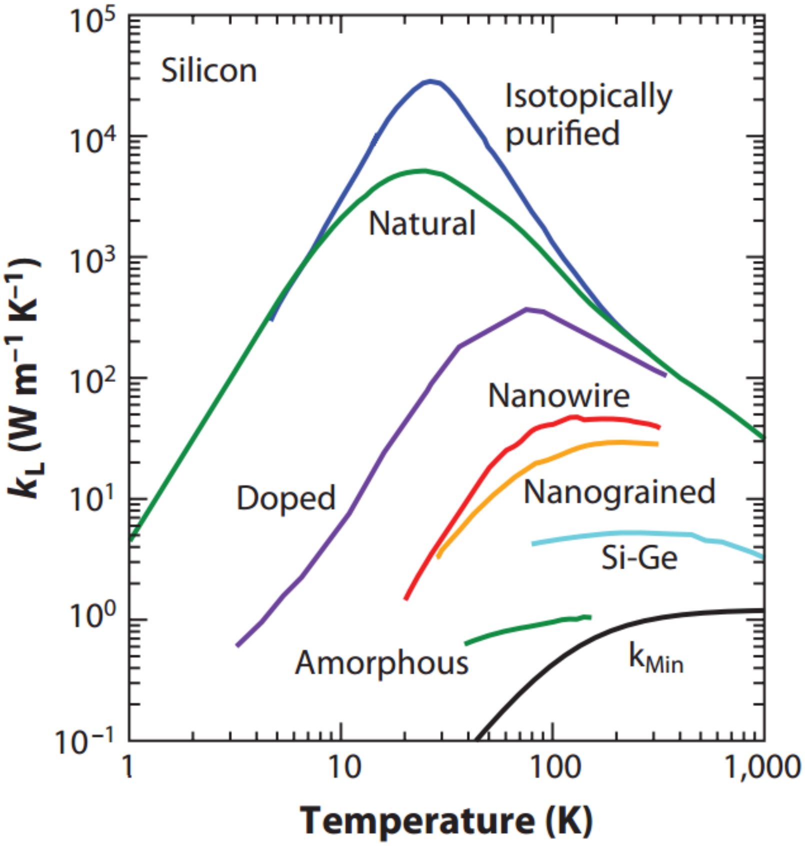

Figure 2-14. Thermal conductivity of various types of bulk and nanostructured silicon. From Ref. [63].

Structural defects tend to dominate thermal conductivity at low temperatures, but as temperatures increase, higher energy phonons become activated and this results in an increase in phonon-phonon scattering. This increasing phonon-phonon scattering acts to decrease the mean free path of phonons as temperature increases, thereby decreasing the thermal conductivity. This results in the '1/T law' which states that the thermal conductivity of materials in the temperature regime where phonon-phonon scattering is dominant will show $k \propto {}^{1}/_{T}$ [64]. Most relatively pure materials will show this dependence. Exceptions include glasses, where the mean free path is limited by the structure and not by phonon-phonon scattering (For example, see the 'Amorphous' and 'Si-Ge' data in Figure 2-14).

The final values for inserting into the dilute gas formula are the heat capacity of the phonon gas, $C_\eta * \eta$. The heat capacity of the lattice is given by the Debye and Einstein relations, as discussed in many basic solid state physics and thermodynamics texts. [30, 65] The Einstein model gives that the heat capacity, C_v, for a system of N oscillators oscillating at frequency ω is given by[66]:

$$C_v = 3Nk_b\left(\frac{\hbar\omega}{k_bT}\right)^2 \frac{\exp(\hbar\omega/k_bT)}{(\exp(\hbar\omega/k_bT)-1)^2} \tag{2.29}$$

At high temperatures this function extends to a limit of $3Nk_b$ - known as the Dulong-Petit value. This holds true for compounds as long as N is the number of oscillators *per formula unit*. A plot of heat capacity for multiple oxides is given in Figure 2-15. Note the heat capacity is in units of J g-atom^{-1}°C$^{-1.}$

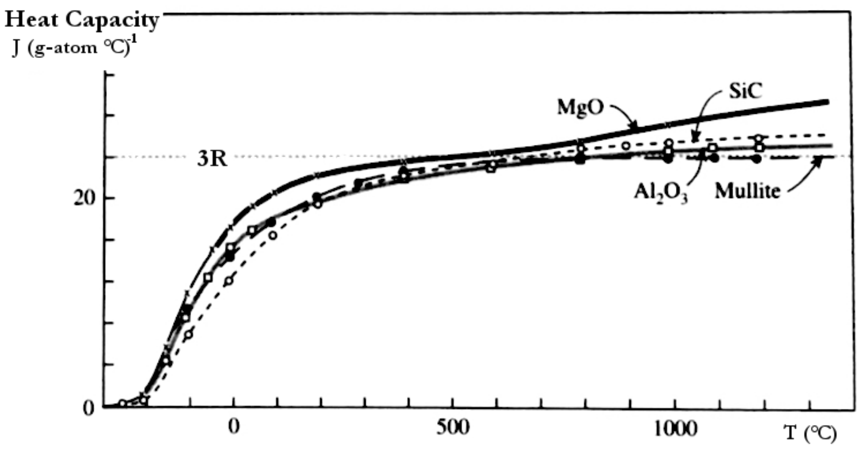

Figure 2-15. Heat Capacity of some ceramics as a function of temperature. From Ref [67].

Most of the heat capacity increase happens before the Debye temperature, θ_D, which is material dependent and depends on the bond strength, elastic constants, and melting point of the material[67]. The heat capacity can also change abruptly at phase transitions, e.g. in $BaTiO_3$[68], although changes to the structure above and below the transition do not tend to matter a great deal as the number of atoms per formula unit remains constant.

2.2.3 Effects of Ferroelectricity on Lattice Thermal Conductivity

Again it is helpful to start with the phonon dispersion relation. This is because displacive phase transitions occur via the softening of phonon branches.[69] This means that a phonon branch decreases in frequency as temperature decreases until the frequency reaches zero, at which time the structure of that phonon is frozen into the lattice. Ferroelectricity specifically is the softening of an optical phonon branch near the Brillouin zone center where the cations and anions are vibrating with an infinite wavelength. This means that when the optical branch reaches zero frequency, the cations and anions associated with the phonon will freeze with displacements relative to each other, resulting in a dipole. This is shown schematically in Figure 2-16.

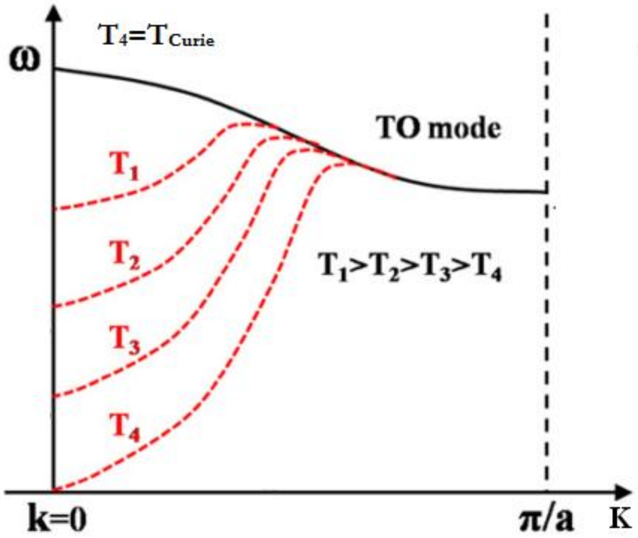

Figure 2-16. Schematic representation of the softening of the transverse optic phonon mode responsible for ferroelectricity in displacive ferroelectrics. Adapted from Ref. [32].

During this process, the optical phonon branch increases in slope, and therefore the group velocity is increased. This introduces an additional branch with a significant group velocity on top of the three acoustic phonon branches. Additionally, the now low-lying optic phonon branch should interact with the acoustic phonon branches, although little research has been done on consequences of this interaction with respect to thermal conductivity. However, acoustic measurements show interactions between the low-lying optic mode and the acoustic modes via changes in the sound velocity near the transition temperature[70].

These two competing processes, the interaction with the acoustic phonon branch and the introduction of an additional branch with a large group velocity act in opposite ways - the former to decrease the thermal conductivity and the latter to increase it. The net result is that changes in the thermal conductivity are found at the transition temperature in multiple ferroelectrics, but the changes are typically ~30% of the thermal conductivity or less in materials investigated so far [71].

The thermal conductivity can also be modified via changes to the mean free path of phonons by the introduction of scattering interfaces. Ferroelectric domain walls can act as scattering interfaces. This was beautifully shown by Weilert et al. using phonon focusing experiments[8]. The phonon focusing experiments were qualitatively consistent with the expected results calculated via acoustic mismatch theory (see Ref. [72]). This shows that scattering depends on the phonon mode, polarization, and direction of propagation as well as the symmetry change at the domain wall. Additionally, Ihlefeld et al. measured the thermal conductivity of a ferroelectric thin film while using an electric field to tune the density of domain walls.[7] It was shown that the thermal conductivity could be modulated via the application of the electric field; the effect was small, with only a change of ~15%. It may be that the larger domain wall mobilities in bulk materials would show a larger effect, but this is yet to be determined. These studies suggest that a large number of domain walls as well as a variety of different orientations of domain walls are necessary to lower the thermal conductivity.

A large number of boundaries around polar clusters occur in relaxor ferroelectric materials, and in fact many relaxor ferroelectrics show low and glasslike thermal conductivities, as seen in Figure 2-17[32].

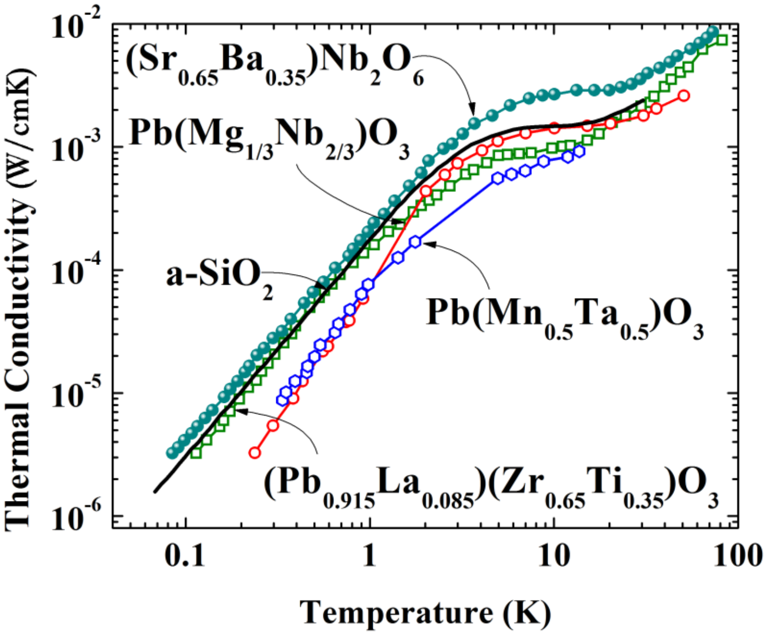

Figure 2-17. Thermal conductivity of multiple relaxor ferroelectrics compared to amorphous SiO_2. Figure taken from Ref. [32]

The detailed mechanism of scattering of phonons off of nanosized polar regions is up for debate, but possibilities include scattering by localized phonon modes [73–75], and scattering due to a boundaries related to the polarization similar to Ref. [7, 8].

One of the key goals of this research is to try to utilize the fact that relaxor ferroelectrics have low thermal conductivities to engineer thermoelectrics. A glasslike thermal conductivity is a good starting point in the design of a thermoelectric, as long as adequate doping can be achieved to reach desirable electrical carrier concentrations and the mobility of the carriers is high enough so that the power factor can be adequately large.

The route of increasing thermoelectric figure of merit by decreasing the thermal conductivity via ferroelectric boundaries does have one major downside - it can only be done in ferroelectrics. Ferroelectrics tend to be insulators with d^0 electron configurations[76]. Additionally, ferroelectricity tends to occur in highly polarizable lattices, and this means that the mobility of any created charge carriers will be relatively low, and the power factor will therefore suffer. Some materials related to ferroelectrics, however, show high mobilities, including Nd:$SrTiO_3$[77], suggesting that high-mobility materials can be made despite the large polarizability of the host lattices.

2.3 Ferroelectricity

The most common definition of a ferroelectric is a material which has a spontaneous electric polarization that is switchable between multiple symmetrically equivalent sites using an external electric field.[78]

Ferroelectrics contain a 'spontaneous polarization', or a polarization which forms without an applied electric field. From a symmetry perspective, 10 out of 32 possible point groups have a polar axis (a spontaneous polarization). All ferroelectric materials fit within these 10 polar point groups, but to classify as a ferroelectric, the spontaneous polarization must be switchable by an external electric field.

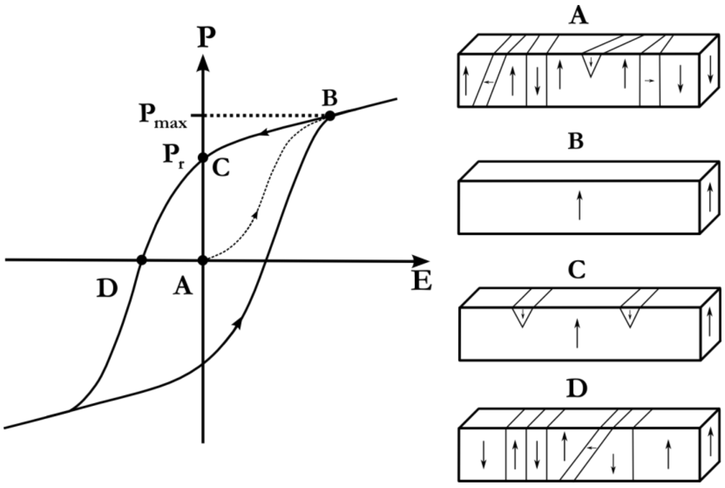

Figure 2-18. A ferroelectric hysteresis loop (left) and the associated domain structures at different locations on the loop (right). From Reference [78].

Inside of a crystal or grain, regions where the polarization of all unit cells is oriented along the same direction, form. These volumes are called domains. The walls between domains are coherent interfaces and therefore stress or charge can build up at domain walls. The strain and charge at domain walls is important to the following work for a few reasons. First, mismatch in the acoustic properties over domain walls can act as a scattering mechanism for phonons[7, 8]. Secondly, charged domain walls tend to be unstable in insulating ferroelectrics due to the required buildup of opposing electric fields[79], but in conducting ferroelectrics, the inability to easily form charged domain walls may be lifted due to screening. For thoroughness it should be noted that charged domain walls can exist in insulating ferroelectrics [80, 81], and interesting properties have been found associated with them – but that is outside of the scope of this thesis.

2.3.1 Relaxor Ferroelectrics

Relaxor ferroelectrics are a subset of ferroelectrics. Relaxor ferroelectrics have nanoscale polar regions as opposed to the more macroscopic domain sizes of normal ferroelectrics[82]. The precise nature of these polar nanoregions (PNR) is debated, and the answer is likely different for different materials, but chemical inhomogeneity, chemical disorder, and phononic breather modes have all been proposed[83, 84]. The important point to this work is that the PNR are much smaller and, therefore, higher in number density, compared to macroscopic domains.

Relaxor ferroelectrics do not exhibit a sharp paraelectric-ferroelectric phase transition. Instead, the net polarization slowly increases on cooling. The permittivity is highly frequency dependent.

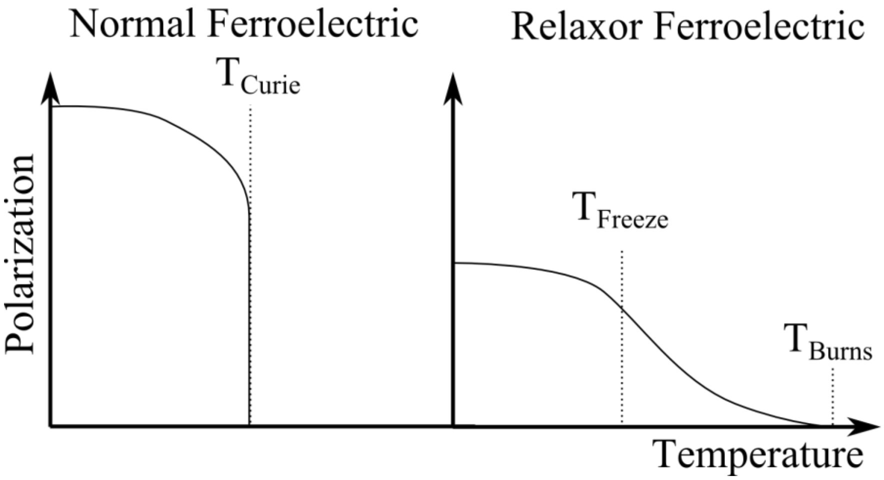

Figure 2-19. Comparison of the temperature dependence of the spontaneous polarization for a normal (left) and relaxor (right) ferroelectric. Note that many normal ferroelectrics such as $BaTiO_3$ may have residual ferroelectricity above the Curie temperature.

Figure 2-19 schematically shows the polarization as a function of temperature for normal and relaxor ferroelectrics. Unlike the abrupt development of a spontaneous polarization directly below the Curie temperature in normal ferroelectrics, the polarization in relaxors forms over a wide temperature range (sometimes multiple hundreds of degrees). The polarization exists well above the temperature of the maximum dielectric constant and is present up until the Burns temperature, T_{Burns}, above which the polarization is zero[82].

2.4 Thermoelectrics

2.4.1 Thermoelectric Effects and Devices

A basic thermoelectric circuit is shown in Figure 2-20. It consists of two conductors, *a* and *b*, which make two junctions, A and B. In practice *a* is a sample under measurement while *b* is the material of the lead wires.

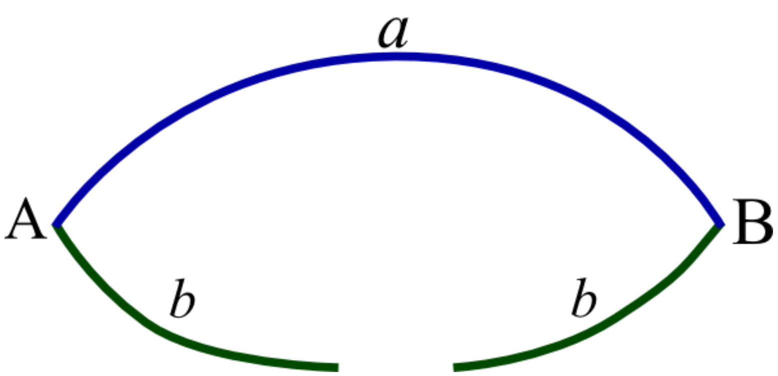

Figure 2-20. A basic thermoelectric circuit

The behavior of this circuit will depend on the thermoelectric characteristics of a and b, namely due to the Seebeck effect, Peltier effect, and Thompson effect[85]. The magnitude of these effects are understood through the Seebeck coefficient (or thermopower), S, the Peltier coefficient, Π, and the Thompson coefficient, τ, respectively. The result of each effect on the circuit in Figure 2-20 will be discussed below. A materials physics description of the different effects will be given in 2.4.2, but the discussion here will focus mainly on the basics of thermoelectricity and definitions. The discussion follows those of Ref. [85–88]

If a temperature difference is created between A and B then a voltage difference, V, will be generated between the two segments of b. This voltage is called the Seebeck voltage and its magnitude is determined by the Seebeck coefficient for the circuit, S_{ab}. The size of the Seebeck voltage given a set temperature gradient is:

$$S_{ab} = S_a - S_b = \frac{V}{\Delta T} \tag{2.30}$$

where S_a and S_b are the absolute Seebeck coefficients for materials a and b, respectively. The sign for S_{ab} is positive if current flows along the temperature gradient. That is, if A is at a higher temperature than B, then current would flow from A to B. In semiconductors, the sign of the majority carrier's charge is the sign of the Seebeck coefficient. To obtain the absolute Seebeck coefficient of the sample, S_a, the contribution from the lead wires must be subtracted out from the complete circuit measurement ($S_a = S_b - S_{ab}$). The Seebeck coefficient is useful in understanding electron transport in materials and an in depth discussion is given in 2.4.2.

If focus is now given to a junction, say junction A, it is clear the current over the junction must be continuous, but the heat carried per electron in materials a and b may be dissimilar. If so, when current flows through the junction, heat must be dissipated or absorbed as a consequence. This is known as the Peltier Effect. In reference to the circuit in Figure 2-20, if a clockwise current, i, is imposed and heat is output at A and absorbed at B, then the junctions have a positive Peltier coefficient. The power exchanged at the junction A is:

$$P = \Pi_{ab} i = (\Pi_a - \Pi_b) i \qquad (2.31)$$

where P is the heat exchanged per unit time, i is the current over the junction (from a to b), Π_a and Π_b are the absolute Peltier coefficients for materials a and b, respectively, and Π_{ab} is the Peltier coefficient of the junction. The absolute Peltier coefficient of a material can be understood as the heat carried per electron in that material.

The final thermoelectric effect, the Thompson effect, occurs when current flows through a single conductor which is subject to a temperature gradient. The power generated is then generated equal to:

$$P = \beta i \Delta T \qquad (2.32)$$

where β is the Thompson coefficient. A heat is generated from the current flow due to the temperature dependence of the Seebeck coefficient. This can be thought of as a continuous version of the Peltier effect. Although the Thompson coefficient is not pertinent to most thermoelectric devices, it should not be ignored in rigorous calculations.

The three thermoelectric effects are quite similar to one another in that they deal with the thermoelectric values of the electronic carriers in materials. Thermodynamics relates the three coefficients via the Thompson relations. The first and second Thompson relations are, in order:

$$\beta_a - \beta_b = T\frac{dS_{ab}}{dT} \tag{2.33}$$

and

$$\Pi_{ab} = S_{ab}T \tag{2.34}$$

The second Thompson relation shows the link between thermoelectric cooling (Π_{ab}) and thermoelectric power generation (S_{ab}).

Important to this work is the Figure of Merit for thermoelectric power generation. A derivation of this figure of merit based on the device efficiency of thermoelectric power generators follows, after Ref. [89, 90]. The device efficiency, φ, of a thermoelectric generator is given by the energy supplied to the electrical load over the heat energy absorbed at the hot junction:

$$\varphi = \frac{Energy\ supplied\ to\ the\ load}{Heat\ energy\ absorbed\ at\ the\ hot\ junction} \tag{2.35}$$

If the Seebeck coefficient, Peltier coefficient, and the thermal conductivity, κ, are temperature independent (since $\frac{dS_{ab}}{dT}=0$ the Thompson coefficient will be zero), and the contact resistances at the junctions are negligible compared to the resistances of the thermoelectric legs, then to determine the heat absorbed at the hot junction three effects must be considered. First, the Peltier heat absorbed at the hot junction, secondly, part of the Joule heat generated in the elements will be created at the hot junction, and finally heat will be conducted away from the hot junction via thermal conduction. Equation (2.35) can be then expressed as:

$$\varphi = \frac{i^2 R_{Load}}{S_{ab} i T_H + K(T_H - T_c) - \frac{1}{2} i^2 R} \tag{2.36}$$

where R_{Load} is the resistance of the load, R is the resistance of the thermocouple legs, K is the thermal conductance of the legs, and the Peltier coefficient has been expressed as $S_{ab}T_H$. Equation (2.36) can be maximized with respect to R and K by changing the dimensions of the thermoelectric elements, and the maximum efficiency becomes:

$$\varphi_{max} = \frac{T_H - T_c}{T_H} \frac{\sqrt{1 + z_c\overline{\overline{T}}} - 1}{\sqrt{1 + z_c\overline{\overline{T}}} + \frac{T_C}{T_H}} \tag{2.37}$$

where $\overline{T}$ is the mean average between T_C and T_H and z_c is the figure of merit of the couple given by:

$$z_c = \frac{{S_{ab}}^2}{\left[\left(\frac{\kappa_a}{\sigma_a}\right)^{\frac{1}{2}} + \left(\frac{\kappa_b}{\sigma_b}\right)^{\frac{1}{2}}\right]^2} \tag{2.38}$$

If the thermoelectric properties of the n-type and p-type materials are similar in magnitude, then the couple figure of merit becomes roughly the average of the two material's figures of merit. In this case, it becomes practical to optimize their properties using the figure of merit for a single material:

$$zT = \frac{S^2\sigma}{\kappa} T \tag{2.39}$$

where $S^2\sigma$ is referred to as the power factor. The figure of merit, *z*, has units of inverse Kelvin so Equation (2.39) uses the more common dimensionless figure of merit, zT.

In order to maximize thermoelectric performance, the figure of merit should be maximized. From the aspect of the three parameters in Equation (2.39) this can be formulated as a function of carrier concentration. With increasing carrier concentration, the electrical and thermal conductivity increase and the Seebeck coefficient tends to decrease, resulting in a set of conflicting optimization parameters and a maximum *zT* as a function of *n*, as shown in Figure 2-21[91].

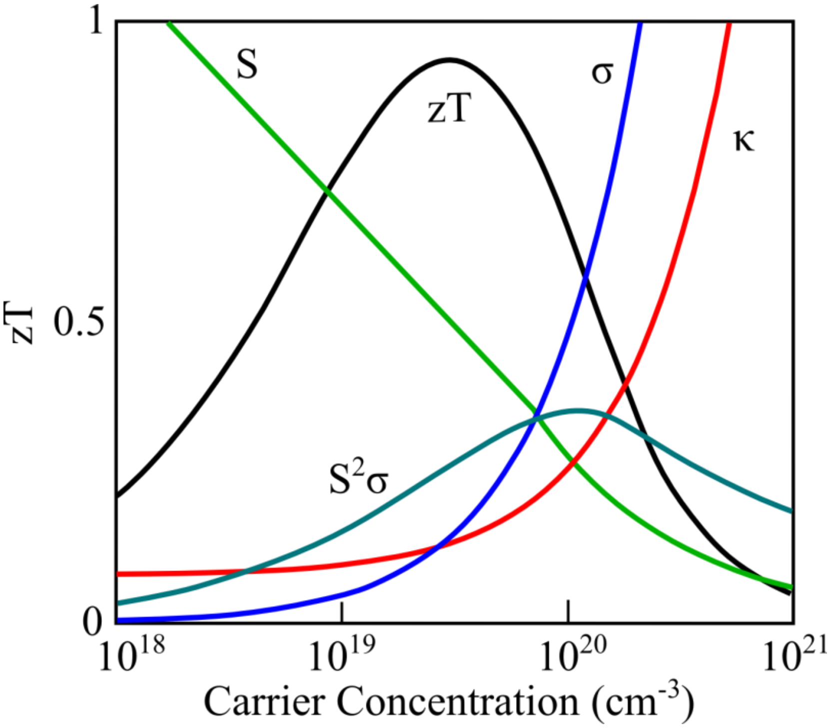

Figure 2-21. Changes in electrical conductivity, thermal conductivity, Seebeck coefficient, power factor, and figure of merit as a function of carrier concentration. The Seebeck coefficient decreases with increasing carrier concentration while the thermal and electrical conductivity increase. This creates a maximum power factor and figure of merit as a function of carrier concentration. Redrawn from Ref. [91]

The best thermoelectrics tend to have carrier concentrations ~10^{19}-10^{21} cm^{-3}.[91] Due to low electron mobilities, oxide thermoelectrics often have a maximum z at higher electron concentrations. The thermal conductivity can be split into the electronic and lattice portions of thermal conductivity, κ_e and κ_l as shown in Figure 2-22.

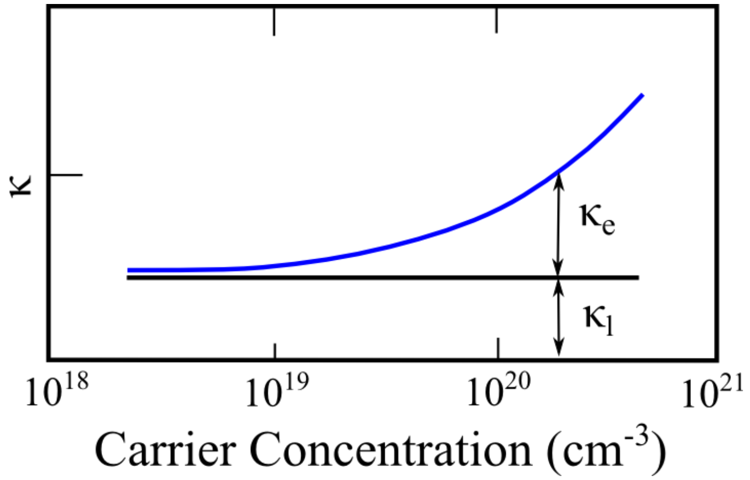

Figure 2-22. Electrical and lattice thermal conductivity as a function of carrier concentration.

The lattice portion of the thermal conductivity is normally assumed to be dopant concentration independent, but dopants which are used to change the carrier concentration can act as scattering sites, so this isn't necessarily always the case.[63] Using the Wiedemann-Franz law (Equation (2.25)), the figure of merit can be written as:

$$zT = \frac{S^2}{L\left(1 + \frac{\kappa_l}{\kappa_e}\right)} \tag{2.40}$$

where L is the Lorenz number. Equation (2.40) clearly shows that minimizing the lattice thermal conductivity is important for optimizing zT.

2.4.2 Material Physics of Thermopower

When a temperature gradient is applied to a material, the electron distribution as a function of energy spreads out. The total electron density remains essentially uniform, but the hot end of the material has a higher density of high-energy electrons and the cold end has a higher density of low-energy electrons. The high-energy electrons therefore diffuse toward the cold end and the low-energy electrons diffuse toward the hot end. A net current results from the energy-dependent diffusion rate of the electrons.[85] This current causes an opposing voltage, and the total current eventually becomes zero. This opposing voltage is the Seebeck voltage. The magnitude of the Seebeck voltage will depend on the magnitude of the temperature gradient and the details of the electronic structure which determine the energy-dependent diffusion rate for electrons. Empirically, the Seebeck voltage can be determined via the application of a temperature gradient to a sample and the simultaneous measurement of the resulting voltage. The relation between the applied temperature gradient and the Seebeck voltage is given by

$$V_{Seebeck} = S(T)\Delta T \tag{2.41}$$

where $V_{Seebeck}$ is the Seebeck voltage, S is the Seebeck coefficient (or thermopower), and ΔT is the applied temperature gradient detected between the probes used to measure the voltage. As the Seebeck coefficient is temperature dependent, the above holds only for small ΔT. The aforementioned details of the energy-dependent diffusion rate for electrons is buried within the Seebeck coefficient and the derivation of the Seebeck coefficient depends heavily on the details of the band structure and electron transport in materials.

The Seebeck coefficient is a useful tool for determining the dominant electron transport mechanism in a material, and understanding the Seebeck coefficient is key to engineering new thermoelectric materials. For both of these reasons, the goal of this section will be to give the reader an intuitive sense for the relation between the band structure and the Seebeck coefficient magnitude and temperature dependence.

Ioffe in 1957 gave a simple instructional explanation to calculate the Seebeck coefficient based on thermodynamics[92, 93], which will be laid out here. First, consider a junction between two conductors, a and b, at a constant temperature T where the two materials at the junction have been allowed to relax to equilibrium. As the two conductors are in equilibrium, their chemical potentials are in equilibrium such that their Fermi energies are equal and the internal energy of each of the conductors can be written as:

$$U_{(a,b)} = Ts_{(a,b)} + E_f \tag{2.42}$$

where

$$E_f = E_{f_a} = E_{f_b} \tag{2.43}$$

The average energy U and entropy s of the two conductors are different, but their Fermi energies are the same, so:

$$U_a - Ts_a = U_b - Ts_b \tag{2.44}$$

When an electron passes through the junction, the average energy of the electron changes by $U_a - U_b$, and this creates the Peltier heat Π_{a-b} where:

$$U_a - U_b = \Pi_{a-b} \tag{2.45}$$

From Equations (2.44) and (2.45) the Seebeck coefficient can be obtained using the second Thompson relation, Equation (2.34):

$$S = \frac{\Pi_{a-b}}{T} = \frac{U_a - U_b}{T} = S_a - S_b \tag{2.46}$$

Comparison of (2.46) and (2.44) shows that the Seebeck coefficient is a measure of the entropy change of an electron over the junction. That is the Peltier and Seebeck coefficients are measures of the energy and entropy moved along with the charge carriers, respectively.

Equation (2.46) is useful for understanding the meaning of the Seebeck coefficient, but it is not useful in designing thermoelectrics, as the value is not related to manipulatable materials properties. An equation for the Seebeck coefficient in the non-interacting electron picture is as follows, as shown in [94]. The heat transport of a current di from an electron at energy E is given by:

$$\frac{-(E - E_f)}{e} di \tag{2.47}$$

The current di due to electrons between E and dE is given by:

$$di = -\sigma(E)\frac{df}{dE}FdE \tag{2.48}$$

where $\sigma(E)$ is the energy-dependent conductivity at E, f is the Fermi function, F is the applied electric field, and E is energy. Plugging (2.48) into (2.47) the total electronic heat transport can be related to the Peltier coefficient as follows:

$$\mathit{\Pi} i = \frac{F}{e}\int \sigma(E)\left(E - E_f\right)\frac{df}{dE}dE \tag{2.49}$$

Using the Second Thompson Relation and rearranging some variables, the Seebeck coefficient follows:

$$S\sigma = -\frac{k_b}{e}\int \sigma_E\left(\frac{E - E_f}{k_b T}\right)\frac{df}{dE}dE \tag{2.50}$$

where σ_E is the electrical conductivity at energy E, e is the charge of an electron, E is the energy of the electron, E_f is the Fermi energy, and f is the Fermi Dirac function. A more rigorous derivation using a Green's Function formalism [95] finds this equation to be exact. From Equation (2.50) it can be seen that the Seebeck coefficient is determined mainly by the band structure of the material (buried within σ_E) and the energy of the electrons in comparison to the Fermi energy. Increasing the Seebeck coefficient therefore becomes an exercise in modifying the band structure such that conduction of electrons occurs at high energies compared to the Fermi energy. It should be reiterated that the above equation is for the free electron model and does not hold for strongly correlated electrons.[95] As a rule of thumb, since the Wiedemann-Franz law can also be exactly derived using the non-interacting electron picture, in materials for which the Wiedemann-Franz law fails, Equation (2.50) also fails.

From an engineering perspective, it is instructive to look at specific cases of (2.50) where the formula can find practical use in identifying conduction mechanisms and engineering thermoelectrics. For a metallic system, where the Fermi energy lies within a series of delocalized electronic states, electrical conduction occurs by electrons within the vicinity of the Fermi energy[52]. For metals, Equation (2.50) simplifies to:

$$S = \frac{\pi^2}{3}\frac{k_b^2 T}{e}\frac{dln\sigma(E)}{dE}\bigg|_{E_f} \tag{2.51}$$

where $\sigma(E)$ is the electronic conductivity as a function of band filling. If the electronic scattering is independent of energy, then $\sigma(E)$ is proportional to the density of states at E. This means that the Seebeck coefficient of a metal is linearly dependent on temperature with a slope that is determined via the derivative of the density of states with respect to energy at the Fermi energy, $\frac{dln\sigma(E)}{dE}\Big|_{E_f}$. Recall that the Seebeck coefficient comes from the energy-dependent diffusion rate of electrons and Equation (2.51) shows this nicely. Optimization of the Mott formula depends on the details of the band structure; a good review is available from Ref. [96].

For semiconducting systems, the Seebeck coefficient can be derived via the Boltzmann transport equation, and is given by[97]:

$$S = -\frac{k_b}{e}\left(\frac{5}{2} - r - ln\left(\frac{n}{N_c}\right)\right) \tag{2.52}$$

where r is a constant that depends on scattering, and N_c is the density of states of the conduction band. For a non-degenerate semiconductor, Maxwell statistics can be used and therefore[98]:

$$n = N_c exp\left(\frac{E_f - E_c}{k_b T}\right) \tag{2.53}$$

Plugging in Equation (2.53), Equation (2.52) becomes

$$S = \frac{k_b}{e}\left(\frac{5}{2} - \frac{E_f - E_c}{k_b T}\right) \tag{2.54}$$

It is seen from Equation (2.54) that for a nondegenerate semiconductor, the Seebeck coefficient will have an inverse relationship with temperature. This will continue until minority carriers become a significantly large portion of the electrical conductivity, in which case ambipolar conduction will cause the Seebeck coefficient to decrease.[99]

It should be noted that Equation (2.54) is derived for the intrinsic regime. Many materials will go through a saturation where further ionization of impurities is no longer occurring and therefore the carrier concentration remains constant. If the carrier concentration is instead temperature independent, Equation (2.54) will no longer hold. Instead, n will be set as constant and a value of N_c will be calculated for a parabolic band as[98, 100]:

$$N_c = 2\left(\frac{m_e k_b T}{2\pi\,\hbar^2}\right)^{3/2} \tag{2.55}$$

where $\hbar$ is the reduced Planck's constant and m_e is the electron effective mass. Inserting (2.55) into (2.52) results in[101]:

$$S = \frac{k_b}{e}\frac{3}{2}\ln(T) + const. \tag{2.56}$$

The important aspect of this equation is the logarithmic dependence of Seebeck coefficient on temperature. The prefactor of $\frac{k_b}{e}\frac{3}{2}$ will be different if the conduction band is not parabolic, as is often the case in narrow band materials or other complex band structures such as for materials with impurity bands. The prefactor will also deviate from the normal value if the effective mass is not constant with temperature[101]. Nevertheless, a logarithmic dependence of the Seebeck coefficient is often indicative of a constant carrier concentration with a temperature dependent N_c and is found in, for example, even the earliest measurements on Bi_2Te_3[102] and will be important in discussion of electron transport in Chapter 4 (4.3.2).

If the thermal energy of the system, k_bT, is greater than the bandwidth, W, then all of the states in the band will be available for electrons to occupy. As discussed previously, the Seebeck coefficient can be thought of as the entropy transported per electron. In the case where $k_bT \gg W$, Boltzmann's entropy formula can be utilized. This gives the following relation[103]:

$$S = \frac{k_b ln(\Omega)}{e} = \frac{k_b}{e}\ln(\frac{c}{1-c}) \tag{2.57}$$

where Ω is the number of microstates possible and c is the ratio of the number of electrons to the number of sites in the band. Equation (2.57) is called the Heike formula and is commonly applicable to narrow band materials[104–106]. As these narrow bands facilitate polaronic formation as discussed in 2.1.4, the Heike formula is often applicable for materials where polaronic conduction occurs. An easy way to understand the Heike formula is to think of the thermopower as the entropy of mixing between electrons and empty states within the band. Given this, the Heike formula resembles the thermodynamic entropies of mixing of solid solutions, as the basic derivation for both is the same. This analogy breaks down when degeneracies are taken into account, as shown by Doumerc [107] and later expanded by Koshibae et al.[108]. These groups showed that the Heike formula must be modified for spin and orbital degeneracies of the two valence states participating in hopping, resulting in:

$$S = \frac{k_b}{e}\ln(\frac{g_1}{g_2}\frac{c}{1-c}) \tag{2.58}$$

where $g_1$and g_2 are the sum of the spin and orbital degeneracies associated with the two cations responsible for hopping conduction. This becomes important for many oxides, especially cobaltites where g_1 is 6 and g_2 is 1, resulting in an additional contribution to S of 154μV/K independent of c. This is the source for the abnormally large thermoelectric figure of merit in cobaltites[108]. Care must be taken in understanding what values of g_1 and g_2 are appropriate when calculating c from S, as is sometimes done to determine the carrier concentration from Seebeck coefficient measurements.

The electron transport mechanism can often be revealed by the temperature dependence of the thermopower. Table 2-1 gives the electron transport mechanism and the associated temperature dependence.

Table 2-1 Different electron transport mechanisms and the associated Seebeck coefficient temperature dependences.

Electron Transport Mechanism	Temperature Dependence of S
Metallic Conduction	$S \propto T$
Hopping Conduction (or k_bT>>W)	Temperature Independent S
Activation of electrons over a gap	$S \propto \frac{1}{T}$
Constant n with changing N_c	$S \propto \ln(T)$

2.4.3 Oxide Thermoelectrics

In this section a few key oxide thermoelectrics will be discussed for later comparison with strontium barium niobate. Due to the toxicity, low melting point, and/or low oxidation resistance of many conventional thermoelectrics such as Be_2Te_3, PbTe, Clathrates (Group IV compounds), and skutterudites (Group V compounds) the goal of a thermoelectric which can operate at high temperatures under oxidizing atmospheres is best routed through oxide-based thermoelectrics. Despite this need, oxide thermoelectrics received little attention due to their high phononic thermal conductivity and low electron mobility until the discovery of large figures of merit in Na_xCoO_2.[109] The zT of Na_xCoO_2 single crystals and polycrystalline ceramics are shown in Figure 2-23 alongside other oxide thermoelectrics, and show much higher values than their n-type counterparts.

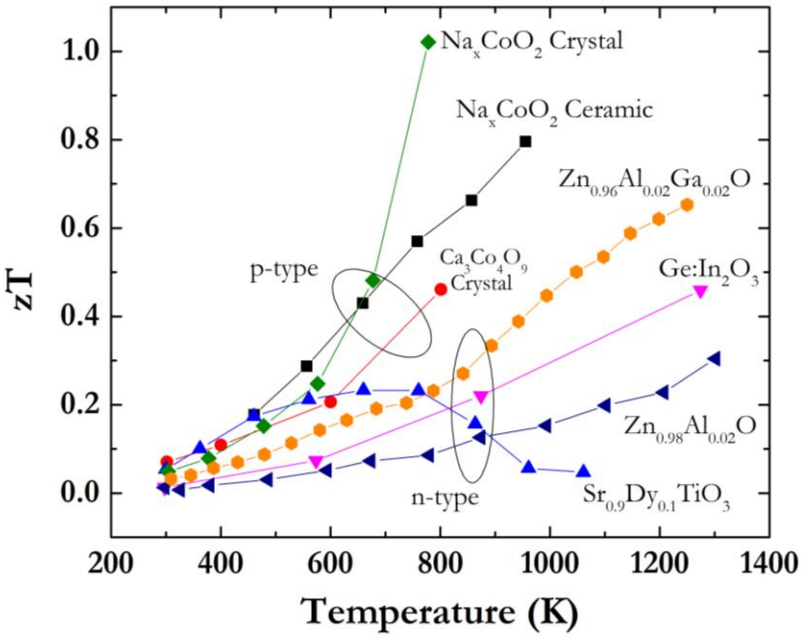

Figure 2-23. Thermoelectric Figure of Merit for some state of the art oxide thermoelectrics. Higher zT values are found for p-type materials than n-type materials, showing the need for new n-type oxide thermoelectrics with higher zT values. Values from [6, 109–114]

This large figure of merit is due to the spin and orbital degeneracy terms in the modified Heike formula (see 2.4.2) of g_1/g_2 of 6 which increase the value of the Seebeck coefficient by 154μV/K.[108] This increased Seebeck coefficient allows for a larger carrier concentration to offset the low electron mobility, resulting in high power factors. Na_xCoO_2 additionally crystallizes in a layered crystal structure which scatters phonons, although this scattering is anisotropic and therefore single crystals show a thermal conductivity of ~20 W/mK at 300K which reduces to ~ 5 W/mK at 800K. This value is reduced in polycrystalline samples to ~2 W/mK between 300K and 800K. [109, 111] High values of zT have also been found in other layered cobaltite systems [113, 115]. As a similar strategy of increasing the Seebeck coefficient cannot be realized in n-type materials, the figures of merit of n-type oxide thermoelectrics are lower than the respective p-type materials.

A search for a compatible n-type leg to make oxide thermoelectric devices has resulted in some possible candidates.

Research on $SrTiO_3$ has identified a large power factor due to the high band degeneracy, and high electron effective mass of $SrTiO_3$, despite the low electron mobility (although $SrTiO_3$ shows high electron motilities if high quality materials are measured, such as those grown by molecular beam epitaxy [116]). Unfortunately, $SrTiO_3$ has a high thermal conductivity at room temperature of ~8 W/mK[117], limiting the zT value. Reduction of the thermal conductivity has been attempted via solid solution formation, although reduction in the power factor accompanies reduction in the thermal conductivity.[77] The best zT found via solid solution formation is $Sr_{0.9}Dy_{0.1}TiO_3$ with a maximum zT of 0.22, shown in Figure 2-23 [110].

ZnO has shown promising thermoelectric properties at high temperatures. The low electronegativity of Zn results in a partially covalent material with a low effective electron mass and relatively high electron mobilities (~100cm^2/Vs)[118]. Doping of ZnO with Al to increase the electrical conductivity results in a measured power factor of 15 µW/cmK^2 [112], however the room temperature thermal conductivity is very large at ~40 W/mK. The thermal conductivity decreases following the 1/T law until a zT of ~0.3 is reached at 1273K. Attempts to decrease the low temperature thermal conductivity were made by changing the Al dopant for cations with a larger mass difference to Zn, such as Ga and In [5]. Unfortunately, decreases in thermal conductivities are accompanied by decreases in the power factor, resulting in lower zT values. Other dopants such as MgO and NiO have been attempted due to their closer electronegativity to ZnO, but again decreases in thermal conductivity were accompanied by decrease in power factor resulting in decreasing zT.[119] However, recent studies of $Zn_{0.96}Al_{0.02}Ga_{0.02}O$ have resulted in increased zT values up to 0.65 at 1273K, and this increase is prescribed to the Ga addition allowing for increased solubility of Al.[114] Unidentified secondary phases are found in $Zn_{0.96}Al_{0.02}Ga_{0.02}O$, suggesting that either the solubility of Al or Ga is reached. Perhaps further work to increase the solubility of Al could result in even larger zT values.

High zT values have also been obtained via the conversion of transparent conducting oxides into the thermoelectrics space. In_2O_3 doped Ge has shown large power factors, up to ~8 μW/cmK^2. Ge doping of In_2O_3 causes a reduction of the thermal conductivity from 10 to 3.5 W/mK, partially due to the formation of $In_2Ge_2O_7$ inclusions which appear above the solid solubility limit for Ge.[6] zT values as high as 0.46 have been obtained in $In_{2.8}Ge_{0.2}O_3$ at 1273K in which these $In_2Ge_2O_7$ inclusions are present.

Despite the strides of n-type thermoelectric oxides resulting in large zT values at high temperatures, no compatible material for Na_xCoO_2 has been found. As discussed in 2.2.3, relaxor ferroelectricity may be an interesting route for lowering the thermal conductivity of oxide materials. The use of oxides with rattler-like ions similar to clathrates or skutterudies may also be of interest. By either method, finding a material with relaxor ferroelectricity/rattler ions with large power factors is of interest to better engineer n-type oxide thermoelectrics to match their larger zT p-type brethren.

2.5 Strontium Barium Niobate

Strontium Barium Niobate (SBN) has the tetragonal tungsten bronze crystal structure as first determined by P.B. Jamieson et al [120]. At room temperature SBN has a space group of P4bm with the structure depicted in Figure 2-24.

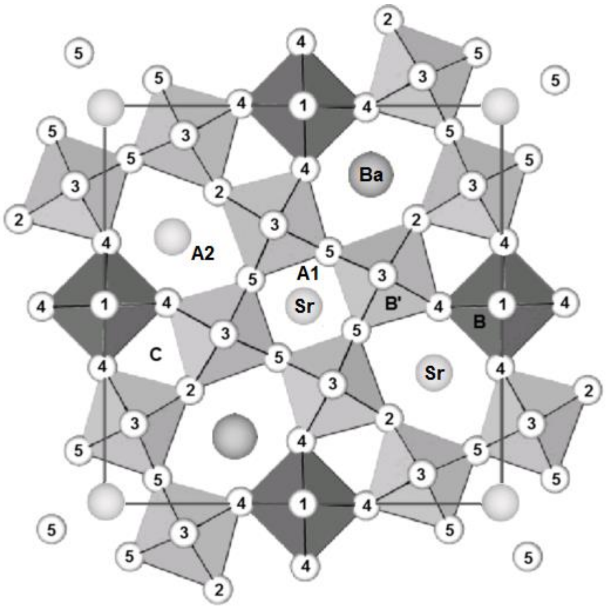

Figure 2-24. Crystal structure of strontium barium niobate shown along [001].

The chemical formula of SBN is $(Sr_x,Ba_{1-x})Nb_2O_6$ and can be written as $(A_1)_2(A_2)_4(C)_4(B)_2(B')_8O_{30}$ where Sr sits on the A1 site, Sr and Ba sit on the A_2 site, the C sites are empty, and Nb sits on the B and B’ sites, and 5 different oxygen sites exist. The structure consists of *c*-axis chains of corner-shared NbO_6 octahedra which are connected in the *a*-*b* plane to form different shapes of channels aligned parallel to the chains along the *c*-axis. The sites within these channels are denoted the A1, A2, and C sites and have coordination numbers of 15, 12, and 3, respectively. In SBN, the A2 site contains Sr and Ba ions in a disordered mixture, but the A1 site has been shown only to be occupied by Sr[120, 121]. SBN is a uniaxial ferroelectric where the spontaneous polarization is due to the displacement of Nb along the *c*-axis. The nature of the ferroelectric properties depends heavily on composition and is related to the amount of disorder found on the A2 site. In $(Sr_{0.33},Ba_{0.66})Nb_2O_6$ the A2 site contains only Ba, while at higher Sr concentrations the A2 site starts to incorporate the extra Sr. As a result, a transition occurs from normal to relaxor ferroelectric properties where x=0.4 is a normal ferroelectric and x=0.7 is a relaxor ferroelectric.[122] The Burns temperature for relaxor ferroelectric SBN (x=0.61) is 350°C and the freezing temperature is 39°C[123]. A change in the octahedral tilt angle along the *c*-axis NbO_6 chains occurs as a function of Sr and Ba concentrations, from 4.5° in x=0.25 to 7.5° in x=0.75[124].

Chapter 3

Metallic-like to Nonmetallic Transitions in a Variety of Heavily Oxygen Deficient Ferroelectrics

In this chapter the coupling between ferroelectric distortions and electrical conductivity is discussed for a small variety of ferroelectric compounds. The coupling between the electron transport and ferroelectricity is important to understand if ferroelectric-thermoelectrics are to be utilized. This knowledge is also useful for the study of ferroelectric/noncentrosymmetric metals. Here, multiple d^0 ferroelectrics with a variety of crystal structures were doped via oxygen deficiency. Metallic-like conduction was identified at high temperatures within these compounds, and non-metallic/semiconducting behavior was found at low temperatures. The idea of the metallic-like to nonmetallic transition being linked to the paraelectric-ferroelectric transition is explored. It is shown that in $(Ba_{1-x}Sr_x)TiO_{3-\delta}$ the metallic-like to nonmetallic transition temperature can be shifted using mechanisms that shift the paraelectric-ferroelectric transition temperature. The magnitude of the shift as a function of Sr doping is shown to be equal to the expected shift in the paraelectric-ferroelectric transition temperature. Other evidence for this coupling will be discussed. One probable mechanism for this ferroelectric-electron transport coupling is determined to be Anderson localization (see section 2.1.3). The relaxor ferroelecric polarization, being of short-range order, may cause disorder and thereby localize the itinerate electrons. As a note, specific aspects of the electron transport of $(Sr_{0.6},Ba_{0.4})Nb_2O_{6-\delta}$ are summarized here, but detailed discussion is reserved for chapters 4-6.

3.1 Background

The study of semiconducting ferroelectrics has shown that coupling between the ferroelectric polarization and electronic carriers exists, and a review of early literature is available in Ref. [125]. Phase transitions in ferroelectrics are affected by high concentrations of electronic carriers. [126] It is well known that increasing the carrier concentration leads to a lowering of the Curie temperature (T_c), a decreasing spontaneous polarization, and a decreasing latent heat of the transition.

Conversely, ferroelectricity is known to perturb electron transport both across grain boundaries and within the bulk of a grain or crystal.[127] For example, to minimize the depolarization energy, any spatial gradients of the spontaneous polarization are compensated by changes in the distribution of charge carriers (i. e. Gauss's Law). This effect can be strong, and can, for example, compensate the large change in the spontaneous polarization at a head-to-head and tail-to-tail domain configuration. Carrier concentrations at these boundaries are high enough to support metallic conductivity.[81, 128] Additionally, as ferroelectricity changes the bonding between the oxygen p-orbitals and the transition metal d-orbitals, changes in the electron density of states may occur. [76]

Although these effects are well-studied in semiconducting ferroelectrics, comparatively little work has been reported on ferroelectric compounds which have carrier concentrations near or above the crossover into metallic conduction, as determined by the Mott Criterion (see section 2.1.3).[32] One reason for this is that many scientists consider a metallic ferroelectric to be a contradiction. The delocalized electronic carriers are thought to screen long range dipole-dipole interactions, and thereby limit the cooperative alignment of dipoles that is the basis of ferroelectricity itself. In addition, high electrical conductivity limits any use of ferroelectrics in switching, transducer, or capacitive applications. However, highly conductive ferroelectric-base compositions are of potential interest for their optical responses[129, 130], magnetoelectricity [130], and ferroelectric-based thermoelectrics. [9, 32] The latter of these is pertinent due to the low thermal conductivity of ferroelectrics that have nanoscale and frustrated polarization, as is the case with relaxor ferroelectrics[71].

A brief summary of ferroelectric metals research will be presented here. Ferroelectric metals were first theorized by Anderson and Blount [131] in the 1960's. Ferroelectric metals have been elusive, as the electronic carriers destabilize the ferroelectric phase by lowering T_c, the spontaneous polarization, and the latent heat of transformation. Nevertheless, Bennet et al. predicted metallic conduction in some ferroelectric compounds [132] and density functional theory calculations on a series of ABX family compounds have found potential metallic ferroelectrics [132]. Experimentally, structural phase transitions comparable to paraelectric-ferroelectric transitions have recently been found in two metallic oxides: $Cd_2Re_2O_7$[133], and $LiOsO_3$[134]. Density functional theory calculations on $LiOsO_3$ by Giovannetti and Capone show the ferroelectric distortion in the unit cell is primarily due to Li-O atomic displacement while the Os-O displacement is relatively small.[135] Hybridization of the Os e_{2g} orbitals and O p orbitals does occur in $LiOsO_3$ as in other ferroelectrics, but the half-filled t_{2g} states responsible for metallic conduction are relatively unperturbed. Puggioni and Rondinelli suggest that ferroelectric/noncentrosymmetric metals rely on this weak coupling between the ferroelectric soft mode and electrons at the Fermi energy.[136]

Separation of metallic conduction and the atomic displacements responsible for ferroelectricity onto two different cation sublattices is a promising route toward making these two phenomena compatible in a single material. Unfortunately, this strategy is possible in only a small subset of ferroelectrics. The lack of an adequate design space for the crystal chemistry raises the difficulty of engineering the large polar cluster density necessary for the low thermal conductivity of ferroelectric-based thermoelectrics. If the interactions between the ferroelectric polarization and the electron transport can be understood within a broader subset of ferroelectric materials, then the design space may be widened to allow for simultaneous engineering of the electron and thermal transport. In this chapter, coupling between the ferroelectric distortion and electrical conductivity is examined in a variety of d^0 ferroelectrics with various crystal structures and paraelectric-ferroelectric transition temperatures.

3.2 Experimental Procedure

A number of octahedrally coordinated ferroelectric compositions with different crystal structures and paraelectric-ferroelectric transition temperatures were doped with donors to induce high electronic carrier concentrations: $(Ba_{1-x}Sr_x)TiO_3$ x=0, 0.1, 0.2, 0.3, and 1 (BSTx), $(Sr_{0.61}Ba_{0.39})Nb_2O_6$ (SBN) and $Sr_2(W_{0.2}Nb_{0.8})_2O_7$. $(Ba_{1-x}Sr_x)TiO_3$ has a perovskite structure, $(Sr_{0.61}Ba_{0.39})Nb_2O_6$ has a tungsten bronze structure[137], and $Sr_2(W_{0.2}Nb_{0.8})_2O_7$ has a perovskite-like layered structure.[138] The paraelectric-ferroelectric transitions for these materials range from <0K for the incipient ferroelectric $SrTiO_3$ to 1600 K for $Sr_2Nb_2O_7$[138, 139].

Samples were fabricated via conventional solid-state reaction and sintering. Precursor powders for the samples include $SrCO_3$, $BaCO_3$, Nb_2O_5, WO_3, and TiO_2; all powders had >99.8% purity. Precursor powders were weighed in the required stoichiometric ratios and mixed via ball milling in ethanol with ZrO_2 media for 12 hours. The dried powders of BSTx and $Sr_2(W_{0.2}Nb_{0.8})_2O_7$ were calcined at 1000 °C for 6 hours, while SBN was calcined at 1200 °C for 6 hours. The high calcination temperature for SBN is needed to homogenize the cation distribution and prevent Nb-rich or Ba-poor regions which cause abnormal grain growth, as discussed by Lee and Freer [140]. The calcined powders were ball milled for 24 hours using ZrO_2 media in ethanol and then sieved using a No. 80 mesh size. The milled powders were uniaxially pressed at 15 MPa and subsequently isostatically pressed at 210 MPa. BSTx was sintered at 1350°C, and $Sr_2(W_{0.2}Nb_{0.8})_2O_7$ was sintered at 1500°C for four hours. Further precautions against abnormal grain growth were taken for SBN by using a two-step sintering process. SBN pellets were first held at 1250 °C for 6 hours to homogenize and then ramped to 1325 °C for 6 hours to sinter. All samples were phase pure by X-ray diffraction and showed relative densities >95%.

Samples were annealed under low partial pressures of oxygen, controlled via gas mixtures of H_2 and H_2O (see Appendix A), to induce oxygen deficiency. This oxygen deficiency was increased until samples showed metallic-like conduction (decreasing conductivity with increasing temperature). Annealing was performed at 1573 K under an oxygen partial pressure of 10^{-14} atm for $(Sr_{0.61}Ba_{0.39})Nb_2O_6$ and $Sr_2(W_{0.2}Nb_{0.8})_2O_7$ and 10^{-17} atm for BST samples. Only estimates of δ are available, but BST samples have $\delta \sim 0.01$ calculated from carrier concentrations[141]. SBN samples have $\delta < 0.002$ calculated via TGA (see section 5.3.4) but show much higher carrier concentrations, on the order of 10^{21} cm^{-3}, due to A-site donors which form upon reduction. This gives a final stoichiometry of the matrix phase of roughly $(Sr_{0.61}Ba_{0.39})_{1.1}Nb_2O_6$ (see chapter 4). Where possible, paraelectric-ferroelectric phase transitions were identified by DSC or temperature dependent X-ray diffraction.[141, 142]

Electrical conductivities were measured on samples cut into rectangular bars of roughly 10 x 2 x 2 mm. Contacts consisted of silver lead wires attached to sputtered platinum electrodes bonded with silver epoxy in a 4-point probe geometry. Below 520 K electrical conductivity was measured in a Delta 9023 environmental chamber using an HP 4284A precision LCR meter. Above 520 K, samples were measured within a tube furnace with partial pressure of oxygen control, and resistance was measured via a Keithley Integra Series 2700 Digital Multimeter.

3.3 Results and Discussion

The electrical conductivities of $SrTiO_{3-\delta}$, $BaTiO_{3-\delta}$, $(Sr_{0.61}Ba_{0.39})Nb_2O_{6-\delta}$, and $Sr_2(W_{0.2}Nb_{0.8})_2O_{7-\delta}$ are shown in Figure 3-1, and confirmed paraelectric-ferroelectric phase transition temperatures are marked. Note the magnitude of the conductivity varies significantly between samples, necessitating multiple conductivity scales.

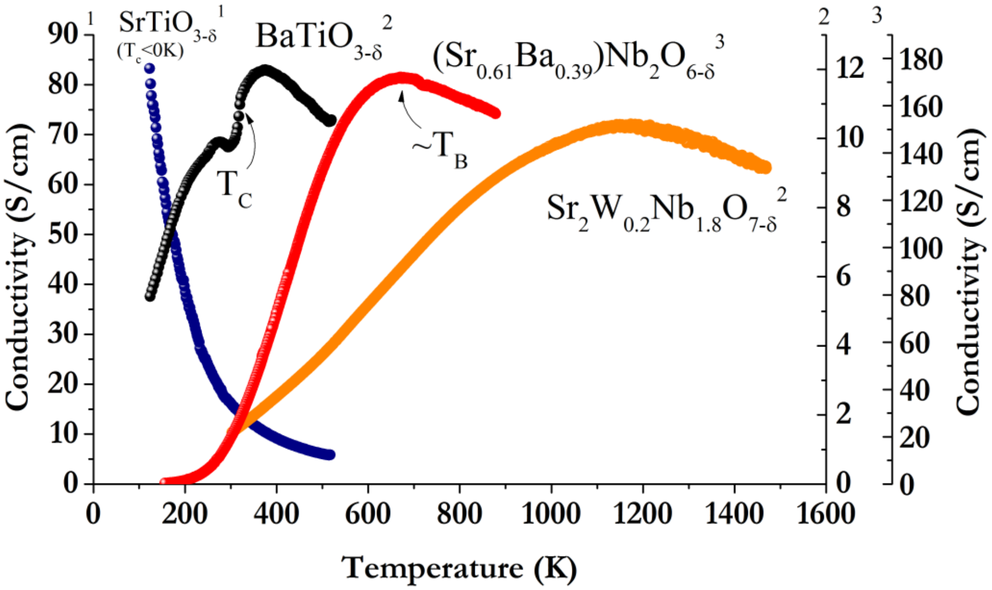

Figure 3-1. Electrical conductivity of multiple ferroelectrics which show metallic-like conduction at high temperatures. Confirmed T_c and T_{Burns} values are marked.

A transition from semiconducting $(^{d\sigma}/_{dT} > 0)$ to metallic-like behavior $(^{d\sigma}/_{dT} < 0)$, hereafter referred to as a metallic-like to nonmetallic (MLNM) transition, is seen in samples with ferroelectricity present in the insulating host compounds. The following discussion will go through each of these individually. It should be noted that metallic-like as used here means that the electrical conductivity is decreasing with increasing temperature. The true definition of a metal is the presence of a Fermi-surface, but there is no evidence here for such behavior.

Metallic-like conduction may also occur when the number of electronic carriers in constant or nearly constant but the electronic mobility is decreasing with increasing temperature, such as in the saturation regime of a semiconductor. The MLNM transitions shown here should not be confused with metal-to-insulator transitions.

The MLNM transition in $BaTiO_{3-\delta}$ occurs at ~370 K, and an additional anomaly is seen roughly 70 K below the MLNM transition. T_c of stoichiometric $BaTiO_3$ is 393 K. This suggests, at first, a correlation with the MLNM transition temperature (T_{MLNM}), but the T_c is known to decrease with increasing carrier concentration.[126] Lee et al. [141] found T_c to be ~315 K via DSC, correlating well to the low-temperature anomaly at ~300 K. It would seem then that the low-temperature anomaly is due to the paraelectric-ferroelectric transition temperature.

It is key to note that the appearance of a ferroelectric polarization does not occur exactly at T_c in $BaTiO_3$. Evidence for a finite amount of polarization has been identified in $BaTiO_3$ above T_c by finite birefringence, showing that polarization exists at least up to 50 K above T_c in $BaTiO_3$ [143]. Evidence for polar ordering was also found 180 K above T_c using Brillouin light scattering[144]. The identified polarization above T_c has aspects of relaxor ferroelectric-like[83] polarization, including its short-range order.[144] It is possible that the appearance of this relaxor-like polarization is the cause for the MLNM transition in $BaTiO_{3-\delta}$ at 370 K. The mechanism would then be Anderson localization due to the disorder created by short-range ordered polarization. That is, the electric fields and strain fields around the nanosized relaxor-like domains would be a likely source for Anderson localization which may cause the MLNM transition.

If the MLNM Transition occurs slightly above T_c, than shifts in T_c should cause shifts in the MLNM transition. Confirmation of the correlation between the MLNM Transition and T_c requires determination of T_c. Unfortunately, this is a difficult task due to the electronic carriers both lowering the latent heat of transformation and making samples too conductive for dielectric measurements. DSC measurements were performed, but were ultimately unsuccessful in measuring a precise T_c due to the small latent heat of transformation. XRD is additionally difficult simply due to the lack of proper cold stages. Fortunately, indirect confirmation of the role of T_c is still possible by utilizing the linear trend of T_c upon the substitution of Sr for Ba in $BaTiO_3$.[139, 145, 146] Electrical conductivity data for BST samples is shown in Fig. 2.

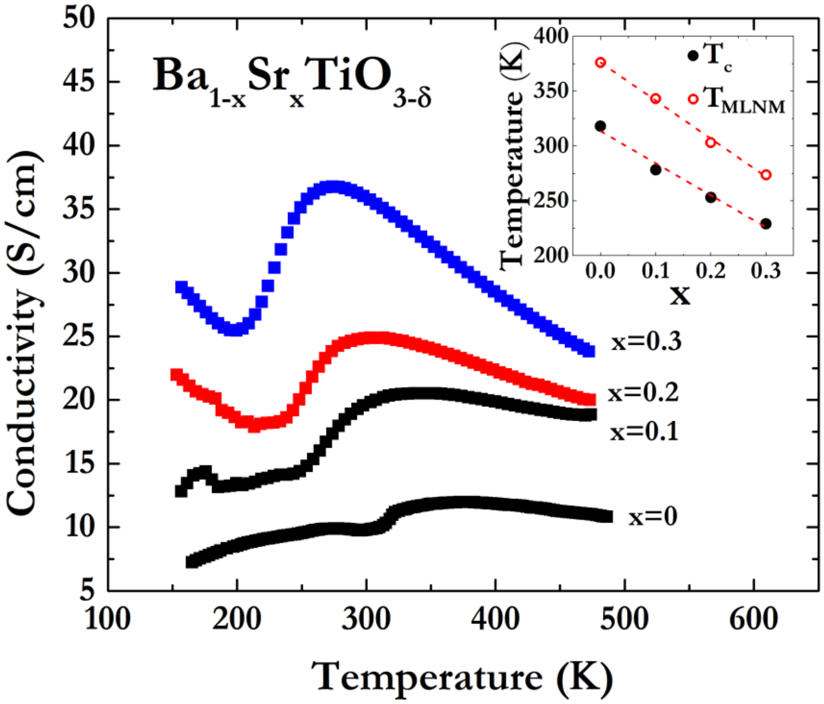

Figure 3-2. Electrical conductivity for $(Ba_{1-x}Sr_x)TiO_{3-\delta}$ ceramics annealed at 1300°C under 10^{-17} atm pO_2. As Sr% increases the electrical conductivity increases, the MLNM transition moves to lower temperatures, and a resurgence of metallic-like conduction is seen at low temperatures. The insert shows both the change in both the maximum conductivity and the inflection point, marked as T_c, as a function of the amount of Sr, x.

With the substitution of Sr for Ba, the MLNM transition decreases in temperature, and this is attributed to a decrease in T_c. The MLNM transition temperature and the anomaly associated with T_c, recorded as the inflection point, are plotted as a function of Sr substitution in the inset of Fig. 2. T_c and T_{MLNM} both follow a linear trend with slopes of 2.9°C/mol%Sr and

3.4°C/mol%Sr, respectively. These values are comparable to the expected 2.9-3.2°C/mol%Sr [139, 145, 146], and this supports the attribution of the conductivity anomalies to the onset of polarization. The increasing Sr content also causes an increase in the electrical conductivity which is attributed to the increase in electron mobility reported by Yamamoto et al. [77] Also, it is found that the conductivity anomaly is broader for BST compounds compared to $BaTiO_{3-\delta}$. This could be a consequence of heterogeneity in the local Ba and Sr concentrations or movement toward a second order phase transition. The end-member case of $SrTiO_{3-\delta}$ was also investigated, and shows metallic conduction over the entire temperature range, consistent with a nonexistent T_c.

$BaTiO_{3-\delta}$ remains semiconducting well below T_c, but a resurgence of metallic-like conduction is found in $(Ba_{1-x}Sr_x)TiO_{3-\delta}$ with x=0.1, 0.2, and 0.3 below T_c. The reason for this is currently unknown. However, possible mechanisms can be thought through. For example, it is speculated that Anderson localization from the relaxor-like polarization above T_c is the cause for the conductivity anomaly between T_c and T_{MLNM}. If this is the case, then coalescence of the polarization into long-range macroscopic domains would eliminate the conductivity anomaly. This coalescence occurs in insulating $(Ba_{1-x}Sr_x)TiO_3$ below T_c, and, if this is transferable to heavily reduced samples, the removal of the relaxor-like polarization could eliminate the Anderson localization that acts to suppress metallic-like conduction. Another possibility comes from the work of Jeong et al. [147] who used neutron diffraction to determine that cubic and tetragonal phases exist simultaneously below T_c in $BaTiO_{3-\delta}$. This coexistence allows for the possibility that metallic conduction occurs via cubic regions, and semiconduction through tetragonal regions. It may be that the resurgence of metallic-like conduction is due to the stabilization of these cubic metallic regions by Sr. This model is strengthened by the result from Levin et al. that the displacement of the individual Ti ions decrease with an increased number of Sr next-nearest neighbors.[148] If the cubic regions remain metallically conducting below T_c, then percolation of these regions could result in bulk metallic-like conductivity. The resurgence of metallic-like conductivity would then require both of these mechanisms – first, the stabilization of metallic-like cubic regions and then the removal of Anderson localization due to the coalescence of the relaxor-like polarization into macroscopic domains. Further research would be needed to confirm this model. Despite the unknown behavior of the low temperature metallic-like conductivity, it is clear that the T_c and T_{MLNM} are linked in $(Ba_{1-x}Sr_x)TiO_{3-\delta}$ and therefore the conductivity anomalies are associated with the ferroelectric polarization.

The properties of SBN are laid out in detail in chapter 4-6. A summary of the important points to this chapter are given here. SBN is a relaxor ferroelectric, and therefore the onset of polarization occurs at the Burns temperature, $T_{Burns.}$ In insulating samples T_{Burns} was measured by Bhalla et al. and Huiqing et al. to be 570-625 K and ~625 K, respectively[122, 149]. As the normal dielectric and optical measurements for determining T_{Burns} are not possible in conducting samples, temperature dependent X-ray diffraction was used to measure the electrostrictive strain associated with the polar nanoregions as shown in Figure 4-5. In contrast to T_c in normal ferroelectrics, T_{Burns} was not affected by electronic carriers and remained at 625±25K. The reason why T_c changes as a function of carrier concentration while T_{Burns} remains constant is currently unknown, and further research within this area is an interesting avenue for future work (see Chapter 4 for more detail). These values correlate well with the ~650K MLNM transition in SBN found in this work, but a link between the MLNM transition and T_{Burns} is not universal. Samples of $(Sr_{0.40}Ba_{0.60})_{1+y}Nb_2O_6$ and $(Sr_{0.50}Ba_{0.50})_{1+y}Nb_2O_6$, which are normal ferroelectric in nature, show the same MLNM transition temperature in their reduced state. This suggests that the MLNM transition temperature is independent of the polarization. Additionally, Dandeneau et al. show that the MLNM transition temperature of $(Ca_{0.18},Ba_{0.82})Nb_2O_{6-\delta}$ is ~560K while T_{Burns} is ~1200K[150]. Although the link between T_{Burns} and the MLNM transition temperature does not hold under scrutiny, the polarization was still found to have an effect on conduction. It is thought that polar nanodomains act as a source of disorder for Anderson localization which causes movement of mobility edges. In d^o oxides, this effect is pronounced as the conduction electrons lie near a band edge. In contrast, in an oxide with increased filling of the *d*-band, such as $LiOsO_3$, this effect would become less severe since Anderson localization of the band edges would not affect a Fermi edge located well within the band. [19]

The host compound $Sr_2Nb_2O_7$ has a perovskite-like layered structure and the highest T_c measured in this study, 1600 K[138]. Additions of W were needed to enhance the carrier concentration for metallic-like conduction. As the T_c is known to decrease with the introduction of electronic carriers, the MLNM transition was hypothesized to be below 1600 K. As expected, a MLNM transition was found in $Sr_2(W_{0.2}Nb_{1.8})O_7$ at 1160 K (Fig. 1). Further research must be done to confirm the correlation between the MLNM transition and T_c. Nevertheless, the expected MLNM transition was found at very high temperatures, where the only likely explanation is the introduction of polarization. Therefore, this phenomenon seems to be common over a broad temperature window across multiple ferroelectric oxides.

3.4 Conclusions

Oxygen deficient d^0 ferroelectrics with a variety of structures and paraelectric-ferroelectric transition temperatures show a metallic-like to nonmetallic transition seemingly concurrent with the onset of polarization formation. The generality of this phenomenon within different structured d^0 ferroelectrics with transition temperatures ranging over 1000 K is consistent with the model put forward by Puggioni and Rodinelli.[136] In BST samples this occurs via a MLNM transition which tracks with changes in the Curie temperature. In SBN, the link between the MLNM transition temperature and the Burns temperature is indirect, in that the polarization causes an increased localization of electrons which provides a driving force toward a semiconducting state. Additional ferroelectric-electron transport coupling mechanisms should not be overlooked; possible effects such as changes in the band structure and spatial redistribution of electronic carriers may be identified with further study.

Chapter 4
Electron Transport in $(Sr_x,Ba_{1-x})Nb_2O_{6-\delta}$ and the Effect of Relaxor Ferroelectricity

SBN has been identified as a promising ferroelectric-based thermoelectric[9], but optimization of SBN has not been undertaken. Optimization of SBN requires a clear understanding of the electron transport mechanism, which has not been previously elucidated. With the goal of understanding the electron transport mechanism in SBN, the electrical conductivity, Seebeck coefficient, and optical response were studied as a function of reduction condition. It will be shown that an odd combination of electron transport properties is found and that unclear trends as a function of reduction condition exist. These include a sharp jump in electrical conductivity as the pO_2 during annealing reaches a specific value, and the combination of an electrical conductivity which identifies band conduction and a Seebeck coefficient which seems to show hopping conduction. The former of these two oddities will be shown in this chapter as being due to a change in electron transport due to relaxor ferroelectricity.

4.1 Background

Ferroelectric materials have been of interest for multiple decades due to high electromechanical coupling coefficients, high permittivity, and high electro-optical coefficients, amongst others. These properties make them useful for high performance capacitors, piezoelectric sensors and actuators, pyroelectric detectors, electro-optic switches, electrocaloric coolers, polarization based non-volatile memories, and multiferroic sensors and switches. [151–156] A commonality of these applications is that they require the application of a sizable electric field, and this necessitates that the ferroelectric materials be insulating. Consequently, much less attention has been paid to the application possibilities for ferroelectric materials that are electrically conducting. Some applications have been found, for example, PTCR thermistors which work via changes to the electrical conductivity due to a polarization-controlled modification of the Schottky barrier at grain boundaries[157]. Recently, renewed interest in conducting ferroelectrics has revolved around polarization-aided photovoltaics [158–160] and thermoelectrics [9, 32, 141, 161], conducting domain walls [80, 81, 128, 162–164] and possibly metallic ferroelectricity [133, 134, 141, 147, 165, 166].

Investigations into metallic ferroelectrics, a topic which has been comparatively ignored since early ideas by Anderson and Blout[131] and Matthias[167], have reopened due to recent work by Kolodiazhnyi et al. [165, 166], Lee et al.[141] , and Jeong et al.[147] on heavily doped $BaTiO_3$; Sergienko et al. on $Cd_2Re_2O_7$[133]; and Shi et al.[134] on $LiOsO_3$. Metallically conducting samples with structural distortions similar to a ferroelectric have been reported [165134], but the most heavily studied of these, $BaTiO_{3-\delta}$, was later found to be inhomogeneous in nature[147]. Jeong et al. suggest that the Ti-O bond distortion (the polarization) and metallic conductivity originate from different volume fractions of the material. The polarization may locally be causing a transition into a semiconducting state. A full understanding of polarization/conduction interactions needs extensive work; however, it is possible that polarization may act as a local field to shift electron concentrations, change the degeneracy of the conduction band, or act as sources of disorder for Anderson localization.

In terms of thermoelectricity, ferroelectrics are interesting due to phonon scattering at domain walls[71168], the interaction of soft optic phonon modes with heat-carrying acoustic phonons [169, 170], and the glasslike properties in relaxor ferroelectrics [71] (see 2.2.3). All of these phenomena act to lower the thermal conductivity and should lead to higher thermoelectric figure of merits. Although relaxor ferroelectricity is beneficial for low thermal conductivity, the lack of research on conducting ferroelectrics means that its effect on the Seebeck coefficient and electrical conductivity is little explored.

Here the ability to transform SBN between relaxor and normal ferroelectricity is used to investigate the role of different types of polarization on electrical conduction. SBN is a tetragonal tungsten-bronze structured ferroelectric material (see 2.5). The Sr/Ba ratio controls the temperature of the P4mm→P4/mmm transition and if the material is a normal or relaxor ferroelectric[121]. The distinctions between normal and relaxor ferroelectrics have been extensively reviewed over the past two decades (see 2.3.1).[83171] This change from normal to relaxor ferroelectric with Sr/Ba ratio permits the exploration of trends in the Seebeck coefficient and conductivity with respect to the polarization's nature. As an extension of Chapter 3, the in-depth study of the conduction behavior of SBN may clarify how polarization plays a role in the electrical transport in both SBN and conducting ferroelectrics in general.

4.2 Experimental Procedure

4.2.1 Sample Sintering and Preparation

Powders of $(Sr_x,Ba_{1-x})Nb_2O_6$ (SBNx) were fabricated using solid-state reaction of $SrCO_3$ (>99.9%, Alfa Aesar), $BaCO_3$ (99.8%, Alfa Aesar), and Nb_2O_5 (99.9%, Alfa Aesar) precursor powders. These powders were weighed in the required stoichiometric ratios and mixed via ball milling in ethanol with ZrO_2 media for 12 hours. The dried powders were calcined at 1200°C for 6 hours. The high calcination temperatures and long calcination times are needed to homogenize the cation distribution and prevent Nb-rich or Ba-poor regions which result in abnormal grain growth, as discussed by Lee and Freer[140]. The calcined powders were ball milled for 24 hours using ZrO_2 media in ethanol and then sieved using a No. 80 mesh size. The milled powders were uniaxially pressed at 15 MPa and subsequently isostatically pressed at 210 MPa. Further precautions against abnormal grain growth were taken by using a 2-step sintering process. That is, pellets were first held at 1250°C for 6 hours to further homogenize and then ramped to 1325°C for 6 hours to sinter. All samples were phase pure by X-ray diffraction and >95% dense after sintering.

Dense pellets were made electrically conducting via annealing in low partial pressures of oxygen. The annealing atmosphere was controlled using H_2-H_2O gas mixtures with a nitrogen carrier gas. To investigate the properties as a function of annealing pO_2, samples of SBN0.6 were annealed under partial pressures of oxygen ranging from 10^{-10} to 10^{-16} atm at 1300°C for 30 hours. To investigate the properties as a function of relaxor ferroelectric character, samples of SBN0.4-0.7 were annealed under a partial pressure of oxygen of 10^{-14} atm at 1300°C for 30 hours. Cooling was performed under a constant pH_2-pH_2O mixture at 15°C/min. Phase compositions of annealed samples were investigated using x-ray diffraction on a PANalytical Empyrean using scan conditions of 20-60° 2θ, a 0.02° step size, and a scan speed of 109 sec/°. All samples annealed below 10^{-12} atm pO_2 formed an NbO_2 second phase. Nb_2O_5 which was converted into NbO_2 via annealing at 1300°C under 10^{-14} atm was found to have a conductivity on the order of 10 S/cm at 700K, in rough agreement with previous reports[172]. The low conductivity of the NbO_2 phase and the lack of percolation in the microstructure suggests that the phase should not contribute heavily to electronic conduction. It was found that the NbO_2 phase indicates changes in the chemistry of the SBN matrix which increases electrical conduction. This will be discussed in detail in Chapter 5. Annealed samples were cut using a diamond saw into bars of 10 x 1.5 x 1.5mm and 6x1x1mm dimensions for electrical conductivity and Seebeck coefficient measurements, respectively. The surfaces of bars were prepared via polishing with SiC sandpaper starting with 400 Grit working down to 1200 Grit.

4.2.2 Electron Transport Measurements

Electrical conductivity measurements were performed via a four terminal technique with Ti/Pt electrodes deposited as films via sputtering using a shadow mask. Ag wires were then attached with Ag epoxy and cured at 120°C for 2 hours. Electrical conductivity at temperatures below 520 K was measured in a Delta Design 9023 environmental test chamber, using an HP 4284A precision LCR meter. Higher temperature measurements were performed using a Keithley 2700 Integra series digital multimeter with leads fed into a tube furnace equipped with pH_2-pH_2O atmosphere control. Samples were measured under the same H_2 and N_2/H_2O flow rates that were used for their annealing to minimize oxidation during measurement. It was found that the electrical conductivity magnitudes were consistent on both heating and cooling over multiple measurements, suggesting that any minor changes in oxidation do not play a significant role in the measurements.

The Seebeck coefficients, S, of samples were measured primarily on a SB100 Seebeck coefficient measurement system by MMR Technologies from 200 to 600 K. The SB100 uses the integral method for determining the Seebeck coefficient. Samples had Ti/Pt electrodes sputtered on the ends to assure ohmic contacts, and then were connected to the stage using silver epoxy which was cured at 120°C for two hours. A heater was used to simultaneously apply a temperature gradient onto both the sample under test and a reference sample. The Seebeck voltage is measured from both the reference sample and the sample under test. The voltage from the reference sample is used to determine the temperature gradient over the reference sample. This temperature gradient is assumed to be the temperature gradient over the sample under test. To assure this assumption was valid, great care was used in determining that the sample under test and the reference sample were symmetrically placed in relation to the heater. The Seebeck coefficient is calculated from the Seebeck voltage from two different applied temperature gradients.

One 5×5×20mm sample of SBN0.6 was measured using a ZEM-3 thermoelectric measurement system at NASA Glenn Research Center. The ZEM-3 system uses the differential method for measurement of Seebeck coefficient. In this method, thermocouples are used as voltage leads so that the temperature gradient can be measured directly at the voltage measurement position. An internal heater sweeps the temperature gradient and the Seebeck coefficient is calculated using the slope of the ΔV vs ΔT plot. Good correlation exists between the MMR and ZEM-3 measurement systems; the ZEM-3 system has a lower noise floor, as well as the capability for higher temperature measurements and atmosphere control. The SBN0.6 sample was measured under a 0.1atm He atmosphere up to 750K, above which sample reoxidation became problematic.

Optical conductivity was determined for ceramic SBN0.6 pellets annealed at partial pressures of oxygen ranging from 10^{-10} atm to 10^{-16} atm at 1300°C for 30 hours. The pellets were polished down to a 0.25 μm finish. Ellipsometry data were collected at three different incidence angles (55°, 65°, 75°) using a J. A. Wollam Co. (Lincoln, NE) M-2000 rotating compensator spectroscopic ellipsometer. Specular reflectance measurements were performed using a Bruker Vertex 70 with a Hyperion 3000 FT-IR microscope attachment. The optical conductivity was determined from the ellipsometry and reflectivity data via a Kramers-Kronig constrained variation analysis as explained in Ref. [173]. The analysis was performed using RefFIT software.

4.2.3 Temperature Dependent X-ray Diffraction Measurements

Lattice parameters as a function of temperature were measured on $(Sr_{0.61},Ba_{0.39})Nb_2O_6$ annealed at 1300°C under 10^{-14} atm and then crushed into powder form. The powder was mixed with NIST standard reference material 674a alumina and placed into a 1 mm diameter quartz capillary. A vacuum was pulled on the capillary, which was then backfilled with 1% H_2/N_2 forming gas. The cycle of evacuation and backfilling with forming gas was repeated >10 times. While under an atmosphere of forming gas, wax was melted in the quartz capillary to seal it. Temperature dependent lattice parameters were then measured using a custom-built furnace on APS beamline 6-ID-D. The alumina powder was used as an internal standard to correct for temperature by using the thermal expansion data measured by Brown et al.[174] Lattice parameters were used to calculate the *c/a* ratio in the SBN material. The Burns' temperature (T_{Burns}) was found by identifying the deviation of the *c/a* ratio on cooling from the high-temperature linear trend. This deviation is expected for relaxor ferroelectrics due to the polarization fluctuation's contribution to strain. The magnitude is given by $x_i = Q_{ij}\overline{P_j^2}$ where x_i is strain, Q_{ij} is the electrostrictive coefficient, and $\overline{P_j^2}$ is the average magnitude of the short-range order polarization in the system[149]. Only Q_{ij} values for SBN0.75 are available, and are $Q_{31} = 0.71x10^{-2}\, {m^4}/{C^2}$ and $Q_{33} = 3x10^{-2}\, {m^4}/{C^2}$[175].

4.3 Results and Discussion

4.3.1 Electron Transport as a Function of Reduction

The electrical conductivity of SBN0.6 annealed in atmospheres from N_2 (~10^{-6} atm pO_2) to 10^{-16} atm pO_2 is shown in Figure 4-1.

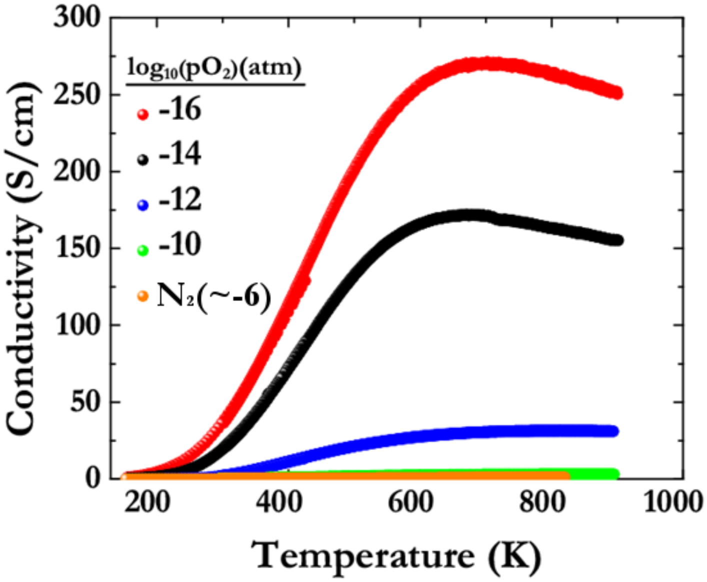

Figure 4-1. Electrical conductivity of $(Sr_{0.6},Ba_{0.4})Nb_2O_{6-\delta}$ annealed under partial pressures of oxygen ranging from 10^{-7} to 10^{-16} atm.

Samples annealed at 10^{-14} and 10^{-16} atm pO_2 clearly show semiconducting ($d\sigma/dt>0$) behavior at low temperatures and metallic-like behavior ($d\sigma/dt<0$) at high temperatures. The phrasing 'metallic-like' is used only to describe that $d\sigma/dt<0$ and does not necessarily mean the Fermi energy (E_F) is located in a band of delocalized electronic states, as in a true metal. Obviously, a maximum in conductivity occurs at the transition from semiconducting to metallic-like behavior. Here it will be denoted by the temperature of the maximum conductivity, $T_{\sigma Max}$. It has been reported previously in samples of SBN0.6 annealed at 10^{-14} atm pO_2 at 1300 °C that $T_{\sigma Max}$ coincides with the T_{Burns} of unreduced samples (see Chapter 3).[32] This correlation was used to hypothesize that the polarization could suppress metallic conduction. A possible mechanism involved a spatially heterogeneous mixture of paraelectric metallic and ferroelectric semiconducting phases, similar to ideas Jeong et al. put forward for $BaTiO_{3-\delta}$ [147].

An alternate explanation for the maximum in conductivity could be that the semiconducting nature is due to incomplete ionization of donors. In this scenario the semiconducting to metallic-like transition would be simply the saturation temperature for donor ionization. The saturation temperature, T_s, is carrier-concentration dependent. That is[30],

$$T_s = \frac{E_d}{kln(\frac{N_c}{N_d})} \tag{4.1}$$

where N_c is the density of states at the bottom of the conduction band, N_d is the donor concentration, and E_d is the donor ionization energy. Therefore, in this model $T_{\sigma Max}$ would be reduction-dependent via changes to N_d and E_d. The N_d increases with reduction whereas E_d should decrease with reduction. The decrease of E_d with reduction occurs due to the spreading out of the impurity band with increasing carrier concentration (see section 2.1.3). These dependences on reduction push the saturation temperature in opposite directions. Changes in T_s therefore depend on the specifics of how N_d and E_d change with carrier concentration. The key first step was to determine either if the carrier concentration dependence exists, or if $T_{\sigma Max}$ is pinned at T_{Burns}.

Samples of SBNx annealed under different reduction conditions have been measured in the current study, by Dandeneau et al.[176], and by Li et al.[177]. As is seen in Figure 4-1, samples annealed at 1300°C under $pO_2=10^{-14}$ atm and 10^{-16} atm show $T_{\sigma Max}$ at ~680K. In chapter 6 it will also be shown that the $T_{\sigma Max}$ is invariant in single crystals annealed at 1300°C under 10^{-14}, 10^{-15}, and 10^{-16} atm. However, for samples annealed under $pO_2=10^{-12}$ atm, $T_{\sigma Max}$ is at ~820K and, although hard to see in Figure 4-1, the pO_2 ~10^{-6}-10^{-10} atm samples have not yet reached $T_{\sigma Max}$ within the measured temperature range. This suggests that at low carrier concentrations $T_{\sigma Max}$

varies substantially while at higher carrier concentrations $T_{\sigma Max}$ becomes pinned near T_{Burns}. In the current dataset, the switch from a carrier concentration dependent $T_{\sigma Max}$ to an invariant $T_{\sigma Max}$ coincides with NbO_2 formation.

Direct comparisons to literature samples are impossible without carrier concentration data, but inferences can be useful if annealing conditions and electrical conductivities are used as substitutes for comparison. Dandeneau et al. annealed SBN0.5 under forming gas at various annealing temperatures ranging from 1000°C to 1150°C.[176] A later study by Dandeneau showed that the sample annealed at 1000°C showed an NbO_2 secondary phase [178] The peak electrical conductivities ranged from ~55S/cm to 125S/cm, and $T_{\sigma Max}$ was ~600-700K for all samples. Therefore, a ~2.3x change in the maximum electrical conductivity occurs with no discernable change in $T_{\sigma Max}$. However, in the work of Li Ye et al. [177] it is shown that a change in $T_{\sigma Max}$ occurs between SBN0.61 samples annealed in pure Argon at 1100°C (phase pure) and a sample annealed in forming gas at 1250°C (NbO_2 present) . Given the sum of these results, it is likely that $T_{\sigma Max}$ becomes pinned once NbO_2 forms, but a systematic study over a larger range of pO_2 values is necessary for confirmation. The pinning of $T_{\sigma Max}$ occurs near T_{Burns} determined from stoichiometric compositions, but it is unclear given the current data if this is correlation or causation. Clarity on this question requires further study of the electron transport mechanism in SBNx. This discussion will be continued in the next section.

The Seebeck coefficients of SBN0.6 as a function of reduction are shown in Figure 4-2a. The Seebeck coefficient decreases with increasing reduction, as expected due to increasing carrier concentrations. More specifically, in samples annealed above 10^{-12} atm pO_2, the Seebeck coefficient decreases linearly with logarithmically decreasing values of pO_2 during annealing (Figure 4-2b). Samples annealed below 10^{-12} atm pO_2 show a deviation from this linear behavior, presumably due to the formation of NbO_2. The Seebeck coefficient seems to be roughly temperature independent, which is indicative of small polaron hopping.[107] Specifically, linear fits of S vs T for these samples result in slopes in the range of -0.08 µV/K^2 to 0.05 µV/K^2. Temperature invariant Seebeck coefficients were also reported in studies by Lee et al. on textured SBN0.6 ceramics.[161] However, the temperature independence of the Seebeck coefficient is not generalizable to all samples, as pointed out by Lee et al. in studies on SBN single crystals [9]. Additionally, the seemingly polaronic dependence of the Seebeck coefficient is unlikely due to the carrier concentration measurements presented in 5.3.4. The next section discusses how this temperature independent nature is not due to the Heike formula (see 2.4.2), but due to the role relaxor ferroelectricity plays in modifying the electron transport.

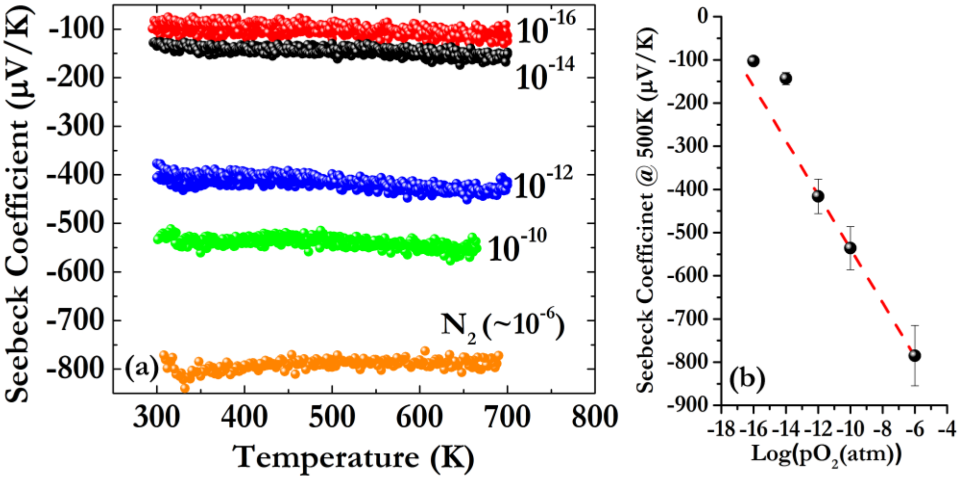

Figure 4-2. (a) Seebeck coefficient vs. temperature and (b) values of Seebeck coefficient at 500K for different reduction conditions of SBN0.6. The magnitude of the Seebeck coefficient is roughly temperature independent. It is noted that the Heike formula (Equation (2.57)) for temperature independent Seebeck coefficients is not valid here, as explained in 3.3.2. Error bars on (b) are a +-10% systematic error based on the loading and reloading of a sample multiple times into the MMR system.

The optical conductivity of SBN0.6 as a function of reduction was also measured in an attempt to investigate possible polaronic hopping behavior. At T=0K, absorption due to a small polaron exists as an absorption band peaked at four times the hopping energy, E_{Hop} from Equation (2.12).[179] The optical conductivity of SBN is shown in Figure 4-3.

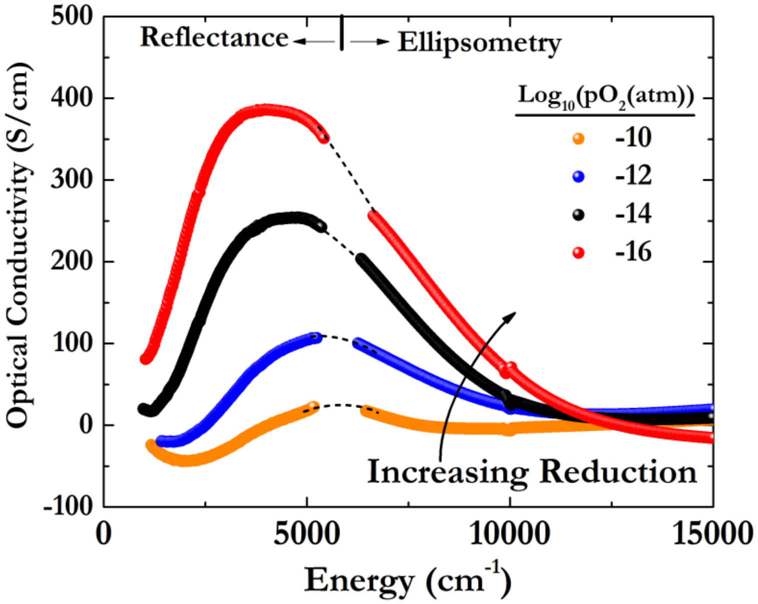

Figure 4-3. Optical conductivity of $(Sr_{0.6},Ba_{0.4})Nb_2O_{6-\delta}$ from 10^{-10} atm pO_2 to 10^{-16} atm pO_2 measured via combination of FTIR and ellipsometry. The peak should be located near $4E_{Hop}$. Low energy tails are an artifact of data analysis due to the FTIR dataset ending in the middle of an absorption peak.

The activation energy for hopping can be estimated from Figure 4-3 using the peak conductivity. Table 4-1 compares the hopping energy from Figure 4-3 and from fits of $\ln(\sigma T)\ vs.\ (k_b T)^{-1}$ for the data in Figure 4-1.

Table 4-1.

Annealing Atmosphere (atm)	E_{Hop}(eV)	
	Optical Conductivity	Electrical Conductivity
10^{-10}	0.26	0.18
10^{-12}	0.21	0.16
10^{-14}	0.16	0.14
10^{-16}	0.14	0.12

Unfortunately only qualitative comparisons can be made. This is because the peak energy is quantitatively equal to four times the hopping energy only at T=0K and for sufficiently strong electron-phonon coupling strengths[179]. As the data in Figure 4-3 were taken at room temperature, the activation energies given from optical methods in Table 4-1 are estimates. These estimates do, however, sit within the correct regime when compared to the activation energy found from DC electrical conductivity. Caution should be stressed in the above interpretation. Similar mid-IR absorption bands have been seen in $La_{2-x}Sr_xCuO_4$[180], Nd:$SrTiO_3$[181], and $BaTiO_{3-\delta}$[182], but interpretation of their cause is scattered. Interpretations range from absorption due to small polaron hopping [183], to absorption arising from oxygen vacancy related defects [184], to incoherent electron-phonon coupling causing spectral weight transfer from the Drude peak via phonons [181]. Unfortunately little can be said without an underlying theory of the mechanism behind the mid-IR band. Further work is clearly necessary.

4.3.2 Effect of Relaxor Ferroelectricity on Electron Transport in SBN

The electrical conductivities as a function of temperature for SBN0.4 through SBN0.7 are plotted in Figure 4-4. The $T_{\sigma Max}$ for SBN0.4, SBN0.5, and SBN0.6 occur around 680K, while $T_{\sigma Max}$ for SBN0.7 was outside the measurement range, >900K. Although the maximum conductivity in SBN0.4-0.6 occurs near T_{Burns} as measured in stoichiometric compositions of SBN0.6 [123], the maximum conductivity of SBN0.7 is at much higher temperatures. This is inconsistent with the idea that the conductivity maxima are fundamentally linked to T_{Burns}. However, the high temperature conductivity maxima of SBN0.7 presented here has been brought into question due to later work conducted by Li et al. [185]. Li et al. show that SBN0.7 samples have a $T_{\sigma Max}$ at ~650K which is consistent with T_{Burns}. This inconsistency between the two results is troubling, but if the work of Li et al. is taken as correct, it brings SBN0.7 into line with SBN0.4-0.6. It is unclear why the SBN0.7 samples in this current dataset show different properties than those of Li et al., but it should be noted that the data in this thesis were confirmed on three independently annealed samples from two independent powder batches of SBN0.7. Therefore, although a link between $T_{\sigma Max}$ and T_{Burns} may be possible in SBN, it is unlikely to be general. The lack of generality is in agreement with the result of Dandeneau et al., which shows that the $T_{\sigma Max}$ of $(Ca_{0.18},Ba_{0.82})Nb_2O_{6-\delta}$ is ~560K while T_{Burns} is ~1200K[150]. The lack of a link between $T_{\sigma Max}$ and T_{Burns} does *not* mean electrical conductivity is unaffected by relaxor ferroelectricity. It only means that the effects may be more subtle than a simple correlation between $T_{\sigma Max}$ and T_{Burns}. Before further study into the subtleties of the conduction mechanism in SBN, it is important to determine the effect of the reduction procedure on T_{Burns}.

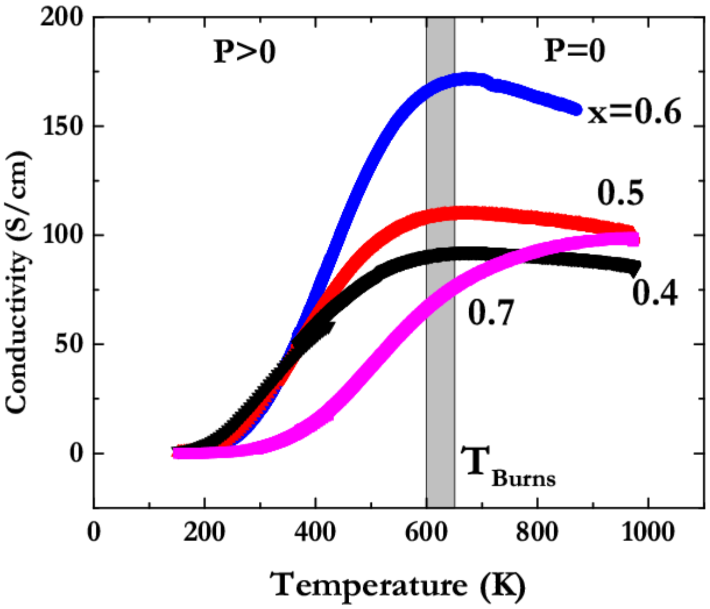

Figure 4-4. Electrical conductivities of $(Sr_x,Ba_{1-x})Nb_2O_{6-\delta}$ for SBN0.4-0.7 from 150K to 1000K. Measurements at temperatures greater than ~450K were performed under a reducing atmosphere consistent with the pO_2 used during sample annealing. Maxima for SBN0.4-0.6 are located near T_{Burns}, while SBN0.7 has a maxima shift to higher temperatures.

Any line of thinking that tries to link relaxor ferroelectric polarization and electrical conductivity must start with an understanding of T_{Burns} in reduced samples. To check how the T_{Burns} is modified by reduction in SBN, temperature dependent lattice parameters were taken on beamline 6-ID-D at the Advanced Photon Source, Argonne National Laboratories. The trend is clearest when plotted as *c/a* ratio, which is shown for SBN0.6 in Figure 4-5.

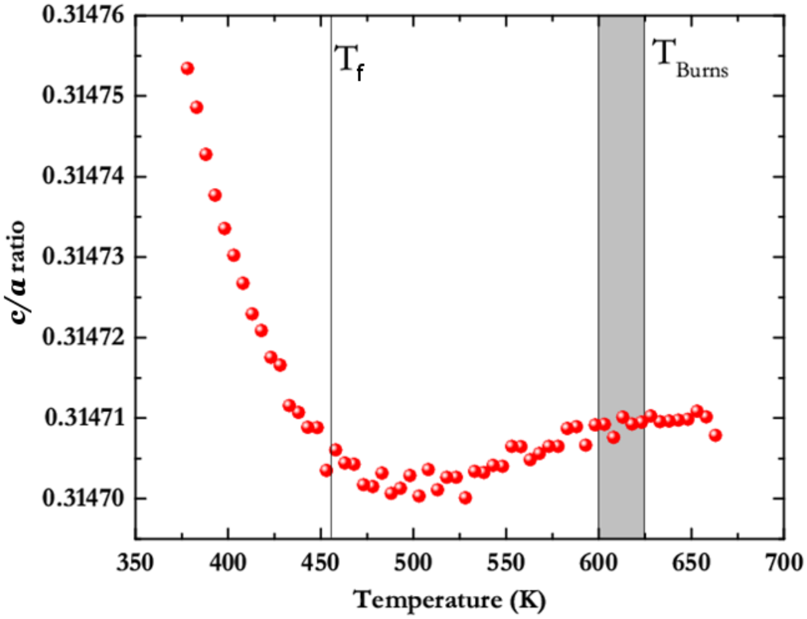

Figure 4-5. The *c/a* ratio of a SBN0.6 sample from 375K to 660K. A linear dependence is seen >~625K, suggesting paraelectric behavior. A decrease in *c/a* ratio is due to the short-range-order polarization between 450K and 625K, and an increase is found <450K associated with the freezing in of mesoscale polar nano-regions.

At temperatures above T_{Burns}, the *c/a* ratio remains roughly constant. There is a decrease in the *c/a* ratio on cooling at ~625K. This decrease is associated with the electrostrictive coupling of polarization to lattice strain. As the nanopolar regions are formed, the polarization along the *c*-axis causes both the *c* and *a*-axis lattice parameters to increase due to electrostriction[175]. Although the electrostrictive coefficient Q_{33} is larger than the Q_{13} coefficient, the larger *a*-axis lattice parameter (*a*=12.44 Å vs. *c*=3.96 Å at room temperature) makes the *c/a* ratio decrease on cooling, as can be seen in Figure 4-5 below ~625K. As the temperature is lowered below 450K, an increase in the *c/a* ratio occurs. This is associated with the immobilization of mesoscale polar nanoregions, as described elsewhere.[186] Thus, T_{Burns} for this oxygen deficient SBN is 625 ± 25K, which is comparable to the T_{Burns} in stoichiometric samples of 600K ± 25K[175] and therefore appears to be essentially invariant to the reduction condition. Therefore, the T_{Burns} does not seem to be heavily dependent on carrier concentration and the T_{Burns} from stoichiometric compositions was utilized in further analysis. This is in contrast to the Curie temperature in normal ferroelectrics, which has been shown to be dependent on carrier concentration [187141].

The model of electron transport in SBN also needs to be clarified. Clearly the high temperature and low temperature regimes of SBN show different behaviors; therefore, the two temperature regimes were investigated. To elucidate the conduction mechanism in SBN at low temperatures, the natural logarithm of conductivity is plotted versus $T^{-1/4}$ in Figure 4-6.

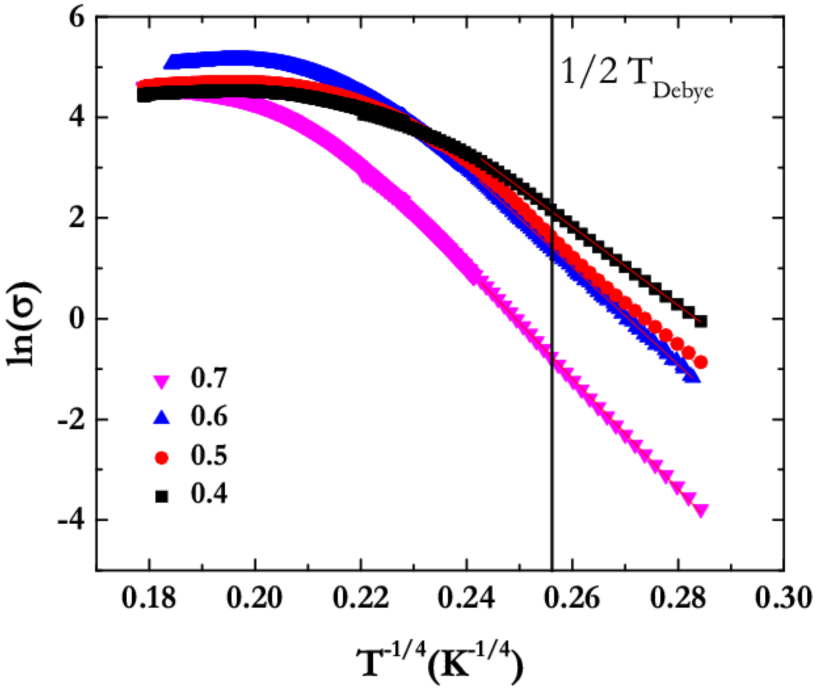

Figure 4-6. $T^{-1/4}$ behavior of the conductivity is found below ~270K for all samples. Emin[47] suggests this may be due to loss of multiphonon hopping processes below ~$1/2T_{Debye.}$ The value for $1/2T_{Debye}$ for SBN0.6 found by Henning[188] is plotted and agrees with the onset of $T^{-1/4}$ behavior.

A linear $\ln(\sigma)\ vs.\ T^{-1/4}$ behavior is found for temperatures below ~270K, with the onset being slightly dependent on Sr/Ba ratio. There are two different possibilities for this behavior.

First, at temperatures below $\sim\frac{1}{2}T_{Debye}$ a $T^{-1/4}$ behavior is indicative of small polaron hopping. That is, since small polaron hopping requires interaction with phonons[189], the lack of high-energy phonon modes below ~$1/2T_{Debye}$ results in $T^{-1/4}$ behavior, as discussed by Emin[47]. The Debye temperature in SBN was found to be 460K by Henning et al.[188, 190]. $1/2T_{Debye}$ is marked on Figure 4-6 and is shown to correlate with the onset of $T^{-1/4}$ behavior. Secondly, variable range hopping, as described in 2.1.4, would be expected if the Fermi energy sits within a finite density of localized states. Dandeandu et al. go through an analysis of variable range hopping behavior for SBN.[191] Using conductivity data augmented with the density of states at the Fermi level measured by XPS, it was shown that the expected electron wave decay length was 5.5Å, close to the Nb-O-Nb distance. This agreement of VRH analysis with a believable localization length for electrons suggests that VRH may be occurring, but further research is needed to resolve whether variable range hopping or short range hopping dominates in this temperature range.

At sufficiently high temperatures, small polaron conduction follows the well-known equation $\sigma = \frac{\sigma_o}{T} exp\left(\frac{-E_{Hop}}{kT}\right)$, where E_{Hop} is the activation energy for hopping. Therefore, at higher temperatures the conduction should show a linear relationship between $\ln(\sigma T)$ and $1/_{kT}$ with a slope equal to E_{Hop}. A plot of $ln(\sigma T)\ vs\ 1/_{kT}$ is shown in Figure 4-7.

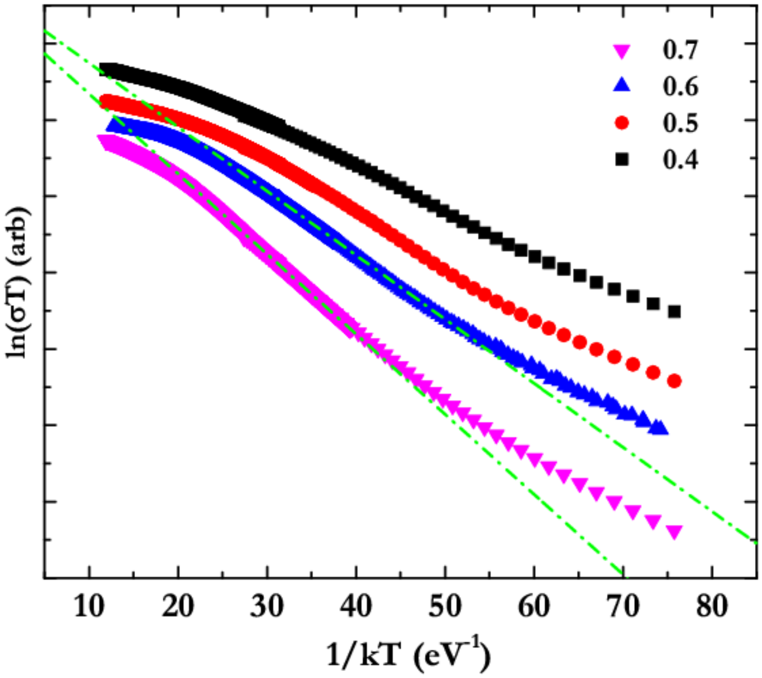

Figure 4-7. Natural log of electrical conductivity-temperature product plotted against reciprocal thermal energy. A linear dependence is expected for small polaron controlled conduction. Areas of SBN0.7 and SBN0.6 samples are linear, suggesting this mechanism within a small temperature window, but high and low temperatures deviate from this dependence.

A line can be fit for a small region between ~300K and 450K for SBN0.7 and SBN0.6, but the plot clearly becomes nonlinear at higher temperatures. No linear fits can be made for SBN0.5 and SBN0.4 in any temperature regime. It would seem then that a small polaron picture of conduction may be confined to the low temperature regime and cannot explain the high-temperature properties.

The change from hopping conduction at low temperatures toward metallic-like conduction as temperatures increase is suggestive of movement from conduction via donor states to conduction via band states. That is, the ionization of donor states into the conduction band may be occurring. To better understand this process, it is helpful to look at the activation energy for donor ionization. This is usually done via fitting a line to a ln(σ) vs $(kT)^{-1}$ plot assuming a temperature-independent activation energy. Figure 4-7 suggests that the activation energy in the high temperature regime is temperature dependent and therefore the temperature-dependent activation energy must be obtained via differentiation of the ln(σ) vs $(kT)^{-1}$ plot. Assuming a conductivity dependence of $\sigma = \sigma_o exp\left(\frac{-E_\sigma}{kT}\right)$, the differential activation energy is $E_a(T) = \frac{dln(\sigma)}{d(1/_{kT})}$. This calculation was done numerically using the data from Figure 4-8 and is re-plotted in this differentiated form in Figure 4-8.

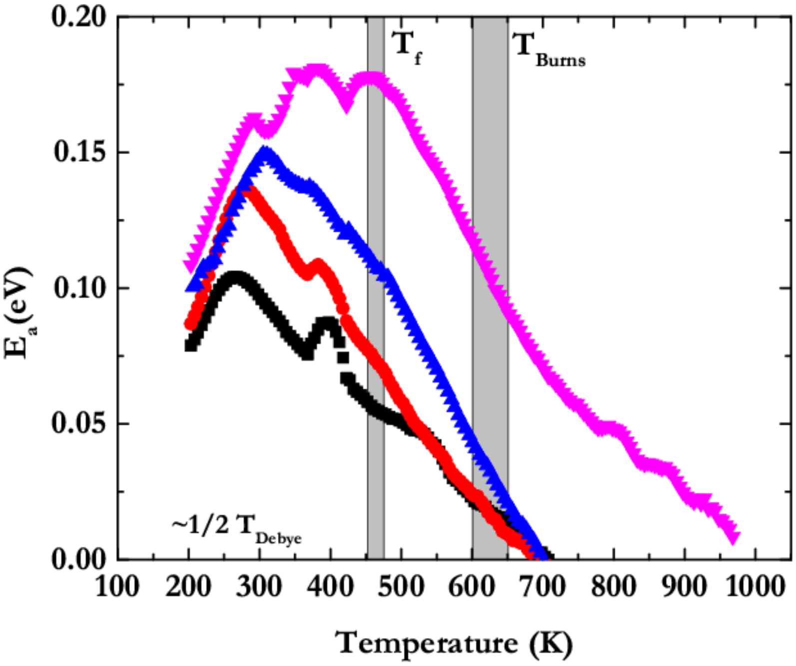

Figure 4-8. Temperature dependent activation energies calculated from electrical conductivity data. Changes in slope are found at 450K and 625K associated with the changes in polarization in the sample, as discussed in the text.

Multiple regions exist with different values of the slope, $\frac{dE_a}{dT}$. As discussed in 2.1.2, a linear change in the activation energy can be due to the temperature dependence of the conduction band edge. The values of $\frac{dE_a}{dT}$ range from 2.5x10^{-4} eV/K to 5x10^{-4} eV/K and are comparable in magnitude to the change in band gap with temperature for SBN, ~10x10^{-4} eV/K[192]. The activation energies of <0.2eV are roughly consistent with donor ionization energies assuming a hydrogen-like model [98]. This suggests activation from donor states or, if the carrier concentration is large enough, an impurity band. As shown in Chapter 5, the carrier concentration of these samples is roughly ~10^{21}/cc and therefore an impurity band is expected.

The $\frac{dE_a}{dT}$ is dependent on the temperature regime. Low temperatures show a positive slope, as is expected for $\ln(\sigma) \propto T^{-1/4}$ behavior. For SBN0.4 a transition from positive to negative slope is found near 270K and is attributed to the transition from hopping conduction to electron activation into bands. This transition from $T^{-1/4}$ behavior to activation into delocalized states seems to skip over the regime where small polaron hopping follows Equation (2.12). The broader transition from positive to negative $\frac{dE_a}{dT}$ for SBN0.7 may be associated with a constant $E_a(T)$ which follows from Equation (2.12). This would explain why a small region in Figure 4-7 fits a line well.

Changes in $\frac{dE_a}{dT}$ are found near both 450K and 630K, which correlate well to T_f and T_{Burns}, respectively. For example, in the SBN0.7 sample, there is, on cooling, an increase in $\frac{dE_a}{dT}$ around 630K from $2.2\text{x}10^{-4}$ eV/K to $5\text{x}10^{-4}$ eV/K, and then a decrease to $0.3\text{x}10^{-4}$ eV/K below 450K. SBN0.4-0.6 samples, whose maximum conductivity is near the T_{Burns}, show the appearance of a finite $E_a(T)$ value at this point. SBN0.4 and SBN0.5 show no change in $\frac{dE_a}{dT}$ at T_f, likely due to their normal ferroelectric nature and therefore lack of the dynamic short-range order polarization as observed in SBN0.6 and SBN0.7. The increase of $\frac{dE_a}{dT}$ at T_{Burns} suggests that $\frac{dE_a}{dT}$ has two contributions – one due to the temperature dependence of the conduction band edge and one due to the relaxor ferroelectric polarization. SBN0.4 shows only the contribution of $\frac{dE_a}{dT}$ due to the temperature dependence of the conduction band edge. As the Sr concentration increases the relaxor ferroelectric nature increases, and increased $\frac{dE_a}{dT}$ causes the increased values of E_a shown in Figure 4-8.

Given the current data, the most likely model is one of electrons activating from an impurity band above a mobility edge in the conduction band. The data agrees well with the expected trends in electrical conductivity laid out in 2.1.3 including the relative size of the activation energy, the temperature dependence of the activation energy, and the presence of $T^{-1/4}$ behavior at low temperatures. The presence of electronic states roughly 3eV above the O_{2p} edge in reduced SBN was found via XPS by Dandeneau et al. [191], agreeing with the presence of donor states in the band. A schematic of this impurity band model is given in Figure 4-9.

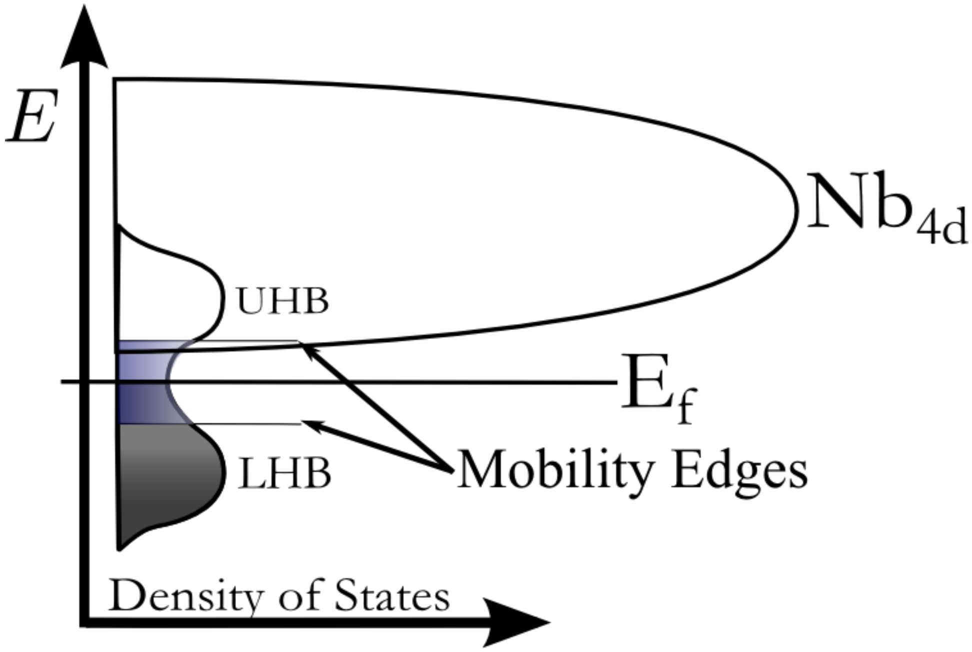

Figure 4-9. Proposed density of states for oxygen deficient strontium barium niobate. The donors create an impurity band which splits into upper (UHB) and lower (LHB) Hubbard sub-bands. The Fermi energy is located between the upper and lower sub-bands within localized states which are separated from delocalized states via mobility edges as shown. Comparison to Figure 2-6d is useful.

The mobility edges are present due to the Anderson localization of electrons, the extent of which is dependent on the disorder in the system. Some disorder occurs in the paraelectric phase due to the solid solution of Sr and Ba’s as well as oxygen vacancies. Here, it is proposed that the nanopolar regions act as an additional source of disorder. As such, the increase in $\frac{dE_a}{dT}$ below the T_{Burns} is attributed to the disorder from the nanosized domains which grow in number and size as temperature decreases below T_{Burns}. The increased disorder would move the mobility edge away from the E_F and result in a decrease in the electrical conduction due to the increased localization of electrons. Once the T_f is reached the polarization would stop influencing the activation energy further, and changes in the activation energy would again be controlled by the temperature dependence of the band. This transition occurs and is associated, for example, with a decrease in $\frac{dE_a}{dT}$ from 5x10^{-4} eV/K to 2.5x10^{-4} eV/K in SBN0.6 at 450K. In this model, no changes to $\frac{dE_a}{dT}$ occur in SBN0.4 and SBN0.5 because of the lack of relaxor ferroelectric polarization. The long-range order of the polarization should not cause the Anderson localization necessary to move the mobility edge away from E_f.

Further insight can be gained through looking at the Seebeck coefficient as shown in Figure 4-10. It is clear that the temperature invariant Seebeck coefficient shown in Figure 4-2 does not appear in samples of all Sr/Ba ratios. In fact, a trend exists from a negative $\frac{dS}{dT}$ for SBN0.4 to a positive $\frac{dS}{dT}$ for SBN0.7, and the temperature invariance of the Seebeck coefficient of SBN0.6 simply seems to exist at the crossover between these two extrema. It is clear then that the Heike formula is not applicable to SBN0.6.

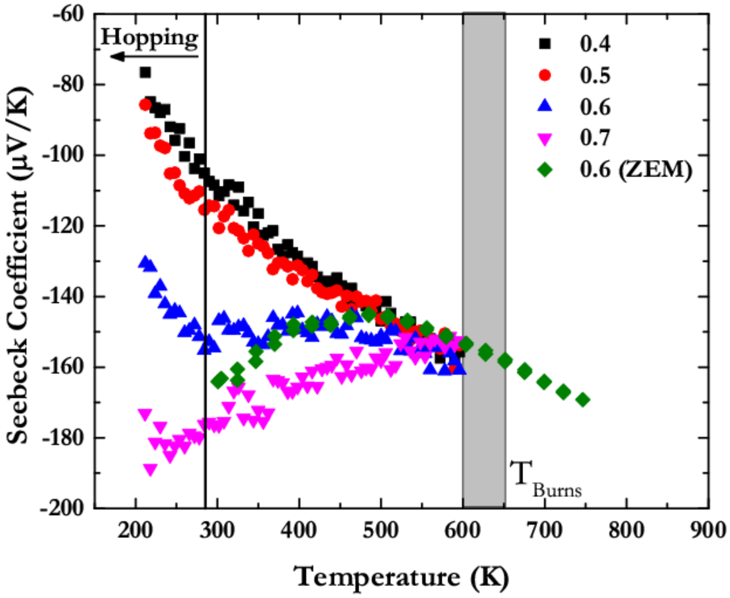

Figure 4-10. 3-point moving average of measured Seebeck coefficients of $(Sr_x,Ba_{1-x})Nb_2O_{6-\delta}$ from 200K to 600K and an SBN0.6 sample measured from room temperature to 750K. The Seebeck coefficients of all samples coincide at the Burns temperature, and the SBN0.6 sample continues the trend of the normal ferroelectric SBN0.4 and SBN0.5 samples above the Burns temperature. This suggests that the nonlinearity found in the SBN0.6 and SBN0.7 samples is due to the relaxor ferroelectric polarization.

To understand the data in Figure 4-10, comparisons were made to $Ce_{3-x}S_4$, which also shows an Anderson localized band. Cutler and Mott explained the Seebeck coefficients data in detail [193] for the low temperature range based on the idea that when $k_bT \ll E_m - E_f$ the conduction electrons are located within a band centered on E_f with a width of k_bT. This is similar to a metal, and it was shown that the Seebeck coefficient reduced to the Mott formula, Equation (2.51), where the Seebeck coefficient is linearly dependent on temperature. It should be noted that this only holds true when conductive electrons are only those from localized states. Therefore, transport is dominated by hopping behavior between states around E_f. As temperature increases, electrons will be activated above the mobility edge and will quickly dominate conduction due to their higher mobility. If a gap exists between the impurity band and the conduction band then the scenario should be similar to Equation (2.54) where electrons are activated over a gap, and then $S \propto \frac{1}{T}$ (Table 1-1). If instead no gap is present an $S \propto \ln(T)$ dependence is expected (see 2.4.2). It is clear for SBN0.4 and 0.5 that no $S \propto \frac{1}{T}$ dependence is present, but differentiating between a linear dependence and a logarithmic dependence of Seebeck coefficient requires a larger measurement temperature range than performed in this study. It is noted that the linear and logarithmic dependences both paint a similar picture in this case – an impurity band localized via Anderson localization. This is in agreement with the conductivity data and the model proposed via Figure 4-9.

As the Sr% increases from SBN0.4 to SBN0.7, differences in the Seebeck coefficients are observed at low temperatures, but the Seebeck coefficients converge at higher temperatures. The convergence point is near T_{Burns}. This suggests that when local polarization is zero, the samples all show similar behavior in Seebeck coefficients. The MMR Seebeck coefficient system unfortunately measures only to 600K, so a SBN0.6 sample was measured using the Ulvac-Riko ZEM-3 system at NASA Glenn Research Center. The measured values are plotted on top of data from the MMR system on Figure 4-10. The Seebeck coefficients of SBN0.6 at temperatures above T_{Burns} seem to be an extension of the behavior found in the normal ferroelectric SBN0.4 sample. This fits with the idea that the increase in $\frac{dE_a}{dT}$ at T_{Burns} is caused by disorder due to the relaxor ferroelectric polarization. Above T_{Burns} SBN0.6 has no polarization and therefore follows a similar trend to SBN0.4. Once SBN0.6 is cooled below T_{Burns}, the disorder from the polarization causes the mobility edge to move away from $E_{F.}$ This should decrease the band carrier concentration and result in an increase in the magnitude of the Seebeck coefficient. The trends are consistent within the series from SBN0.4 to SBN0.7. Normal ferroelectric SBN0.4 shows a linear/logarithmic temperature dependence of the Seebeck coefficient as the long-range order of the polarization plays little role, but as relaxor character is increased, the deviation from the linear/logarithmic trend becomes larger. The convergence of all samples near T_{Burns} and the reemergence of linear/logarithmic behavior at $T>T_{Burns}$ suggests that the relaxor-based polarization is strongly correlated to the phenomenon.

Although the proposed model fits most of the data, there are a few concerns to point out. First, although the expected logarithmic dependence of Seebeck coefficient is found at high temperatures, the derivation of this equation for a parabolic band results in a slope of $S\ vs\ ln(T)$ of -298 $\mu V/K^2$. The slope of the measured SBN0.4 sample is notably different: -170 ± 8 $\mu V/K^2$. This discrepancy could be due to any mechanism that makes the band non-parabolic, such as overlap between the impurity band and conduction band near E_f or due to the Hubbard band splitting of the impurity band. Another complication arises from possible changes to the structure or ferroelectric behavior due to the A-site filling discussed in Chapter 5. The presence of an NbO_2 second phase with no Ba or Sr-rich tertiary phases suggests that Ba and Sr are entering the naturally present metal vacancies on the A-site. The filling of the A-site may thus play an important role in octahedral bonding angles as well as the disorder of those angles. This would perturb d-orbital overlap and subsequently the conduction. These details require further examination, yet are not points which are inconsistent with the current model as a first order approximation. It is therefore proposed that conduction in SBN is via electronic states in an impurity band impurity band where the Fermi energy (E_F) lies within localized states in this band. The relaxor ferroelectric polarization in SBN seems to be a source of disorder. This affects the location of the mobility edge and therefore the activation energy of electrons into delocalized states, as shown via electronic conduction and Seebeck coefficient measurements. These results do not suggest ferroelectric polarization completely suppresses metallic conduction, but only that it can act as a source of disorder which may localize carriers.

4.4 Conclusions

Electrical conductivity and Seebeck coefficient measurements of SBN at different reduction conditions and different Sr/Ba ratios were used to study the conduction mechanism. Proposed here is a model where the E_F is surrounded by a finite number of localized electronic states that are separated from delocalized states via a mobility edge. This mechanism results in hopping conduction at low temperatures, consistent with the observed $T^{-1/4}$ behavior. At high temperatures the electrons activate from the impurity band over a mobility edge, consistent with the temperature-dependent activation energy. Changes to the electron transport properties were studied as samples were varied from normal ferroelectric to relaxor ferroelectric compositions. Changes in the activation energy for electronic conduction and the Seebeck coefficient suggest that the relaxor ferroelectric polarization acts as a source of disorder, thereby increasing the extent of Anderson localization.

Chapter 5

The Effects of Low Oxygen Partial Pressures on the Phase Equilibria and Cation Occupancy of Strontium Barium Niobate

Strontium barium niobate (SBN) is a tungsten bronze family ferroelectric which shows promising thermoelectric properties under heavily reducing conditions. It is found here that the enhanced electrical conductivity of oxygen deficient SBN correlates with the formation of a NbO_2 secondary phase. The effects of the reducing environment and the NbO_2 phase formation are studied via a detailed defect chemistry analysis. As harsher reduction treatments are used, the amount of the NbO_2 phase increases and is accompanied by an increase in the (Sr+Ba):Nb ratio of the SBN matrix. This is facilitated by an interesting mechanism where the A-site occupancy of the SBN matrix increases. The resulting donor defects cause the large carrier concentrations which are the source of the enhanced electrical conductivity necessary for thermoelectric performance. To better understand this A-site filling, the phase equilibria are examined in compositions with increased strontium and barium concentrations. It is found that a solid solution between $(Sr_{0.6},Ba_{0.4})Nb_2O_6$ and $(Sr_{0.6},Ba_{0.4})_{1.2}Nb_2O_6$ exists, and that A-site filling occurs at much more modest reduction conditions in Sr and Ba rich compositions. Finally, thermogravimetric analysis of the reoxidation process is performed, and the results suggest that the A-site filling is compensated ionically, possibly by the formation of oxygen interstitials. Not only do the presented results explain the enhanced electrical conductivity of oxygen deficient strontium barium niobate and point toward simplified processing routes for SBN thermoelectrics, but the modification of the site occupancies by reduction and reoxidation may widen the design space for property modification in tungsten bronze structured materials in general.

5.1 Introduction

Strontium Barium Niobate (SBN) is a ferroelectric material used in single crystal form for electro-optic and photorefractive non-linear optic applications[194, 195]; it has recently been identified as a potential thermoelectric in its oxygen deficient state[9, 32, 161]. SBN has a tetragonal tungsten bronze structure with space group *P4bm* at room temperature[120] and the unit cell shown in Figure 5-1.

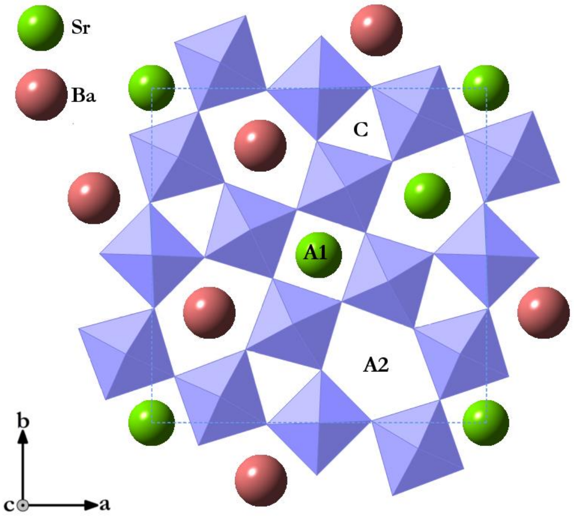

Figure 5-1. Tetragonal tungsten bronze crystal structure of strontium barium niobate. Corner-shared NbO_6 octahedra connect in-plane to form multiple cation sites labeled as A1, A2, and C-sites. 1/6th of the A1 and A2 sites are empty in stoichiometric $(Sr_x,Ba_{1-x})Nb_2O_6$.

The formula unit can be represented as $(A1)_4(A2)_2C_4B_{10}O_{30}$ where both the A1 and A2 sites host strontium ions, barium ions sit exclusively on the A1 site, the C-site is empty, and Nb fills the B-sites inside the oxygen octahedra. Only 5/6th of the A1 and A2 sites are filled, resulting in an A-site vacancy solid solution which is thought to contribute to the relaxor ferroelectric properties of SBN.[120, 121, 124, 196] Other tetragonal tungsten bronze materials show different cation site occupancies including, for example, in the ‘stuffed’ bronzes like

$K_6Li_4Nb_{10}O_{30}$ where all of the A1, A2 and C-sites are completely filled[197], and the ‘filled’ bronzes like $Ba_4Na_2Nb_{10}O_{30}$ where the A1 and A2 sites are filled but the C-sites remain empty.[198] These differences in cation occupancy can be important to functional properties. For example, cation site occupancy influences the ferroelectric properties of tungsten bronzes, although research is ongoing as to the mechanism [124, 199]. A recent survey of the field shows that the ordering of tilts may be a key parameter[199], and changes in cation occupancy may affect these tilts.

Additionally, oxygen deficient strontium barium niobate has been gaining interest as a potential thermoelectric material due to its low thermal conductivity and large thermoelectric power factor [9, 32, 142, 176–178, 200, 201]. Research has focused on both benchmarking the thermoelectric performance[9, 161, 176, 177] and understanding how the ferroelectric nature of SBN affects thermal conductivity[185, 201] and electron transport[32, 142, 191]. Multiple researchers have noted the formation of an NbO_2 secondary phase in reduced SBN [32, 178] and although the defect chemistry associated with oxygen loss in the SBN matrix is often considered[9, 178], other changes to the SBN matrix upon the formation of NbO_2 are not. As the electrical conductivity of NbO_2 is small compared to oxygen deficient SBN[172] it is unlikely this phase itself significantly enhances the thermoelectric performance. Despite this, samples with large electrical conductivities nearly always show the formation of a NbO_2 phase[142, 178].

Understanding correlations between enhanced thermoelectric properties, the presence of NbO_2, and changes to the SBN matrix may give insights toward optimization of the thermoelectric performance of SBN. Here the formation of the NbO_2 phase is studied as a function of annealing conditions with emphasis on changes to the A-site occupancy of the SBN matrix. The results show an increase of the A-site occupancy in SBN which explains the previously identified enhanced thermoelectric performance. The phase equilibria are then expanded into Sr/Ba-rich compositions. Finally, the ramifications of these findings on the oxidation resistance of SBN are discussed, and thermogravimetric analysis is used to study the reoxidation.

5.2 Experimental Procedure

Phase pure $(Sr_{0.6}Ba_{0.4})Nb_2O_6$ powders were fabricated via solid state reaction of $SrCO_3$, $BaCO_3$, and Nb_2O_5 powder precursors weighed out to the correct stoichiometric ratios and then heated to 1200°C for 6 hours. The high temperatures and long dwell times for calcination are required to eliminate Nb-rich and Ba-poor regions which lead to abnormal grain growth via the creation of a liquid phase at 1240°C[140]. After ball milling and drying of the reacted powder, pellets were uniaxially pressed at 15MPa, cold isostatically pressed at 200MPa, homogenized at 1200°C for 2 hours, and sintered at 1325°C for 6 hours to obtain >95% relative density[142]. Dense pellets were annealed at temperatures ranging from 950°C to 1300°C under oxygen partial pressures ranging from 10^{-9} to 10^{-19} atm. The phase compositions of samples were detected with powder X-ray diffraction (XRD) (PANalytical Empyrean).

An in-depth investigation was undertaken on a series of samples annealed at 1300°C and partial pressures of oxygen ranging from 10^{-9} to 10^{-16} atm. In these samples, changes in the chemistry of the SBN matrix were identified by using quantitative energy dispersive X-ray spectrometry (EDS) (FEI Quanta 200 Environmental SEM with an Oxford Instruments X-act $10mm^2$ silicon drift detector) to measure the (Sr+Ba):Nb ratio and Rietveld refinements were conducted to quantify the weight percentage of second phases in these samples. The refinements were conducted using PDF#04-0072133, #01-073-0487, and #04-002-9010 using JadeXRD analysis software. Samples for this investigation had compositions of $(Sr_{0.6}Ba_{0.4})Nb_2O_6$, $(Sr_{0.6}Ba_{0.4})_{1.1}Nb_2O_6$, and $(Sr_{0.6}Ba_{0.4})_{1.2}Nb_2O_6$ (SBN1.0, SBN1.1, and SBN1.2, respectively) and were fabricated using the same starting powders, calcining, and sintering conditions previously mentioned. Samples for EDS were polished down to 0.1µm diamond slurry and samples were measured under a background pressure of 30Pa to avoid charging of the sample surface. Electron beam intensity quantification was performed using copper foil and standardization of the EDS signal was performed using a phase pure oxygen deficient SBN1.0 pellet, which was annealed under 10^{-10} atm at 1300°C. Backscattered electron images were used to ensure that the EDS signal was only from the SBN matrix and to confirm the phase purity of XRD results.

Thermogravimetric analysis was performed on SBN1.0 samples which were annealed at 1300°C under 10^{-10} to 10^{-16} atm pO_2 using a TA Instruments TA2050. Samples were heated in flowing air up to 800°C at 10°C/min using ~100mg of powder. Sample pans were cleaned before each run by heating with an MAPP gas blowtorch.

Electrical conductivity tests were performed via a 4-pt probe measurement on rectangular samples of roughly 1.5 x 1.5 x 10 mm using a Keithley Integra 2700 multimeter. Sample leads were fabricated by sputtering platinum films through a shadow mask followed by attachment of silver wires by high-temperature silver epoxy. During measurement, samples were held under low oxygen partial pressure conditions to prevent reoxidation. Hall measurements on one SBN1.2 sample annealed at 10^{-16} atm were performed at 300.00 K using a Quantum Design® PPMS system. A Hall-bar geometry with Ga-In electrodes and silver wire leads were used. The Hall resistance was measured as a function of magnetic field from 80000 Oe to -80000 Oe while a current of 5 mA AC source and a vacuum of 5 mTorr were maintained. The misalignment voltage was subtracted via use of magnetic field reversal.

5.3 Results and Discussion

5.3.1 Formation of NbO_2 as a Function of pO_2 and Temperature

Previous studies have identified the presence of the NbO_2 phase in oxygen deficient SBN, but no studies have been conducted to precisely determine the annealing conditions necessary for NbO_2 formation. Therefore, the phase diagram of $(Sr_{0.6}Ba_{0.4})Nb_2O_{6-\delta}$ as a function of annealing temperature and oxygen partial pressure was investigated and is presented in Figure 5-2.

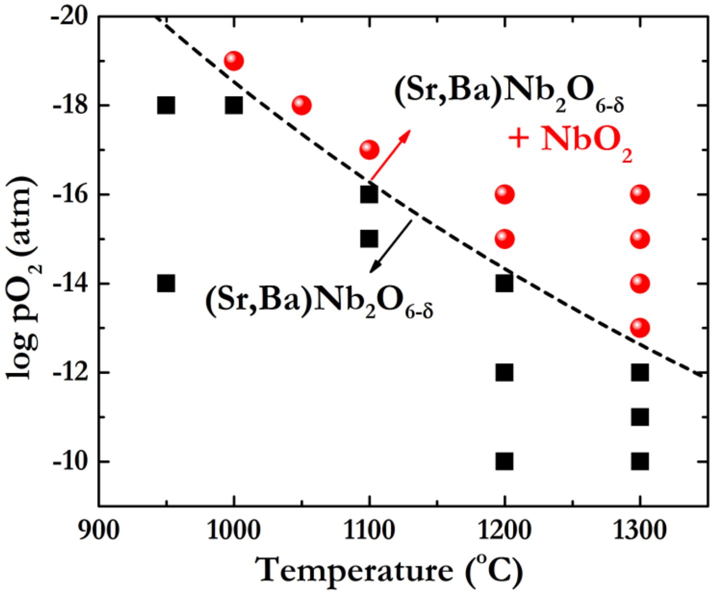

Figure 5-2. Phase diagram of SBN at various annealing temperatures and partial pressures of oxygen. Black squares are phase-pure SBN within XRD detection limits, red circles correspond to a detectable amount of NbO_2. The dotted line shows a constant oxygen vacancy concentration assuming an oxygen vacancy formation enthalpy of 4.25 eV.

The NbO_2 phase forms when SBN is annealed at high temperatures under low oxygen partial pressures. As the annealing temperature is increased, the critical oxygen partial pressure for NbO_2 formation increases. This suggests that NbO_2 forms once SBN reaches a critical oxygen vacancy concentration. If so, then the one and two phase regions should be separable by a line of constant oxygen vacancy concentration in the SBN phase. The pO_2-temperature conditions that control the thermodynamically stable concentration of oxygen vacancies can be calculated using the law of mass action assuming the defect reaction:

$$O_o^x \leftrightarrow V_o^{\cdot\cdot} + 2e^- + \frac{1}{2} O_{2(g)} \tag{5.59}$$

with an equilibrium constant of

$$K_{eq} = \frac{[V_o^{\cdot\cdot}] n^2 {pO_2}^{1/2}}{[O_o^x]} \tag{5.60}$$

where $[V_o^{\cdot\cdot}]$ is the oxygen vacancy concentration per oxygen lattice site, n is the electron concentration, $[O_o^x]$ is the concentration of oxygens per oxygen lattice site, and pO_2 is the partial pressure of oxygen used as a measure of the oxygen activity. When the following Brouwer approximation can be employed:

$$n \cong 2[V_o^{\cdot\cdot}] \tag{5.61}$$

the pO_2-temperature conditions are:

$$\ln(pO_2) = \frac{2\Delta H}{RT} + \frac{2S_{conf}}{R} + 2ln\left(\frac{[O_o^x]}{4[V_o^{\cdot\cdot}]^3}\right) \tag{5.62}$$

where: ΔH is the enthalpy of formation for an oxygen vacancy and S_{conf} is the configurational entropy. The vibrational entropy is assumed to be negligible as a first order approximation. A line that separates the one and two phase regions is obtained with a ΔH of 4.25 eV and $[V_o^{\cdot\cdot}]$ of 0.002. These values are compatible with previous studies in SBN[202] and the TGA data in Figure 5-7, discussed later. This condition is plotted as a dotted line in Figure 5-2. The good agreement between Equation (5.4) and the onset of NbO_2 formation suggests that the formation of NbO_2 is likely a result of the SBN reaching the solid solubility limit for oxygen vacancies. The result is that under low partial pressures of oxygen SBN leaves the solid solubility regime and enters a two-phase region resulting in the formation of NbO_2.

5.3.2 Change in A-site Occupancy of the SBN Matrix During NbO_2 Formation

Although a likely mechanism which determines the onset of NbO_2 formation has been identified, the mechanism by which enhanced thermoelectric properties occur must be established. Toward this goal, the changes to the chemistry of samples were studied. To understand the effect of NbO_2, it is important to note that the NbO_2 is the only secondary phase. That is, samples above the critical oxygen vacancy concentration threshold are mixtures of SBN and NbO_2 with no strontium-rich or barium-rich tertiary phases, as confirmed by XRD (e.g. Figure 5-3) and scanning electron microscopy (SEM). The conservation of mass dictates that the total amounts of Sr, Ba, and Nb in the system must be kept constant before and after NbO_2 formation. There are two possible ways for this to occur without a Sr/Ba-rich tertiary phase. First, the excess Sr and Ba may either remain as defects in the SBN (and/or NbO_2) matrix or, secondly, the excess Sr and Ba may evaporate into the atmosphere as volatile species. The second possibility was eliminated by the following experiment: SBN+NbO_2 composites made by annealing at 1300°C under a pO_2 of 10^{-16} atm were re-annealed in air at 1300°C for 6 hours. The XRD pattern after the air anneal shows only a phase-pure SBN (Figure 5-3) confirming the reversibility of the reaction. Similar results were verified for multiple SBN+NbO_2 composites. If extensive cation volatility occurred, then the Sr and Ba would not be present to reform phase pure SBN. Extensive cation volatility is therefore ruled out, and the accommodation of the excess Sr and Ba is likely dominated by internal changes of the composition. A finite solubility of Nb (perhaps as Nb^{2+}) on the A site is also possible. Clearly, however, this mechanism does not dominate the response, given the observation of NbO_2 second phase particles.

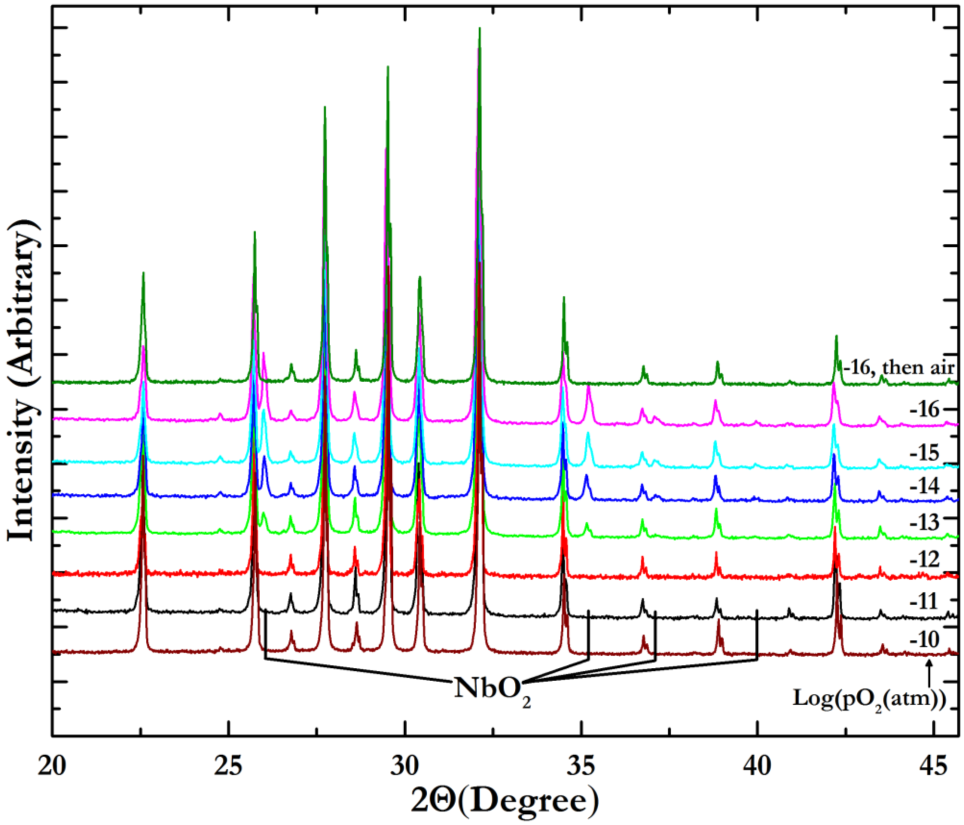

Figure 5-3. Offset XRD patterns of $(Sr_{0.6},Ba_{0.4})Nb_2O_{6-\delta}$ annealed at 1300°C under multiple partial pressures of oxygen. An NbO_2 phase forms starting at 10^{-13} atm pO_2 and increases in volume fraction for decreasing pO_2. The NbO_2-containing sample annealed at 10^{-16} atm pO_2 was reannealed in air at 1300°C for 30 hours, and shows only phase pure SBN.

To investigate the changes in composition of the SBN matrix, quantitative EDS spectra were measured on the SBN matrix of SBN+NbO_2 composites formed at 1300°C under multiple pO_2 conditions. Due to charging under the electron beam, an unreduced insulating sample could not be used as a compositional standard. Quantification was instead achieved by presuming a phase pure SBN sample annealed at 1300°C under 10^{-10} atm pO_2 to have a (Sr+Ba):Nb ratio of 0.5. The (Sr+Ba):Nb ratio of 0.5 was found to be maintained in phase pure samples annealed at pO_2 values of 10^{-11} and 10^{-12} atm. As the partial pressure of oxygen during annealing is lowered, the (Sr+Ba):Nb ratio increases toward a value of 0.593±0.015 (Figure 5-4(a)).

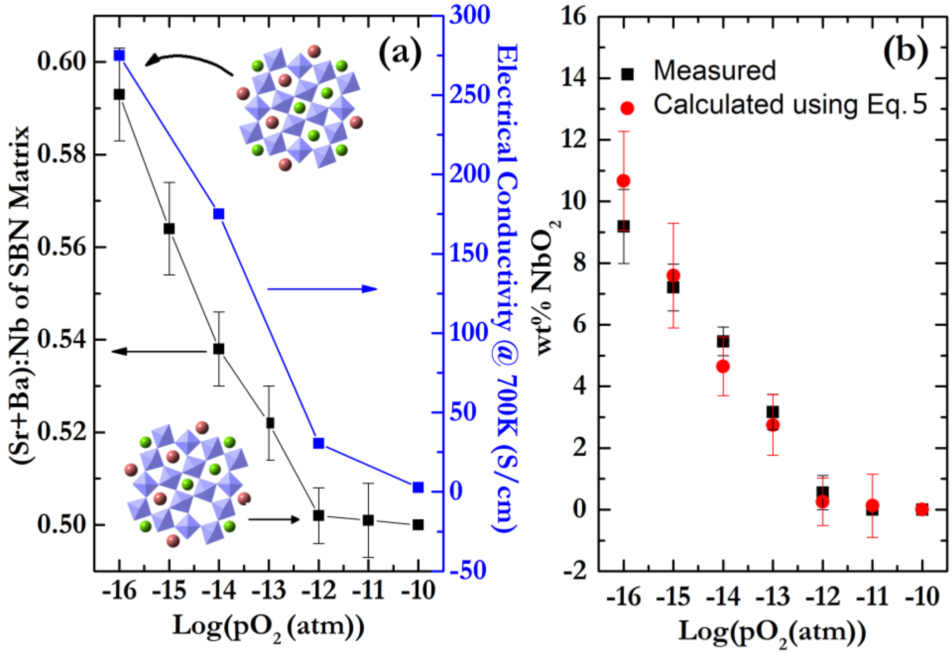

Figure 5-4. (a) The (Sr+Ba):Nb ratio in the SBN matrix of SBN+NbO_2 composites increases alongside the electrical conductivity. (b) Equation (5.5) correctly calculates the amount of NbO_2 formed by using the (Sr+Ba):Nb ratio of the SBN matrix.

The onset of NbO_2 formation occurs at 10^{-13} atm, the same sample in which the (Sr+Ba):Nb ratio first increases above 0.5. Both the (Sr+Ba):Nb ratio and the Wt.% of NbO_2 increase linearly as the partial pressure of oxygen decreases logarithmically below 10^{-12} atm pO_2 (Figure 5-3 and 5-4b). It therefore seems that the (Sr+Ba):Nb ratio and the NbO_2 phase formation are linked.

The link between NbO_2 concentration and the (Sr+Ba):Nb ratio could, in principle, be explained either by an increase in Nb vacancies or via an increase in the Sr and Ba concentration of the SBN matrix. The possibility of Nb vacancies can be ruled out based on the observation that the electrical conductivity rises as the (Sr+Ba):Nb ratio increases. As SBN is an n-type conductor[142], acceptor defects such as Nb vacancies (which would promote p-type conductivity) are therefore unlikely. Thus, the exsolution of SBN into an SBN+NbO_2 composite must be accommodated by an increase in the Sr and Ba content in the SBN matrix. An increased A-site occupancy is a likely mechanism for this to occur.

In air-fired $(Sr_x,Ba_{1-x})Nb_2O_6$ only 5 of the 6 A1 and A2 sites (where Sr and Ba occupy) are filled, making SBN a vacancy solid solution with an A-site occupancy of 0.83. It is likely that the increase of the (Sr+Ba):Nb ratio is a result of the filling of these vacancies toward a limiting A-site occupancy of 1 and an end-member composition of $(Sr_xBa_{1-x})_{1.2}Nb_2O_6$. The formation of NbO_2 would therefore be a consequence of this process. As phase equilibria investigations of Sr-Ba-Nb-O systems show a finite solubility of excess Nb in SBN [203, 204], one contingency is that some of the excess Nb may remain in solution in the SBN matrix. The NbO_2 would therefore only form once the solubility limit for excess Nb in SBN is reached. The defect chemistry associated with the Nb excess is uncertain, but possibilities include Nb sitting on the A-site similar to materials such as $Nb_{16}W_{18}O_{94}$[205, 206] or possibly NbO-layer intergrowths as are found in multiple reduced niobates [207–209]. In the absence of any Nb excess in solution, the reaction for NbO_2 formation from an increasing A-site occupancy would be:

$$\begin{gathered}(1+y)(Sr_xBa_{1-x})Nb_2O_6 \rightarrow \\ (Sr_xBa_{1-x})_{1+y}Nb_2O_6 + 2yNbO_2 + yO_{2(g)}\end{gathered} \tag{5.63}$$

If Equation (5.5) is accurate, the Wt.% of NbO_2 in the final composite could be calculated once y is known; the value of y can be obtained using the (Sr+Ba):Nb ratio of the SBN matrix measured via EDS:

$$\frac{(Sr+Ba)}{Nb} = \frac{(1+y)}{2} \tag{5.6}$$

This calculated Wt.% of NbO_2 is compared to the values measured via Rietveld refinements in Figure 5-4b and shows good agreement. This suggests that Equation (5.5) is appropriate, meaning that the NbO_2 formation is a response of the increased A-site occupancy and that Nb solubility is negligible, within the error of the current measurements. Additionally, a sample annealed under 5% H_2/Ar forming gas at 1400°C was found to have an $SrNb_8O_{14}$-structured tertiary phase and an SBN matrix with a (Sr+Ba):Nb ratio of 0.597±0.005. This agrees with a prediction of the A-site filling hypothesis that the maximum (Sr+Ba):Nb ratio should be 0.6, corresponding to an A-site occupancy of 1 with no excess Nb. After an A-site occupancy of 1 is reached, any additional decrease in the oxygen activity is accommodated by an additional phase. More accurate determination of the site occupancies could be achieved via Rietveld refinements as has been done previously for air-fired SBN[120, 121, 196], but unlike previous studies the A-site vacancy concentration must be refined in the current work. This additional degree of freedom renders refinements of the system unconstrained if only XRD and compositional analysis are used. Analysis of site-occupancies using simultaneous refinement of x-ray and neutron diffraction data constrained via precise compositional analysis of the SBN matrix is an interesting avenue for future work.

From the perspective of oxygen deficient SBN as a thermoelectric, the above finding suggests that engineering the carrier concentration for maximum thermoelectric performance is not a function of the concentration of oxygen vacancies only. The increased A-site occupancy can be treated as the filling of neutral A-site vacancies with 2+ cations or, in Kröger-Vink notation, $A_{V_A^x}^{\cdot\cdot}$. These defects must be taken into account when engineering the carrier concentration. For a filled SBN sample the expected carrier concentration, *n*, can be calculated using the number of defects per unit cell, 6y, and the volume of the unit cell from the lattice parameters. For y=0.2, the completely filled condition, and a unit cell volume of 615$Å^3$ the carrier concentration is calculated to be $4*10^{21}$/cc. Such high carrier concentrations are near the degenerate regime, consistent with proposed impurity band models for electron transport in oxygen deficient SBN.[142] Although previous studies assumed oxygen vacancies to be the major donor defect [9, 32], the difference of electrical conductivity before and after A-site filling starts to occur (2.8 S/cm in 10^{-10} atm samples compared to 275 S/cm in 10^{-16} atm samples, Figure 5-4a) suggests that the oxygen vacancies play a minor role. The low partial pressures of oxygen during annealing seem to play the major role not by modifying the concentration of oxygen vacancies, but instead by moving the equilibrium into a phase region where A-site filling is favorable. It therefore seems that the correlation between the NbO_2 phase and enhanced thermoelectric properties occurs because the presence of NbO_2 is a marker for the onset of A-site filling. In this model the NbO_2 is an unnecessary phase. Formulating compositions with various A-site occupancies without excess Nb may result in phase pure samples with similarly enhanced thermoelectric properties

5.3.3 Phase Equilibrium of $(Sr_{0.6},Ba_{0.4})_{1+y}Nb_2O_{6-\delta}$ at Low Oxygen Activities

To clarify the process of making phase pure A-site filled samples, the phase equilibria of $(Sr,Ba)_{1+y}Nb_2O_{6-\delta}$ under low oxygen partial pressures is investigated. Two additional powders were batched with compositions equivalent to $(Sr_{0.6},Ba_{0.4})_{1.1}Nb_2O_6$ and $(Sr_{0.6},Ba_{0.4})_{1.2}Nb_2O_6$, or SBN1.1 and SBN1.2, respectively. Air-fired pellets of SBN1.1 and SBN1.2 were found to be mixtures of SBN and $(Sr_x,Ba_{1-x})_2Nb_2O_7$. The $(Sr_{1-x},Ba_x)_2Nb_2O_7$ in these pellets all were measured to be $x\approx0.17$ via EDS, well within the solid solubility limits for $(Sr_{1-x},Ba_x)_2Nb_2O_7$ of $0<x<0.35$.[210] For simplicity the notation "***A***" will be used to refer to cations that are either Sr^{2+} or Ba^{2+}. These air-fired pellets were annealed at 1300°C for 30 hours at pO_2 values ranging from 10^{-9} to 10^{-16} atm, and the phase compositions were measured via XRD and Rietveld refinements.

The results are presented in Figure 5-5.

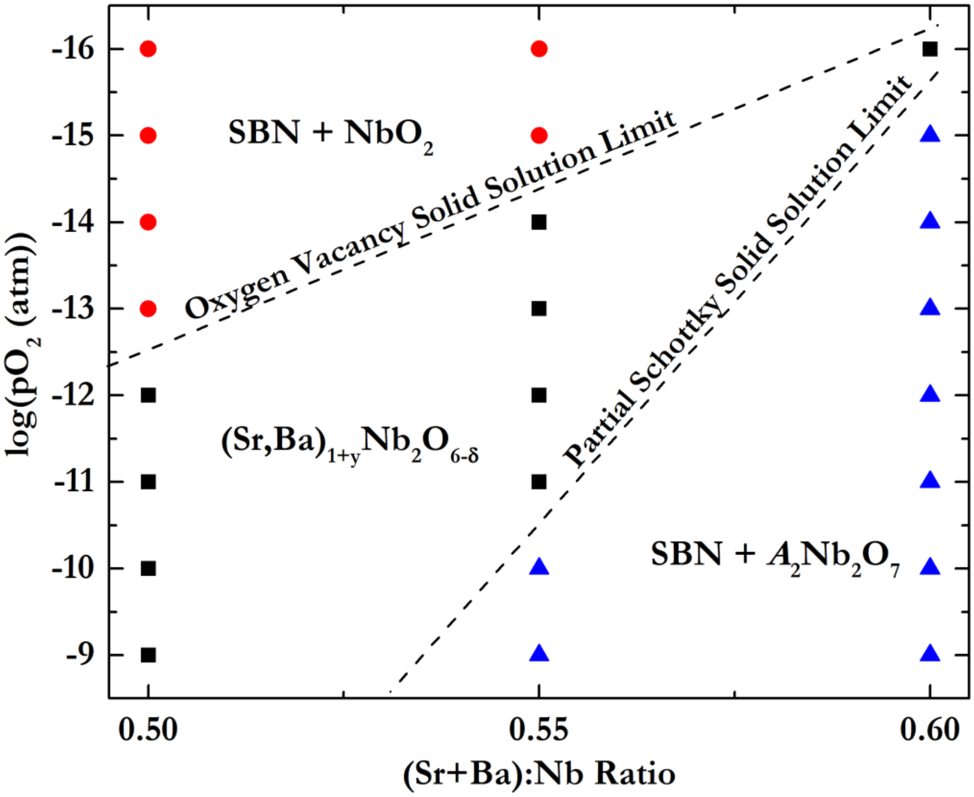

Figure 5-5. Phase composition of different SBN samples batched with different A:B ratios and annealed at 1300°C under various pO_2 conditions. Moving to the right on the plot corresponds to an increase in the Sr and Ba chemical potentials. Note that decreasing pO_2 is plotted along the positive y direction. Samples with NbO_2 as a secondary phase are marked with red circles, phase pure samples are black squares, and samples with $A_2Nb_2O_7$ are blue triangles. The SBN phase region is limited by the solid solution limits of either oxygen vacancies or partial Schottky defects.

Three regions are found, one with only phase pure SBN, one which shows the NbO_2 secondary phase, and another which shows an $A_2Nb_2O_7$ secondary phase. The dotted line which separates the phase pure and SBN+$A_2Nb_2O_7$ region extends down to SBN1.0 in air. Given the results shown in Figure 5-2, the boundary between the phase pure SBN and SBN+NbO_2 regions is thought to be the solid solution limit for oxygen vacancies. The dotted line from Figure 5-2 would therefore be the extension of this boundary into the temperature axis. From Gibbs' phase rule for this 4 component system, the number of degrees of freedom in the single phase solid solution regime is 5. The volumetric phase field in the quaternary diagram allows for independent changes in temperature, pO_2, and the other three individual component chemical potentials. Once the solid solution limit of any component is reached, the system loses one degree of freedom and the chemical potentials can no longer be changed independently. This results in the two-phase regions in Figure 5-5. For the SBN+NbO_2 phase region, both the amount of NbO_2 which forms and the composition of the SBN matrix would then be determined by the tie-line between this phase boundary and the NbO_2 phase field on the Sr-Ba-Nb-O quaternary molar phase diagram. Similarly, the lower dotted line is thought to be the solid solution limit for partial Schottky defects; the phase composition would be determined by the tie line between this limit and the $A_2Nb_2O_7$ phase field boundary.

When the SBN phase is in equilibrium with a secondary phase, the chemical potentials of the different components are equal in both phases. This can be used to predict how the boundaries between the one and two phase regions react to changes in the component chemical potentials. For SBN-NbO_2 composites this equilibrium results in:

$$2NbO_2 + \frac{1}{2}O_2 + A_{V_A^x}^{\cdot\cdot} \leftrightarrow 2Nb_{Nb}^x + A_A^x + 5O_o^x + V_o^{\cdot\cdot} \qquad (5.7)$$

This means, in terms of chemical potentials, that at the SBN-NbO_2 equilibrium:

$$\frac{1}{2}\mu(O_2) + \mu\left(A_{V_A^x}^{\cdot\cdot}\right) = const. + \mu(V_o^{\cdot\cdot}) \qquad (5.8)$$

As the oxygen vacancy solid solution limit has been reached, a decrease in the pO_2 cannot be accompanied with an increase in the $\mu(V_o^{\cdot\cdot})$. Hence, the result is an increased chemical potential for $A_{V_A^x}^{\cdot\cdot}$. The increased chemical potential of Sr and Ba in SBN1.1 and 1.2 increases the $\mu\left(A_{V_A^x}^{\cdot\cdot}\right)$ and therefore decreases the $\mu(O_2)$, explaining the positive slope of the upper phase boundary in Figure 5-5.

For SBN- $A_2\mathrm{Nb_2O_7}$ composites at equilibrium:

$$A_2Nb_2O_7 \leftrightarrow 2Nb_{Nb}^{x} + A_A^{x} + 6O_o^{x} + \frac{1}{2}O_2 + A^{\cdot\cdot}_{V_A^{x}} \tag{5.9}$$

and

$$const. = \frac{1}{2}\mu(O_2) + \ \mu(A^{\cdot\cdot}_{V_A^{x}}) \tag{5.10}$$

Therefore, decreasing the oxygen partial pressure results in an increase in $\mu\left(A^{\cdot\cdot}_{V_A^{x}}\right)$ as confirmed by the positive slope of the lower phase boundary in Figure 5-5. In both scenarios an increase in the total (Sr+Ba):Nb ratio lowers the necessary oxygen activity for A-site filling.

The phase compositions of the samples are shown in Figure 5-6 alongside the (Sr+Ba):Nb ratio of the SBN matrix measured via EDS. The amount of $A_2\mathrm{Nb_2O_7}$ phase present in SBN1.1 and 1.2 is decreased compared to that of air-fired samples. This is corroborated by EDS data which shows the SBN matrix in SBN1.1 and 1.2 pellets possess a (Sr+Ba):Nb ratio above 0.5 for all samples. Therefore, SBN1.1 and 1.2 have increased A-site occupancy even at 10^{-9} atm $\mathrm{pO_2}$. This stands in stark contrast to SBN1.0, where changes to the A-site occupancy do not occur until 10^{-13} atm $\mathrm{pO_2}$. It does, however, agree with the predicted equilibrium between SBN and $A_2\mathrm{Nb_2O_7}$ outlined in Equation (5.10). Within the phase purity region of SBN1.1, the (Sr+Ba):Nb ratio of the SBN matrix remains constant near the expected value of 0.55. Changes in oxygen activity within these samples are accommodated by changes in the oxygen vacancy and quasi-free electron concentrations according to Equation (5.2). This increased A-site filling in samples with increased strontium and barium contents point toward easier processing routes for thermoelectric SBN, as higher oxygen partial pressures may be used during annealing. The electron transport properties of these phase-pure filled SBN ceramics are similar to those of $SBN+NbO_2$ composites.[211]

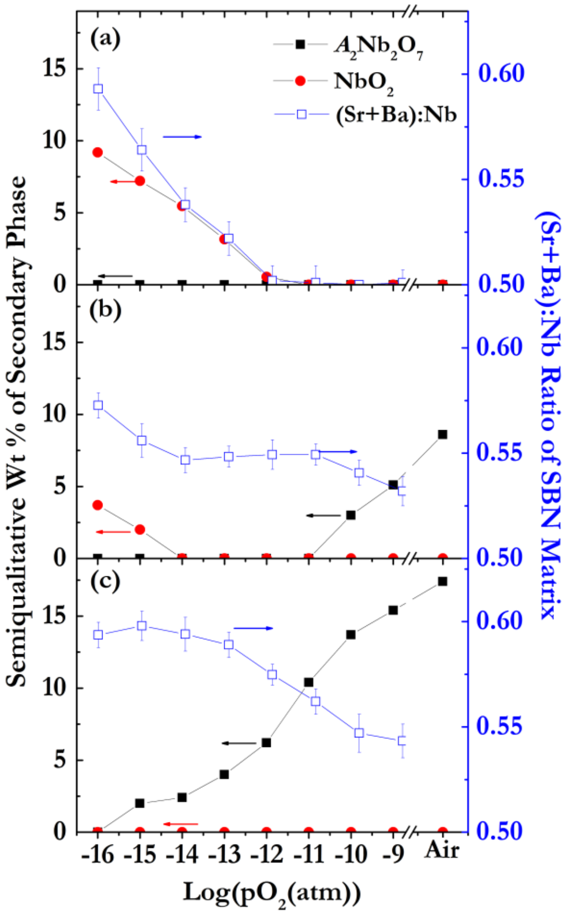

Figure 5-6. Phase composition of SBN samples batched with a (Sr+Ba):Nb ratio of (a) 0.50 (b) 0.55 and (c) 0.60 annealed at 1300°C at varying pO_2 conditions. The amount of $A_2Nb_2O_7$ drops below that of air-fired samples at pO_2 values as low as 10^{-9} atm, showing that A-site filling is occurring at higher pO_2 values in samples with increased (Sr+Ba):Nb ratios.

5.3.4 Reoxidation of $(Sr_{0.6},Ba_{0.4})_{1+y}Nb_2O_{6-\delta}$

From a device standpoint, the equilibrium conditions are important for processing, but more important is the stability of SBN under working conditions. Although filled SBN shows promise as a thermoelectric, the lack of oxidation resistance is a major hurdle which needs to be solved. The only quantitative numbers currently published show oxidation at temperatures as low as 700°C[202], but changes in properties start to occur at much lower temperatures. It is widely mentioned in experimental procedures that high temperature measurements of SBN are performed under inert atmospheres[142, 176, 212], and polycrystalline SBN samples measured in 0.1 atm He above 480°C were reported to show degradation of the electrical properties[142].

Given the current results on A-site filling, the sensitivity of the electrical properties of SBN to oxygen environments is peculiar. As discussed previously, a vast majority of the carrier concentration is thought to occur due to the A-site donors rather than the compensation of oxygen vacancies. While the oxygen vacancies may be filled via annealing in air, then the A-site donors remain, and therefore require a negative compensating defects such as electrons. However, oxygen deficient SBN annealed under 10^{-16} atm was annealed in air at 700°C for 3 hours and resulted in a white powder of SBN and γ-Nb_2O_5. The white color of the powder points toward a lack of electronic carriers, suggesting the A-site donors must be ionically compensated. The defect chemistry for the ionic compensation scenario is puzzling, as the possible compensating defects are either cation vacancies or some form of superoxidation. Both of these are unlikely. Under the equilibrium condition in air the A-site donors would either react with NbO_2 to form SBN (for SBN1.0) or form an $A_2Nb_2O_7$ phase (for higher Sr and Ba concentrations). However, for the kinetically constrained condition of annealing at 700°C it is unlikely that cations could migrate long distances. If the required 10^{21}/cc cation vacancies did form, then the aforementioned secondary phases would be detectable via SEM or XRD (either as a crystalline phase or an amorphous hump), and no evidence of such a secondary phase is found. Therefore migration of the A-site donors out of the lattice is unlikely.

The sluggish cation motion means that compensation occurs via the anion lattice. However, the formation of oxygen interstitials is unlikely due to their large size. The largest empty site in A-site filled SBN is the C-site. Outside of the fact that an oxygen interstitial on this site would be unfavorably surrounded by anions, the only ion which has been found to fit on the C-site is Li^{+} [197], which has a 6-coordination Shannon-Prewitt radius of 0.74 Å, much smaller than the radius of 1.40Å for an oxygen anion in 6-coordination. Due to this, it is unclear where the additional oxygen absorption is located or the mechanism by which it occurs, but the compensation of the A-site donors is peculiar and the identification and study of any possible oxygen absorption via TGA is worthwhile.

The results from TGA are presented in Figure 5-7.

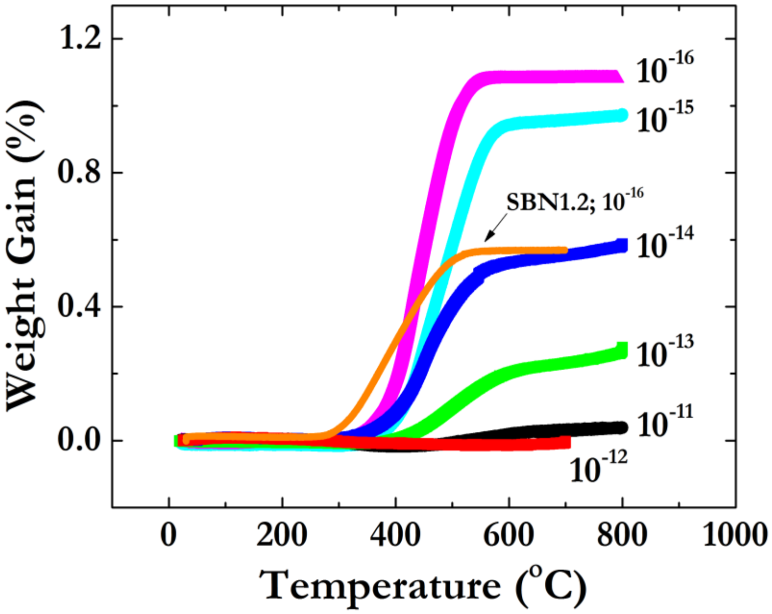

Figure 5-7. Thermogravimetric analysis in air of various $(Sr_{0.6},Ba_{0.4})\ Nb_2O_6$ powders annealed at 1300°C for different partial pressures of oxygen (in atm). The weight gain is a combination of an NbO_2 to Nb_2O_5 transition and the changing oxygen content of the matrix. The weight gain increases with decreasing partial pressure of oxygen during annealing.

A measurable weight gain is present and clearly increases for samples which are annealed under lower oxygen activities. Care must be taken in analysis of the TGA data as it is a result of two contributions. One contribution is from the NbO_2 to Nb_2O_5 transition and the other from absorption of oxygen by the SBN matrix. However, these may be deconvoluted to a degree. This is because the amount of NbO_2 in the samples is known from the Rietveld refinements discussed previously. Unfortunately, a combination of errors from both the Wt.% of NbO_2 from Rietveld refinements and the baseline drift in the TGA signal prevents precise deconvolution of the two contributions, but rough estimates are possible. The calculated weight gain from the NbO_2 to Nb_2O_5 transition is $128\frac{mg}{gNbO_2}$, giving an expected weight gain of 0.6±0.1% for SBN1.0 annealed under 10^{-16} atm pO_2. This accounts for only roughly half of the measured weight gained. The remainder must be due to absorption of oxygen by the SBN matrix.

The oxygen absorption by the SBN matrix could be from either filling of oxygen vacancies and/or superoxidation. The samples annealed under 10^{-11} and 10^{-12} atm pO_2, samples with neither A-site filling nor NbO_2, show no measureable weight gain discernable from the baseline drift of the TGA. The 10^{-12} atm sample is near the solid solubility limit for oxygen vacancies, and therefore its weight gain should estimate the maximum weight gain from oxygen vacancies possible in any sample. As this weight gain is <0.1% (i.e., lower than TGA can measure), it is thought that the contribution to the weight gain from the filling of oxygen vacancies is minimal. The additional absorption of oxygen in the SBN lattice must therefore be due to some form of superoxidation. The location of the excess oxygen is unknown, but for simplicity an absorbed oxygen with a 2^- charge will be denoted as an oxygen interstitial, $[O_i'']$.

The electroneutrality equation for SBN during low temperature reoxidation is then:

$$2\left[A_{V_A^x}^{\cdot\cdot}\right] + 2[V_O^{\cdot\cdot}] = n + 2[O_i''] \tag{5.64}$$

Under the fully oxidized condition, $[V_O^{\cdot\cdot}]$ is negligible and samples are insulating and white, suggesting n is negligible as well. Therefore, for oxidized samples we may write:

$$2\left[A_{V_A^x}^{\cdot\cdot}\right] \cong 2[O_i''] \tag{5.65}$$

Thus, under these conditions the weight gain of the SBN matrix during reoxidation is entirely due to the superoxidation, $[O_i'']$. As the amount of superoxidation can be determined via the weight gain measured via TGA, the $\left[A_{V_A^x}^{\cdot\cdot}\right]$ can be determined via equation (5.12). For the TGA data in Figure 5-7 the concentrations lay in the range of ~10^{21}/cc. This result can be used to measure the carrier concentration of oxygen deficient samples, because in oxygen deficient samples it can be assumed $[O_i'']$=0 and $\left[A_{V_A^x}^{\cdot\cdot}\right] \gg [V_O^{\cdot\cdot}]$ resulting in Equation (5.11) simplifying to:

$$2\left[A_{V_A^x}^{\cdot\cdot}\right] \cong n \tag{5.66}$$

Precise determination of *n* is hindered by the previously mentioned errors from TGA and Rietveld associated with the NbO_2 phase. A more accurate determination of *n* is possible if the same analysis is performed on a phase-pure SBN1.2 sample annealed at 1300°C under forming gas. The value of *n* in this sample was determined by two methods. The first method assumed that the weight gain during TGA was due to superoxidation; n was then calculated using Equations (5.12) and (5.13). Secondly, carrier concentrations were determined on reduced samples by Hall measurements. The TGA data for the SBN1.2 sample is presented alongside the TGA data for SBN1.0 in Figure 5-7. The value of *n* calculated from TGA was found to be $(2.6\pm0.3)*10^{21}$/cc. Hall measurements on this sample before reoxidation were performed by Chan et al.[211], and gave a value for *n* of $(2.3\pm0.3)*10^{21}$/cc. The equivalence of these numbers suggests that the analysis of Equations (5.11-13) is correct. From these results it seems that the lack of oxidation resistance is not due to the filling of oxygen vacancies, but instead to the absorption of additional oxygen. Additional research is necessary to identify the specific location of this oxygen in the lattice, which should be possible via combinations of refinements of X-ray diffraction and Neutron diffraction profiles. Knowledge of the oxygen interstitial position could help in identifying a strategy for increasing the oxidation resistance of SBN thermoelectrics. As a final point, the lack of an NbO_2 phase in the SBN1.2 sample meant that the sample did not powderize due to the NbO_2 to Nb_2O_5 transition upon reoxidation. The dielectric properties of reoxidized ceramic samples were therefore measureable and were found to have a lower magnitude of the maximum permittivity and a decreased temperature of maximum permittivity as is discussed elsewhere.[211] Effects of the increased A-site occupancy and superoxidation on the structure-property relations of tetragonal tungsten bronze dielectrics is an interesting avenue for future work.

5.4 Conclusions

Formation of NbO_2 occurs in oxygen deficient SBN at high temperatures and low partial pressures of oxygen once a critical oxygen vacancy concentration is reached. As the oxygen activity decreases at a constant temperature, the amount of NbO_2 increases and is accompanied by an increase in the (Sr+Ba):Nb ratio of the SBN matrix. It is shown that the defect mechanism for this change is the filling of the naturally occurring A-site vacancies in SBN, a mechanism which results in donor defects. Using the chemical potential equivalence of cations between the matrix and secondary phase, it is shown that increasing the (Sr+Ba):Nb in the starting batch results in an increased chemical potential for A-site stuffing and affects the critical oxygen activity for second phase formation. This provides an interesting route toward control of the carrier concentration in thermoelectric SBN via the A-site filling. The lack of oxidation resistance of SBN under this model is due to compensation of $A^{\cdot\cdot}_{V_A^x}$ by some form of superoxidation. All in all, the current results show an interesting crystal-chemical modification of SBN due to processing in low partial pressures of oxygen. The tungsten bronze structure possesses a large number of degrees of freedom which allows for property design, and this new processing route widens the design space. This helps not only to increase the utility of oxygen deficient SBN as a thermoelectric, but should also be a useful tool in building a set of structure-property relations of tungsten bronzed structured materials

Chapter 6

Thermoelectric Properties of (Sr,Ba)Nb2$O_{6-\delta}$ Single Crystals: zT's and Anisotropy

In this chapter, the thermoelectric properties of SBN single crystals are revisited under an expanded range of measurement temperatures and annealing conditions. The power factor of the SBN single crystals measured here are lower than previously reported, 4.2µW/cmK^2 rather than 19µW/cmK^2 at 250°C for the 10^{-14} atm pO_2 annealing condition. Presuming polycrystalline values of the thermal conductivity, zT values of 0.38 at 600°C are obtained. The formation of the NbO_2 secondary phase upon reduction is studied, and is found to deviate from that of the polycrystalline samples of chapter 5 due to the lack of heterogeneous nucleation sites. The Seebeck coefficient along the polar axis of the crystals shows similar behavior to relaxor ferroelectric samples, while the nonpolar axis shows behavior similar to the normal ferroelectric/paraelectric samples, providing evidence that the ferroelectricity is perturbing the electron transport.

6.1 Introduction

Strontium Barium Niobate has been reported to have thermoelectric power factors as large as 19µW/cmK^2 along the *c*-axis of oxygen deficient single crystals. [9] These power factors are similar in magnitude to other potential oxide thermoelectrics[6, 110, 112, 114, 117], but SBN possesses the added advantage of a low thermal conductivity, <2 W/mK[10]. The reported power factors in conjunction with steady state thermal conductivity measurements resulted in a zT value of 0.75 at 250°C [32]. The power factors were shown to increase as a function of temperature and annealing pO_2, suggesting additional increases in zT are possible [9] .

The largest zT values reported for polycrystalline samples of SBN are ~0.2 at 830°C[185] compared to ~ 0.75 at 250°C for single crystals. A decreased zT in polycrystalline samples is expected as power factors along the *c*-axis were reported to be over ten times larger than the *a*-axis.[9] By multiplying the numerical averages of the reported thermoelectric property tensor components, a power factor value of 5μW/cmK^2 at 250°C is expected for polycrystalline samples; however, no values >2.2μW/cmK^2 at 250°C have been reported[176, 212–214] While texturing increases the power factor [161], the improvement was minor and an anisotropy of only $\frac{PF_c}{PF_a} \sim 1.8$ was found at a Lotgering factor of 82-90%. Given this, a reexamination of the thermoelectric properties of single crystal SBN was deemed to be of interest.

One possible difference between single crystals and ceramics may be in the formation of NbO_2 during annealing. In chapter 5 it was shown that the NbO_2 phase formation is concurrent with an increase in the Sr/Ba-site occupancy under low oxygen activity conditions. The increased A-site occupancy is thought to act as a donor source, thereby causing the large carrier concentrations found in oxygen deficient SBN. The appearance of NbO_2 therefore acts as an important marker for enhanced thermoelectric properties. In polycrystalline materials, NbO_2 nucleates heterogeneously at the grain boundaries; therefore the lack of grain boundaries in single crystals may hinder NbO_2 formation. As previous reports of SBN single crystals did not investigate NbO_2 development, a study of NbO_2 in single crystals is conducted here.

The thermoelectric properties of single crystals over an extended range of temperature and annealing conditions are reported. Values in line with reported polycrystalline data are found, suggesting that previous reports are single crystals were anomalous. It was found that the NbO_2 formation conditions in single crystals differ from those of polycrystalline samples, but adjusting for this difference via seeding NbO_2 particles using a pre-anneal shows that this is not the cause for the anomalous power factors of previous crystals. The anisotropy of the properties is discussed, as is the role of ferroelectricity.

6.2 Experimental Procedure

Single crystals of strontium barium niobate were obtained from Altechna Co. (Vilnius, Lithuania). Substrates of 10x10x1mm were aligned and cut into samples of 10x1x1mm in length using a ADT ProVectus 7100 dicing saw. The single crystals were reduced using thermal anneals in atmospheres with low partial pressures of oxygen. Anneals were completed in an alumina tube furnace with temperatures measured via a sheathed thermocouple sitting directly next to the sample. Annealing temperatures and times were kept constant at 1300°C and 30 hours. The annealing atmosphere was varied to 10^{-11}, 10^{-14}, 10^{-15}, and 10^{-16} atm pO_2. Control of the pO_2 was achieved using gas mixtures of H_2 and $H_2O(g)$. $H_2O(g)$ was delivered via argon flowed through a bubbler, and additional argon was used as a carrier gas.

Seebeck coefficients and electrical conductivities were measured on a Linseis LSR-3/800 Seebeck coefficient and electrical resistivity unit. Data were taken using the steady state differential technique. [215] Measured temperature gradients were spaced ~1-2°C apart and were limited to <15°C. The temperature reported is the average temperature over the Seebeck coefficient measurement. The conductivity was measured by the four point probe technique using the thermocouples as the inner leads. The conductivity was measured at each ΔT point, and is reported as the average conductivity over the Seebeck measurement. Measurements were made in an atmosphere of 1atm of 1%H_2/He forming gas. The microstructure of SBN crystals was determined via backscatter scanning electron microscopy (BSEM) using an FEI Quanta 200 Environmental SEM.

6.3 Results and Discussion

6.3.1 Formation of NbO_2 in Single Crystal SBN

The main goal of this chapter is to elucidate the power factor values of single crystalline SBN at different reduction conditions. However, within the study of these crystals the formation of NbO_2 was found to be different than polycrystalline samples. As the NbO_2 is a marker for A-site filling and therefore the donor concentration, a discussion of these findings is necessary to understand the electron transport results. In Figure 6-1, BSEM images of polished cross sections of SBN single crystals show the microstructure evolution for annealing at 10^{-11}, 10^{-14}, 10^{-15}, and 10^{-16} atm pO_2 at 1300°C. NbO_2 is identified as the darker grey regions, due to the Z-contrast. This was confirmed via EDS.

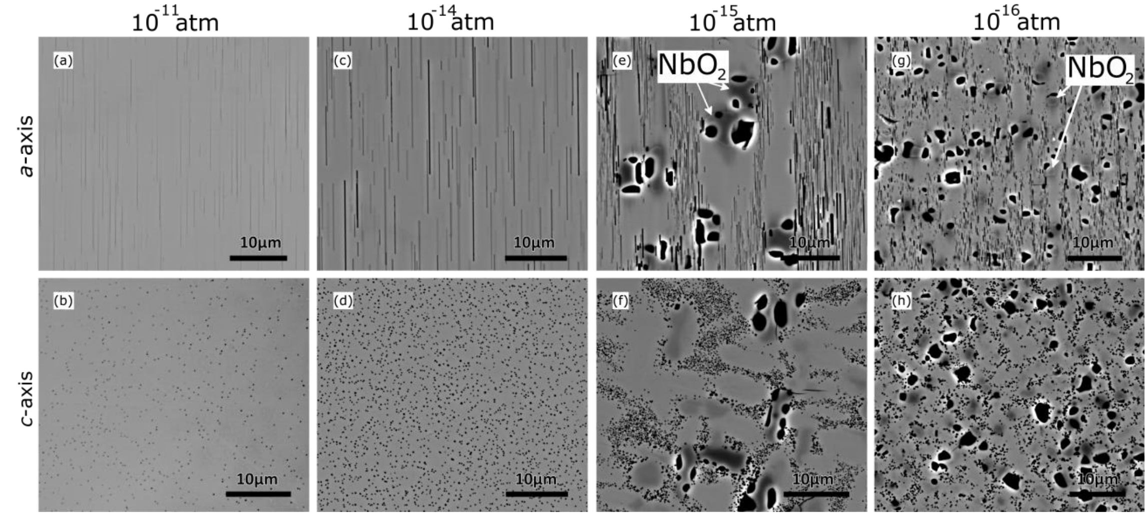

Figure 6-1. Backscatter SEM images of polished cross sections of SBN single crystals annealed at (from left to right) 10^{-11} (a,b), 10^{-14} (c,d), 10^{-15} (e,f), and 10^{-16} (g,h) atm. Cross sections are either of the (100) (top row; a,c,e,g) or (001) (bottom row; b,d,f,h) planes.

For reference: NbO_2 formation in polycrystalline samples annealed at 1300°C begins between 10^{-12} and 10^{-13} atm pO_2 (see Figure 5-2). No NbO_2 is found in the bulk of 10^{-14} atm pO_2 crystals

(Figure 6-1c and 6-1d); however, NbO_2 does form on the surfaces of single crystals annealed under this condition (See Figure 6-2).

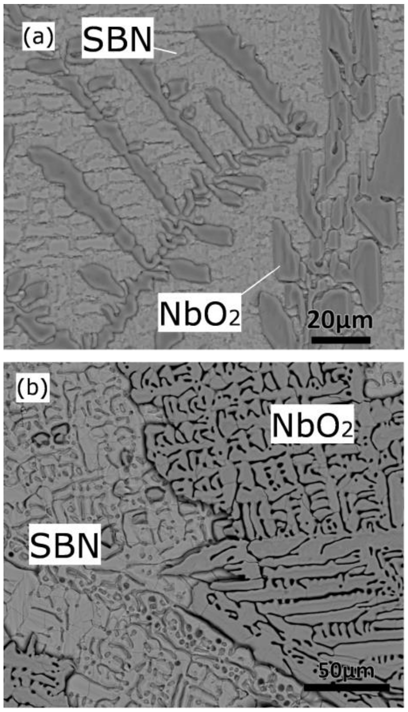

Figure 6-2. Backscatter SEM images of the (a) (100) and (b) (001) surfaces of an SBN single crystal annealed at 1300°C for 30 hours under 10^{-14} atm pO_2. In Figure 6-2b, an area is presented where the surface NbO_2 has spalled off, revealing an underlying layer of a porous SBN phase. Similar surface phases are found for crystals annealed under 10^{-15} and 10^{-16} atm pO_2.

The formation of NbO_2 on the surface of crystals, but not in the bulk, suggests that the homogeneous nucleation energy for NbO_2 formation has not been overcome under the 10^{-14} atm pO_2 annealing condition. In contrast, when annealing pO_2 is decreased to 10^{-15} atm or 10^{-16} atm NbO_2 nucleates in the bulk. This is likely due to an increased change in the Gibbs free energy during NbO_2 formation under lower pO_2 anneals. Porosity located adjacent to NbO_2 nuclei (Figures 6-1e through 6-1h) presumably forms as a result of the volume change during the transition.

An unexpected result is the presence of high aspect ratio porosity (~1-30μm long by ~100nm wide), a universal feature which is best seen in Figures 6-1c and 6-1d.Within the 10^{-11}

and 10^{-14} atm pO_2 samples these pores are homogeneously distributed, while in the 10^{-15} and 10^{-16} atm pO_2 samples their distribution is heterogeneous. The heterogeneous spatial distribution of the pores in the lower pO_2 samples seems to be in relation to the formation of NbO_2, as no pores are found directly above or below the NbO_2 particles along the *c*-axis of crystals (the *c*-axis is aligned vertically for the SEM images of the (100) surfaces, Figures 6-1e and 6-1g). This interplay between the NbO_2 and the high aspect ratio porosity is currently not well understood. It is clear that the formation of the elongated porosity requires the formation of new surfaces, and therefore must overcome the energy barrier to provide the additional surface energy required, but it is unclear what the source of this energy is. Under these annealing conditions, SBN is near the phase boundary for NbO_2 formation (See Figure 5-2). Perhaps the energy comes from a Gibbs free energy change due SBN entering a new phase region, but within the current dataset this is simply a conjecture.

The A-site filling is thought to be the cause for the large carrier concentrations of polycrystalline oxygen deficient SBN, and it may be that the electrical conductivity is severely reduced without homogeneous NbO_2 formation.(see section 5.3.2) To test the differences between the scenarios where NbO_2 does and does not form, crystals equilibrated at 10^{-14} atm pO_2 were compared with and without homogenous NbO_2 formation. This was performed by first annealing crystals under reduction conditions which lead to formation of NbO_2, and then re-annealing at 10^{-14} atm pO_2. The electrical conductivities of the crystal were recorded after the initial anneal and after each of multiple 30 hour anneals at 10^{-14} atm pO_2. The results are shown in Figure 6-3.

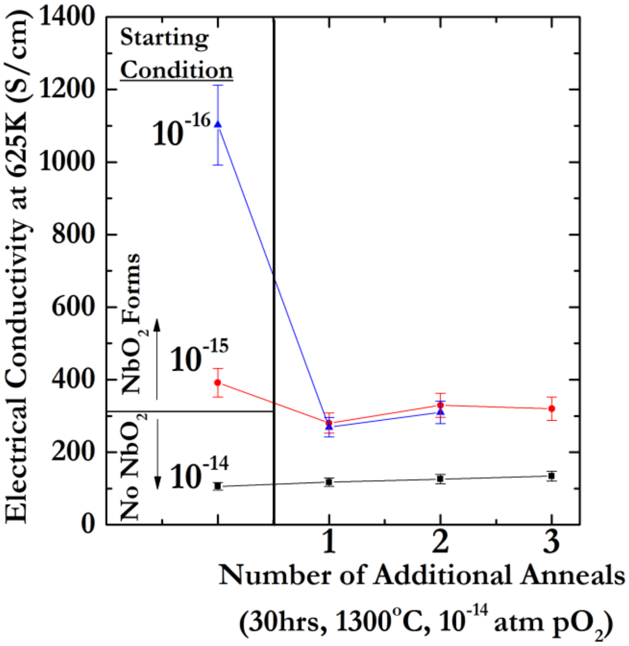

Figure 6-3. The electrical conductivities for *c*-axis oriented SBN crystals as a function of annealing time at 10^{-14} atm pO_2 after first annealing in different annealing conditions to either allow or disallow bulk NbO_2 nucleation.

The initial electrical conductivities show large differences. This is expected as the crystals are equilibrated to different annealing conditions. Subsequent anneals at 10^{-14} atm pO_2 show a convergence of both the $10^{-15}\rightarrow10^{-14}$ and $10^{-16}\rightarrow10^{-14}$ atm pO_2 crystals. The electrical conductivities did not change heavily after subsequent anneals, suggesting equilibrium was reached on the first 30 hour anneal. The $10^{-14}\rightarrow10^{-14}$ atm pO_2 crystal shows only a small increase in electrical conductivity after the additional 30 hours of annealing, and this trend continues up to 120 hours of total annealing time.

The presence of NbO_2 in crystals is not discussed by Lee et al. [9]. However, it is clear that NbO_2 formation does not occur in the bulk of crystals annealed under 10^{-14} atm pO_2, and that this affects the electrical conductivity. As the 10^{-14} atm pO_2 condition is on the border of forming NbO_2, slight variations in temperature, annealing pO_2, or crystal quality may affect the formation of NbO_2 in the bulk. Due to this uncertainty, the electron transport properties of crystals annealed under both the 10^{-14} atm pO_2 condition and the $10^{-16}\rightarrow10^{-14}$ atm pO_2 condition are compared alongside the other pO_2 conditions below.

6.3.2 Electron Transport Properties

Figure 6-4 shows the electrical conductivity, Seebeck coefficients, and power factors for *a*-axis and *c*-axis SBN single crystals annealed at 1300°C for 30 hours under 10^{-14}, 10^{-15}, 10^{-16}, and $10^{-16}\rightarrow10^{-14}$ atm pO_2. As the pO_2 during annealing is reduced, an increase in the electrical conductivity and a decrease in the Seebeck coefficient occur. This is consistent with an increase in the carrier concentration. The $10^{-16}\rightarrow10^{-14}$ atm pO_2 sample shows an increased electrical conductivity and decreased Seebeck coefficient compared to the 10^{-14} atm pO_2 sample. This suggests a higher carrier concentration, presumably due to an increase in the A-site donor concentration.

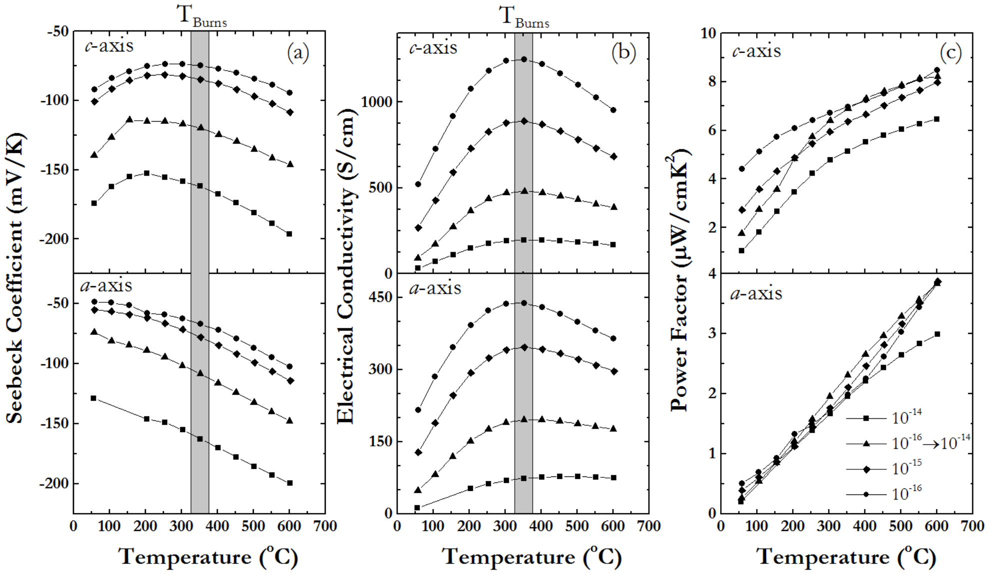

Figure 6-4. Seebeck coefficients (a), electrical conductivities (b), and power factors (c) of SBN single crystals annealed at 1300°C for 30 hours under various oxygen partial pressures.

The Seebeck coefficients show different temperature dependencies in the *a* and *c*-axis crystals. The *c*-axis crystals show a decreasing Seebeck coefficient at low temperatures, while at high temperature the Seebeck coefficient increases with temperature. Note the y-axis scale of Figure 6-4a, where the magnitude of the Seebeck coefficient decreases moving away from the origin along the y-axis. In contrast to the c-axis, the Seebeck coefficient of *a*-axis crystals increases over the entire temperature range. These two behaviors mimic the temperature dependencies of relaxor ferroelectric and normal ferroelectric compositions of SBN, respectively.[142] In chapter 4 it was explained that the increased Seebeck coefficient below the Burns temperature was a result of the relaxor ferroelectric polarization. As the *c*-axis is the polar axis of the structure, it may be that the ferroelectric polarization is responsible for the anisotropy in the temperature dependence. Above the Burns temperature, both the *a*-axis and *c*-axis show nearly identical temperature trends and magnitudes of the Seebeck coefficient. Below the Burns temperature, where ferroelectric polarization is finite, the *c*-axis deviates from the *a*-axis. The change from roughly isotropic behavior to anisotropic behavior correlates well with the Burns temperature, suggesting that the polarization along the *c*-axis is the cause. However, further work on additional samples is necessary to confirm this. Specifically, if the ferroelectric polarization is the cause of the anisotropic behavior, than this anisotropy should not exist in non-ferroelectric tungsten bronze single crystals. Study of this behavior in other tungsten bronze crystals is an interesting avenue for future work.

A transition in the electrical conductivity from semiconducting behavior at low temperatures to metallic-like behavior at high temperatures occurs for all samples measured in the current study. The location of this transition is quantified by the temperature of maximum conductivity, $T_{\sigma Max}$. Identical transitions in SBN have been discussed previously by multiple authors [142, 176, 177, 191, 216]. It has been hypothesized that this transition occurs due to the onset of relaxor ferroelectricity [32] because the $T_{\sigma\mathrm{Max}}$ and T_{Burns} in SBN correlate well [32, 142, 216]. Moreover, similar phenomenon have been seen in other oxygen deficient ferroelectrics [216]. However, analysis of the literature points to this being a coincidental correlation. First, although the correlation between $T_{\sigma\mathrm{Max}}$ and T_{Burns} holds for the relatively narrow set of reduction conditions investigated in the current study, other studies have shown that $T_{\sigma\mathrm{Max}}$ will shift when a wider set of reduction conditions are considered. For example, Li et al. [212] reports a $T_{\sigma\mathrm{Max}}$ of 550°C for $(Sr_{0.6},Ba_{0.4})Nb_2O_{6-\delta}$ annealed at 1100°C under Argon compared to the $T_{\sigma\mathrm{Max}}$ of 350°C reported here. Secondly, $(Ca_{0.18},Ba_{0.82})Nb_2O_{6-\delta}$, which is isostructural to SBN, when reduced under forming gas for 25hrs at 1000°C shows a $T_{\sigma\mathrm{Max}}$ of 260°C[191] while the unreduced samples shows a T_{Burns} of 930°C[150]. Finally, reduced samples of non-relaxor ferroelectric compositions of SBN, which should not have any relaxor ferroelectric polarization, still show a $T_{\sigma\mathrm{Max}}$ of 350°C[142]. Nevertheless, changes in the conduction mechanism were found at the Burns temperature of relaxor ferroelectric samples[142, 191] suggesting that ferroelectricity does play a role in coupling to electron transport. However, the connection between ferroelectricity and electron transport does not seem to be as simple as equating T_{Burns} and $T_{\sigma\mathrm{Max}}$ as has been previously hypothesized. The reason for the reduction independent $T_{\sigma\mathrm{Max}}$ in the current work is unclear, but may be due to the competing influence of the donor ionization energy, E_d, and the donor concentration, N_d, on $T_{\sigma\mathrm{Max}}$. If $T_{\sigma\mathrm{Max}}$ is equivalent to the carrier saturation temperature, then $T_{\sigma\mathrm{Max}}$ would be given by:

$$T_{\sigma\mathrm{Max}} = \frac{E_d}{k ln\left(\frac{N_c}{N_d}\right)} \tag{6.1}$$

As lower pO_2 anneals are used, the N_d would increase thus pushing $T_{\sigma\mathrm{Max}}$ upward. Simultaneously, as N_d increases, E_d decreases, pushing the $T_{\sigma\mathrm{Max}}$ downward. These competing forces may be the cause of the carrier concentration independent $T_{\sigma Max}$ found in this and other studies[176].

The *a*-axis power factors are roughly independent of reduction condition, suggesting that the $10^{-16}\rightarrow10^{-14}$ atm pO_2 to the 10^{-16} atm pO_2 conditions result in carrier concentrations near the optimum carrier concentration for thermoelectric performance. The 10^{-14} atm pO_2 condition shows slightly lower power factors above 450°C, implying that it is somewhat below the optimum carrier concentration. An identical trend is found for *c*-axis crystals at high temperatures, with the $10^{-16}\rightarrow10^{-14}$ atm pO_2 to the 10^{-16} atm pO_2 conditions showing similar power factors, while the 10^{-14} atm pO_2 shows slightly reduced power factors. However, the *c*-axis power factors show a clear pO_2-dependence at low temperatures for all samples. The cause for this is the larger *c*-axis Seebeck coefficient which is roughly ~50μV/K larger than the *a*-axis Seebeck coefficient, independent of pO_2. This additive contribution to the Seebeck coefficient increases the optimum carrier concentration for maximization of the power factor, resulting in the increasing trend from the 10^{-14} atm pO_2 to the 10^{-16} atm pO_2 annealing condition.

The maximum power factor measured in the current work is 8.4 $\mu W/cmK^2$ at 650°C in the *c*-axis 10^{-16} atm pO_2 crystal. This falls below the previous report of $19\mu W/cmK^2$ at 250°C[9]. To compare these results, the electron transport properties of crystals from literature [9] are plotted alongside data from the current manuscript in Figure 6-5.

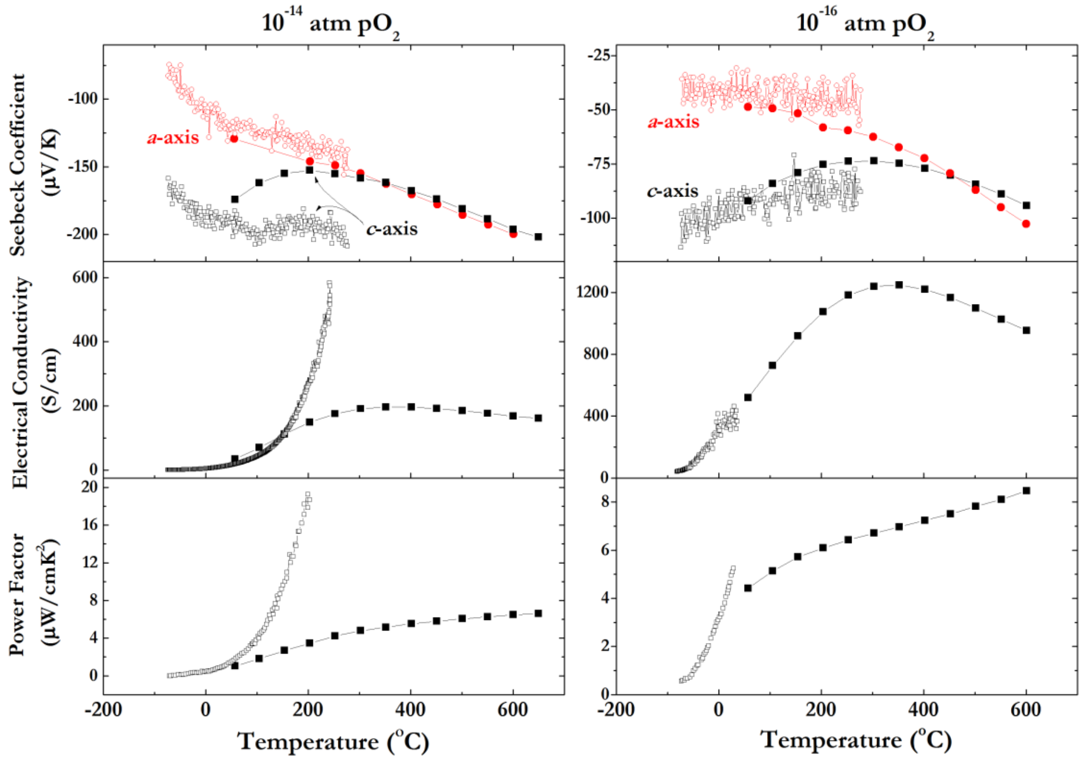

Figure 6-5. Comparison of Seebeck coefficients, electrical conductivities, and power factors of 10^{-14} and 10^{-16} atm pO_2 single crystals; Current work (closed symbols) and Lee et al. (open symbols)[9].

A majority of the Seebeck coefficient values for crystals measured in the current dataset and from Ref [9] are similar in magnitude. The primary exception is that the Seebeck coefficients of the two 10^{-14} atm pO_2 *c*-axis SBN crystals differ by ~40μV/K at 250°C. However, the temperature dependencies of the Seebeck coefficients seem to be roughly consistent between the two datasets.

Near room temperature the electrical conductivities from Ref [9] and the current work agree well. However, starting at 150°C the 10^{-14} atm pO_2 crystal from Lee et al. deviates toward higher electrical conductivities, resulting in a difference of roughly 2.7x at 250°C. The temperature dependence of the two 10^{-14} atm pO_2 samples also differs. The electrical conductivity of sample measured by Lee et al. increases roughly exponentially, while the sample measured in this work, as well as all other samples of this work and from Lee et al., go through an inflection point and eventually a maximum. The difference between the currently measured power factor at 250°C for a 10^{-14} atm pO_2 crystal, 4.2μW/cmK^2, and the value reported by Lee et al, 19μW/cmK^2, is ascribed to differences in both the reported Seebeck coefficients and electrical conductivities.

As the 10^{-14} atm pO_2 annealing condition sits near the edge of homogenous NbO_2 nucleation, slight changes in annealing conditions may cause drastic differences in properties. However, both samples with and without NbO_2 nucleation (the $10^{-16} \rightarrow 10^{-14}$ and the 10^{-14} atm pO_2 samples, respectively) show lower power factors than the sample from Ref [9]; therefore, processing differences are not thought to be the cause of the discrepancy between the work of Lee et al. and the current work. Currently, the cause of the discrepancy is unknown. As the entirety of the current dataset agrees with the work of Lee et al. bar the *c*-axis 10^{-14} atm pO_2 samples and the currently measured 10^{-14} atm pO_2 sample shows systematic behavior within the dataset, the 10^{-14} atm pO_2 sample from Lee et al. is thought to be anomalous.

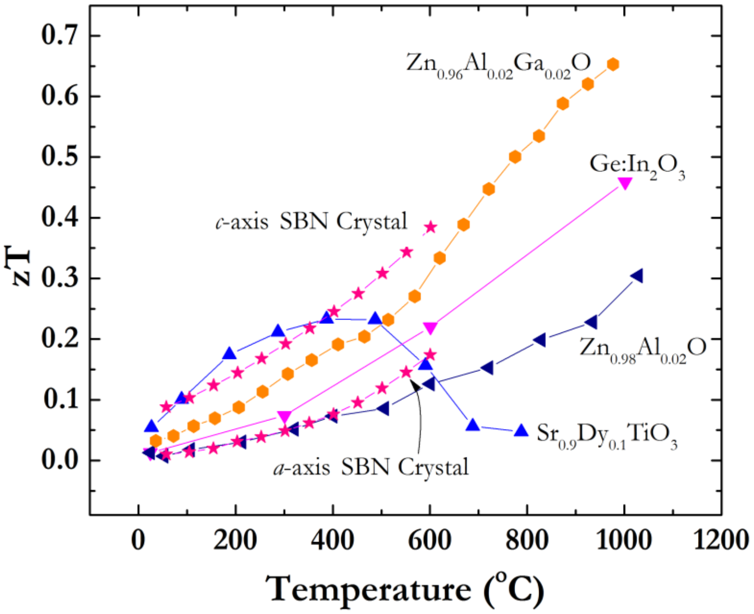

Figure 6-6. zT of a 10^{-16} atm pO_2 annealed *c*-axis and *a*-axis single crystals of $Sr_{0.6}Ba_{0.4}Nb_2O_6$ using polycrystalline values of the thermal conductivity from Ref [185]. zT values of other n-type oxide thermoelectrics are from References [6, 110, 114, 217]

The zT values for the 10^{-16} atm pO_2 crystal are plotted alongside other promising n-type oxide thermoelectrics in Figure 6-6. As thermal conductivity measurements are difficult on the small size of samples measured here, thermal conductivity values from polycrystalline samples are substituted[185]. A caution should be advised for this substitution, as the polycrystalline samples likely did not show significant amounts of porosity and the thermal conductivity is likely anisotropic, but the substitution does allow for a rough estimate of zT. With this stated, the calculated zT value for *c*-axis SBN annealed under 10^{-16} atm pO_2 is ~0.38 at 600°C. This value is on par with other state-of-the-art oxide thermoelectrics, as shown in Figure 6-6. The *a*-axis shows a lower zT but still reaches a value of roughly 0.17 at 600°C. These values suggests that the tungsten bronze structured materials are an interesting avenue for future oxide thermoelectrics.

6.4 Summary

The NbO_2 formation in and thermoelectric properties of reduced $(Sr_{0.6},Ba_{0.4})Nb_2O_6$ single crystals were investigated. The NbO_2 formation of single crystals show similar pO_2 dependencies to that of polycrystalline samples in literature, although the lack of grain boundaries for heterogeneous nucleation of NbO_2 limits the formation of NbO_2 in the bulk of crystals at 10^{-14} atm pO_2 at 1300°C. A successful route for overcoming this limitation was to pre-anneal crystals at harsher reduction conditions to seed the crystals with NbO_2 nucleates followed by re-equilibration at 10^{-14} atm pO_2. The Seebeck coefficient along the *c*-axis and *a*-axis of samples show dependencies reminiscent of relaxor ferroelectric and normal/non-ferroelectric samples, respectively. This suggests that the polarization along the *c*-axis is the cause for the increase in the Seebeck coefficient below the Burns temperature in relaxor ferroelectric SBN. The maximum power factor for an SBN single crystal measured in this study was 8.5 μW/cmK^2. This value falls below the previously measured values of 19μW/cmK^2 at 250°C[9], but still results in a zT of ~0.38 at 600°C if polycrystalline values of the thermal conductivity are assumed. This value falls below the previously measured values of 0.75 at 250°C, but are still large for an n-type oxide in this temperature range.

Chapter 7
Conclusions and Future Work

These sections will overview the major findings of this thesis. Possible avenues of future work are detailed in light of these results.

7.1 Conclusions

7.1.1 Coupling Between Ferroelectricity and Electron Transport

The electrical conductivity of a variety of oxygen deficient ferroelectric materials was measured as a function of temperature and it was shown that in $(Ba_{1-x}Sr_x)TiO_{3-\delta}$ the metallic-like to nonmetallic transition temperature can be shifted via Sr doping; furthermore, the temperature shift is equivalent to the shift in the paraelectric-ferroelectric transition temperature in non-reduced samples. This points toward a connection between the ferroelectric nature of materials and the stifling of metallic conduction. However, it has been shown that the metal-to-insulator transition does not always lay near the Burns temperature of $(Sr_{1-x},Ba_x)Nb_2O_{6-\delta}$ samples, as was previously hypothesized. The metal-to-insulator transition may instead be a saturation of electronic carriers from an impurity band. The Burns temperature does mark a change in the activation energy of electronic conduction in SBN samples and the onset of an increasing Seebeck coefficient on cooling.

These results do not eliminate the possibility of metallic conduction in the ferroelectric state. In fact, a metallic ferroelectric has been identified by other authors in $LiOsO_3$.[134] These results instead suggest that materials in which ferroelectric distortions and the conduction band primarily originate from the same cationic sublattice – here the d^0 cations – a cross-coupling effect between ferroelectricity and the electronic conduction suppresses metallic conduction.

Anderson localization is a likely mechanism for this coupling, although additional coupling mechanisms may exist such as changes in the band structure and spatial redistribution of electronic carriers. Further research is needed to fully understand the extent of ferroelectricity on electronic conduction.

7.1.2 Electron Transport in $(Sr_x,Ba_{1-x})Nb_2O_{6-\delta}$

The electrical conductivity, Seebeck coefficient, and polarization-induced lattice strain of $(Sr_x,Ba_{1-x})Nb_2O_{6-\delta}$ were investigated for $0.4<x<0.7$. At low temperatures conduction occurs by hopping of electrons via these localized states, resulting in characteristic $T^{-1/4}$ behavior. As temperature rises, electronic conduction is well modeled by activation of electrons over a temperature-dependent gap. Within this high temperature region the electronic mobility is well above the Bosman & van Dall[218] limit for polaron mobility ($\mu << 0.1 cm^2/Vs$), necessitating band conduction. Given the low temperature hopping behavior, high temperature band conduction, and large carrier concentration ($\sim 10^{21}$/cc), an electron transport model is proposed where the Fermi energy lies within an impurity band of localized electronic states located below a the delocalized *d*-orbital band. As relaxor ferroelectricity is introduced via compositional modification of the A-site, an increase in the activation energy for electronic conduction is found, but only below the Burns temperature. The effect of relaxor ferroelectricity is thought to be due to the introduction of short-range order polarization which acts as a source of Anderson localization.

7.1.3 Formation of the NbO_2 Secondary Phase and Resulting Changes in the SBN Matrix

It was found that enhanced electrical conductivity in oxygen deficient SBN correlates with the appearance of an NbO_2 secondary phase. NbO_2 forms at different pO_2 conditions as a function of temperature. It is found that the NbO_2 develops once a critical oxygen vacancy concentration is reached. Past the oxygen vacancy solubility limit, harsher reduction treatments result in increased amounts of NbO_2 accompanied by an increase in the (Sr+Ba):Nb ratio of the SBN matrix. The increased (Sr+Ba):Nb ratio is facilitated by a concomitant rise in the A-site occupancy of the SBN matrix. The additional A-site cations act as donor defects, and cause the large carrier concentrations which are the source of the enhanced electrical conductivity necessary for the high thermoelectric performance of oxygen deficient SBN.

7.1.4 Phase Equilibrium Analysis of A-site filling in Oxygen Deficient SBN

To better understand the A-site filling, the phase equilibria of $(Sr_{0.6},Ba_{0.4})_{1+y}Nb_2O_{6-\delta}$ y=0-0.2 was examined as a function of pO_2 at 1300°C. It is found that a solid solution exists between $(Sr_{0.6},Ba_{0.4})Nb_2O_{6-\delta}$ and $(Sr_{0.6},Ba_{0.4})_{1.2}Nb_2O_{6-\delta}$; EDS measurements found that increasing the initial Sr and Ba concentration resulted in the occurrence of A-site filling at more modest reduction conditions. The solid solution is bounded by the oxygen vacancy solid solution limit at low pO_2 and the partial Schottky solid solution limit at high pO_2. It was shown that increasing the (Sr+Ba):Nb in the starting batch results in an increased chemical potential for A-site stuffing and affects the critical oxygen activity for second phase formation. This provides an interesting route toward control of the carrier concentration in thermoelectric SBN via the A-site filling.

7.1.5 Defect Chemistry of the Low Temperature Reoxidation of A-site Filled Strontium Barium Niobate

Thermogravimetric analysis of the reoxidation process shows that oxygen absorption starts to occur at ~250°C, and this poor oxidation resistance is a problem that must be solved for use of SBN thermoelectric elements in air. The amount of oxygen absorbed, as measured by

TGA, was found to be the correct amount to completely compensate the A-site donors, and this was confirmed using Hall measurements. The lack of oxidation resistance is detrimental to the application of SBN as a thermoelectric, but insulating samples of A-site filled SBN were obtained. These ‘superoxidized’ SBN samples have shown shifts in the permittivity to lower temperatures and decreased permittivity magnitudes and may be interesting for future study in tungsten-bronze structure-property relations.

7.1.6 Thermoelectric Properties of Strontium Barium Niobate Single Crystals

The NbO_2 formation in and thermoelectric properties of reduced $(Sr_{0.6},Ba_{0.4})Nb_2O_6$ single crystals were investigated. The NbO_2 formation of single crystals follows a similar pO_2 dependence to that of polycrystalline samples, although the lack of grain boundaries limits the nucleation of NbO_2 in the bulk of the crystals. Pre-annealing crystals at harsher reduction conditions to seed the crystals with NbO_2 nuclei followed by re-equilibration at 10^{-14} atm pO_2 successfully overcame the kinetic limitation. The Seebeck coefficient along the *c*-axis and *a*-axis of samples show dependencies reminiscent of relaxor ferroelectric and normal/non-ferroelectric samples, respectively. This suggests that the polarization along the *c*-axis is the cause for the increase in the Seebeck coefficient below the Burns temperature in relaxor ferroelectric SBN. The maximum power factor for an SBN single crystal measured in this study was 8.5 $\mu W/cmK^2$. This value falls below the previously measured values of 19$\mu W/cmK^2$ at 250°C[9], but still results in a figure of merit ZT of 0.38 at 600°C if polycrystalline values of the thermal conductivity are assumed. Polycrystalline values of the power factor calculated from the *c*-axis and *a*-axis values agree with the literature on polycrystalline samples. Within the paraelectric regime, the power factor changes little as a function of reduction between 10^{-14} and 10^{-16} atm pO_2, suggesting these reduction conditions are near the power factor maximum as a function of carrier concentration.

At temperatures below ~200°C, however, the additional Seebeck coefficient contribution along the *c*-axis moves this maximum toward larger carrier concentrations and the 10^{-16} atm pO_2 sample results in the largest room temperature power factor.

7.1.7 Effect of Current Results on the Design of Relaxor-Ferroelectric Based Thermoelectrics

The final set of conclusions necessary is to discuss this work in its totality as to how it relates to the design of relaxor-ferroelectric based thermoelectrics. The driving idea behind the use of relaxor-ferroelectric based thermoelectrics is the decrease of the thermal conductivity due to the scattering of phonons by nanosized polar regions. The thermal conductivity is not the only necessary design parameter, however. All the thermoelectric properties must be optimized to increase the figure of merit. The work of Chapters 3 and 4 show that relaxor ferroelectricity most likely increases Anderson localization. This increased Anderson localization converts many of the highly mobile band-conducting electron to localized electrons. The effect of this can be thought of as an effective decrease in the carrier concentration. Therefore, although relaxor ferroelectricity lowers the thermal conductivity, a higher electrical carrier concentration is necessary to offset the increased localization. This can be seen, for example, in Figure 6-4c. All samples in the paraelectric phase show carrier concentrations independent power factors, but, within the relaxor ferroelectric regime, the power factor has a clear carrier concentration dependence. This suggests that the peak carrier concentration (Figure 2-21) for these samples shifts to higher values within the relaxor ferroelectric regime.

Although on the surface this is as simple as increasing the donor concentration, increasing the donor concentrations in oxides may be difficult to achieve due to solid solubility limits. [114] The solid solubility limit here has been circumvented via A-site doping during reduction. Different doping techniques will be necessary in the future to overcome the limitation of oxidation resistance at the temperature of applicaiton.

7.2 Future Work

The current work within this dissertation has been focused on a singular material – strontium barium niobate. Power factors along the *c*-axis have been shown to have values similar to other state-of-the-art n-type oxides and, in conjunction with the low thermal conductivity, have shown figure of merits on-par with the best n-type oxide thermoelectrics to date. This is an impressive proof of concept for ferroelectric-based thermoelectrics. However, moving thermoelectric-ferroelectrics forward should not necessarily continue this focus on optimizing a single material. Instead, future work should focus on identifying trends within these material systems and optimizing the thermoelectric properties based on these trends. The future work laid out here mainly focuses on projects based on this premise.

7.2.1 Investigation of Changes to the Ferroelectric Properties as a Function of A-site Filling and Oxygen Content

Doping for tungsten bronze thermoelectrics will depend heavily on the substitution of A-site cations. Understanding how both the ferroelectricity and crystal structure are affected by A-site substitution is important for optimization of the thermoelectric properties. Work to ascertain the structure-property relations of tungsten bronze ceramics is currently underway by many groups, with a good summary given in Ref [199]. Proposed here is a study specifically designed to elucidate a missing piece of that literature.

As discussed in section 5.1, many types of tungsten bronzes exist. The ferroelectric properties are of tungsten bronzes are dependent on the crystal structure in multiple ways. For example, an analysis of many tungsten bronzes has shown that relaxor ferroelectricity occurs in samples with incommensurate structures.[219] These structures are enabled by a high A1-site tolerance factor and small average A-site cation radii.[199] This model has explained previous results which show that A-site cation radii play a role in the normal vs. relaxor ferroelectric transition in unfilled bronzes. [220] However, little is known about how cation vacancies affect these trends. These include the filled, unfilled, and empty varieties which are distinguished by the structure of A-site cation vacancies. Opening up the design space for tungsten bronze ferroelectric-thermoelectrics requires understanding of how the A-site vacancies affect thermoelectric and ferroelectric properties. It was hypothesized by Zhu et al. that cation vacancies permit a relaxation of the frustrated tilt network that gives rise to the incommensurate modulation, thereby allowing for commensurate modulations to take place.[199] In other words, cation vacancies should push samples toward normal ferroelectric behavior. Normally, cation vacancy concentration is modified by doping the A-site with aliovalent cations. This convolutes two variables – cation size and vacancy concentration. SBN, however, is an interesting system to investigate, as the A-site occupancy is easily modifiable without addition of separate cation species. Phase pure samples of SBN with different A-site occupancies can be fabricated following the phase diagram in Figure 4-5, resulting in $(Sr_x,Ba_{1-x})_{5+y}\square_{1-y}Nb_{10}O_{30}$. This is not a perfect solution, however, as the carrier concentration will change with A-site filling. However, given that it has been suggested that steric phenomena are an underlying cause of the changes to tilting, the carrier concentrationshould be of smaller consequence than the cation size.

As for practical experimental details, $(Sr_x,Ba_{1-x})_{5+y}\square_{1-y}Nb_{10}O_{30}$of x=0.4 and y=0, 0.2, 0.4, 0.6, 0.8, and 1 may be investigated. A Sr concentration of 40% is suggested to insure that the y=0 compositional end member is a normal ferroelectric, as the test is to see if filling of the vacancies converts the sample to a relaxor ferroelectric. The theory laid out in Ref [199] shows that the structural changes which determine normal vs relaxor ferroelectricity are the incommensurate vs. commensurate tilting of the octahedral. The tilting structure of the different samples may be investigated via electron diffraction patterns via transmission electron microscopy, and the ferroelectric nature of samples can be determined via temperature dependent XRD as discussed in section 3.3.2.

During measurement, samples must not be allowed to oxidize as the additional oxygen absorbed by the lattice may affect the tilt structure, as discussed in section 4.3.4. The strategy for mitigating high-temperature oxidation is to use capillaries similar to section 3.3.2. The Advanced Photon Source beamline 11-BM allows for temperature-dependent XRD measurement of capillary samples up to 1000°C. The greater accuracy of lattice parameters obtainable from 11-BM compared to beamline 6-ID-D, the beamline used for the current thesis, would enable qualitative determination of the magnitude of the polarization as a function of temperature. The data would be qualitative only because the values of the electrostrictive coefficients Q_{33} and Q_{31} are necessary for data quantification, and even if these were available or measured on unreduced samples, the change in Q_{33} and Q_{31} as a function of filling cannot be determined easily in conducting samples. The combination of TEM and XRD data would allow for correlation of the tilting structure and ferroelectric behavior in SBN over the filling transition. Over the filling transition the electronic carrier concentration will change. This has been known to affect the stability of the ferroelectric phase via screening of the ferroelectric polarization[32], but the screening may be of less importance here as octahedral tilting should be less sensitive to electronic carriers than the ferroelectric transition. Despite this complication, the nature of the ferroelectricity (normal vs relaxor) is the key parameter to be measured and not the phase transition temperature.

Additionally, the A-site filled SBN structure can be perturbed via the use of 'super-oxidized' $(Sr_x,Ba_{1-x})_6Nb_{10}O_{30+\delta}$. Filled SBN can be oxidized in air below ~600°C and retain phase purity while absorbing enough oxygen to electronically compensate the A-site donors (see section 4.3.4). The location of the oxygen in these super-oxidized samples is unknown, but clearly should act to perturb the tungsten bronze structure and therefore should affect the dielectric properties. Preliminary dielectric properties of these insulating samples have been measured [211] and have been found to shift the T_{Max} to lower temperatures compared to stoichiometric SBN. Understanding these changes within a crystal chemical framework requires knowledge of the position of the extra oxygen in the crystal structure. The location of these oxygens should be determinable via structure refinement of neutron diffraction patterns. Once the location of the additional oxygen is well understood, a link between the filling of these super-oxidative sites and the ordering of the oxygen octahedral tilts can be determined. Capacitance measurements as a function of frequency and temperature can be used to discern between relaxor and normal ferroelectric behavior.

An additional benefit of this research is investigation into any octahedral tilting which may occur simultaneously. Octahedral tilting is important to the electronic conduction of tungsten bronze thermoelectrics as the d-orbital bandwidth decreases with increasing oxygen octahedral tilt angle[221, 222] with the largest bandwidth at an O-Nb-O angle of 180°. Control of the oxygen octahedral tilt angle is currently difficult from a crystal chemistry point of view as the knowledge of the tungsten bronze structure is not as robust as those of perovskites. However, some information has been gleamed from previous research. Zhu et al. proposed that the oxygen octahedral tilt angle is dependent on the radius ratio between the A1 and A2 sites [223]. This is based on the example of $(Sr_x,Ba_{1-x})Nb_2O_6$ where the Nb-O-Nb angle changes from 175.5° to 174.4° to 172.5° for x=0.25, 0.50, and 0.75 respectively[124], suggesting that moving the radius ratio toward 1 will increase the oxygen octahedral tilting angle. However, in $Ca_{0.28}Ba_{0.72}Nb_2O_6$, where Ca shows a strong preference for the A1 site, a Nb-O-Nb angle of 169° is found, supporting the opposite trend[224]. It has been shown that increases in tetragonality have been linked to stabilization of the ferroelectric phase, and these increases in tetragonality correlate with increases in ionic radii in both the B-site cations[225] and the A-site cations[220]. This suggests that larger cation sizes will result in decreased oxygen octahedral tilt angles, although the tetragonality term is convoluted with the presence of octahedral tilt around the [001] direction. Filling of A-site cations during the reduction of SBN seems to be well suited to test if A-site vacancies heavily affect the tilt angle. The tilt angle may be measured as a function of site filling via structure refinements. As the lattice parameter of SBN increases upon A-site filling [201, 226] it is thought that this tilt angle is decreasing with filling, thereby increasing the electron mobility.

7.2.2 Determination of Thermal Conductivity in a Variety of Normal and Relaxor Ferroelectric Tungsten Bronzes

The thermal conductivity of Strontium Barium Niobate is glasslike at low temperatures [32]. This fact was a major point of interest when choosing SBN as potential ferroelectric-thermoelectric. Early papers suggested that the glasslike thermal conductivity is primarily due to the relaxor ferroelectric nature of SBN. The results of Li et al.[185] show that Ba-rich, oxygen deficient SBN shows similar glasslike behavior. The Seebeck behavior, however, suggests that the samples are normal ferroelectrics.[185] If these glasslike samples are indeed normal ferroelectrics, then the glasslike nature of SBN may not primarily be due to relaxor ferroelectricity. This is not an impossibility, as neutron scattering measurements of SBN show that low-lying optic phonon modes intersect the acoustic phonon modes[227], and this intersection, similar to clathrates[60], may be the cause of the low thermal conductivity of SBN. If the low thermal conductivity is not due to relaxor ferroelectricity, then the idea of ferroelectric-based thermoelectrics may be unnecessary and instead focus should shift toward tungsten bronze structured thermoelectrics outside of the subset of relaxor ferroelectric tungsten bronzes. If relaxor ferroelectricity is not necessary, this vastly opens the design space of tungsten bronze thermoelectric, giving greater hope of finding a possible high-zT material within the tungsten bronzes. It is imperative that the role of relaxor ferroelectricity be determined, as this will allow for better future planning of where to focus energy on the design of tungsten bronze thermoelectrics.

To understand if the thermal conductivity is due to relaxor ferroelectricity or the 'rattling' of A-site cations, a series of samples may be measured which range from normal to relaxor ferroelectric behavior. This may be done in SBN via changing the Sr:Ba ratio, similar to that which was done in Chapter 3. It may seem very similar to the work of Ref. [185], but the key difference is the lack of A-site filling and electronic carriers. Outside of the measurement of Figure 4-4 clear evidence on how A-site filling affects ferroelectric polarization is not available. Therefore, it is simpler to investigate a system which is will understood – the unreduced variety of strontium barium niobate. The ferroelectric properties can be easily understood using capacitance vs temperature and frequency measurements to determine the normal or relaxor ferroelectric nature, and this can be correlated to temperature-dependent thermal conductivity experiments via laser flash diffusivity. If normal ferroelectric samples of SBN show glasslike behavior similar to the Ba-rich samples of Ref. [185] then it would be shown that relaxor ferroelectricity is not the cause of the glasslike nature. This does not, however, prove that relaxor ferroelectricity does not play a role in the scattering of phonons. Domain walls have been shown via separate means to act as phonon scattering sites [7, 8]; however, if relaxor ferroelectricity is not necessary for the lowering of thermal conductivity for tetragonal tungsten bronze thermoelectrics, than the ability to move away from the restrictive compositional space of only relaxor ferroelectrics is lifted. This would enable further optimization of these tungsten bronze thermoelectrics.

7.2.3 Increasing Stability of $(Sr_x,Ba_{1-x})_{1+y}Nb_2O_6$ in Air

For SBN to be a practically useful thermoelectric material, it must be stable at high temperatures (>450°C) in air. The large power factors found in SBN are only achieved once samples are equilibrated under reducing conditions and, as shown in section 4.3.4, on re-equilibration in air, samples revert back to an insulating state. For real-world applications, retention of the large power factors in air is necessary.

The processing of SBN in reducing atmospheres creates oxygen vacancies and increases the A-site occupancy. In samples with increased A-site occupancy, the additional 2+ cations sitting on normally vacant A-sites, $A_{V_A^x}^{\cdot\cdot}$, are the major donor species. This means that if the oxygen vacancies are filled without perturbing the $A_{V_A^x}^{\cdot\cdot}$, the electronic carrier concentration should show only minor changes. Unfortunately, annealing A-site filled samples in air fills not only the oxygen vacancies, but additional oxygen is absorbed. This additional oxygen compensates the A-site donors and therefore the material becomes insulating. The location of these A-site compensating oxygen defects in the lattice is currently unknown. If the location of the A-site compensating oxygen can be identified, then a doping strategy could be devised to kinetically constrain their formation. For example, one possible site for the A-site compensating oxygen is the empty C-site, as it is the largest empty volume in the crystal structure. If this is the location of the additional oxygen, then addition of Li^+ onto the C-site could severely hinder oxygen diffusion along the channels of C-sites. This will not prevent the formation of oxygen once equilibrium is reached, but may kinetically constrain oxygen absorption. It is unlikely that this strategy alone will make samples fully oxidation resistant, but co-doping may help in conjunction with additional strategies.

Another possibility is to block oxygen absorption via a coating on the material surface. There are many types of possible coating processes which include, but are not limited to, atomic layer deposition (ALD), dip coating of a sol-gel film, sputtered coatings, chemical vapor deposition, and more. The main design parameter is for the coating is to prevent oxygen diffusion. A scan of the literature shows potential in Al_2O_3 coatings [228–230] due to their low oxygen diffusion coefficients. Using the diffusion coefficient of $2.7 \times 10^{-19} m^2/s$ measured in Ref. [230] for an ALD-deposited amorphous Al_2O_3 film, a 10,000 hour anneal at 900°C results in a characteristic diffusion length of only ~3μm. The thermal expansion of Al_2O_3 and SBN are similar with values of $8\text{-}9 \times 10^{-6}/°C$ for Al_2O_3 [231, 232] and $9 \times 10^{-6}/°C$ for SBN75[175], suggesting that films could remain crack-free during operation over 0-1000°C. There are many approaches to prepare alumina films, including pulsed laser deposition[233], chemical vapor deposition[234, 235], spray pyrolysis[236], sputtering[237], and sol-gel processing[238–241]. Dense, crack-free 800nm films deposited by dip-coating have been fabricated via sol-gel [240] although temperatures required for removal of organics is ~600°C, and it would be necessary to investigate the oxidation of SBN during this process. Crystallization of the sol-gel Al_2O_3 could be measured via TGA/DTA, which would simultaneously measure any uptake of oxygen during the process. The quality of the coating microstructure could be determined via SEM, and the phase can be determined via grazing incidence x-ray diffraction. Oxidation resistance of the coated sample could be determined via isothermal TGA at 1000°C in flowing air.

Appendix A: Control of Oxygen Partial Pressure

Control of oxygen partial pressure is key to investigating the defect chemistry of oxide systems. The oxygen partial pressure is most commonly controlled via a reaction of gases with different oxygen contents and controlling the oxygen content via Le Chatelier's principle. In this thesis the reaction used is:

$$H_{2(g)} + \frac{1}{2} O_{2(g)} \leftrightarrow H_2O_{(g)} \tag{A.1}$$

Increasing the amount of $H_{2(g)}$ will decrease the amount of $O_{2(g)}$ and increasing the amount of $H_2O_{(g)}$ will increase the amount of $O_{2(g)}$. When a specific partial pressure of oxygen (pO_2) is required then the pH_2 and pH_2O can be controlled and the pO_2 is therefore pinned via thermodynamics. For Equation (A.1) the Gibbs free energy equation is:

$$\Delta G^o = -247{,}500 + 55.85T \text{ J} \tag{A.2}$$

where ΔG^o is the Gibbs free energy in the standard state (pressure of one atmosphere). The equilibrium constant of Equation (A.1) is:

$$K_{Eq} = \frac{pH_2O}{pH_2 * pO_2{}^{1/2}} \tag{A.3}$$

The equilibrium constant and the Gibbs free energy of a reaction are related by:

$$\Delta G^o = -RTln(K_{Eq}) \tag{A.4}$$

If Equation (A.2) is input into Equation (A.4), then:

$$\ln(K_{Eq}) = \frac{-247{,}500}{RT} + \frac{55.85}{R} \tag{A.5}$$

And insertion of Equation (A.3) with rearrangement gives:

$$pO_2^{1/2} = \frac{pH_20}{pH_2}\exp(\frac{247{,}500}{RT} - \frac{55.85}{R}) \quad (A.6)$$

The above equation shows that the partial pressure of oxygen depends on the $\frac{pH_20}{pH_2}$ ratio and temperature. The H_2O is introduced into the gas via flowing a carrier gas through a bubbler. The H_2 is introduced either directly in its gaseous form or via a mixture of H_2 and a carrier gas called forming gas. The latter is useful as it is not flammable.

Two drawbacks of controlling pO_2 via pH_2/pH_2O mixtures are the temperature dependence of pO_2 and the limited pO_2 range. The temperature dependence of pO_2 can be seen in Equation (A.6) and means that during a furnace run a decreasing temperature will result in an increased pO_2. This increased pO_2 can result in reoxidation of samples during furnace cooling. This could lead to, for example, reoxidation of the grain boundaries of a reduced ceramic resulting in an accidental barrier layer capacitor. Quenching under low pO_2 may be needed to alleviate this reoxidation problem.

The limited pO_2 range of pH_2/pH_2O mixtures is seen in Figure A-1 for H_2 flow of 1sccm-50sccm and N_2 flow through a water bubbler of 10sccm-500sccm

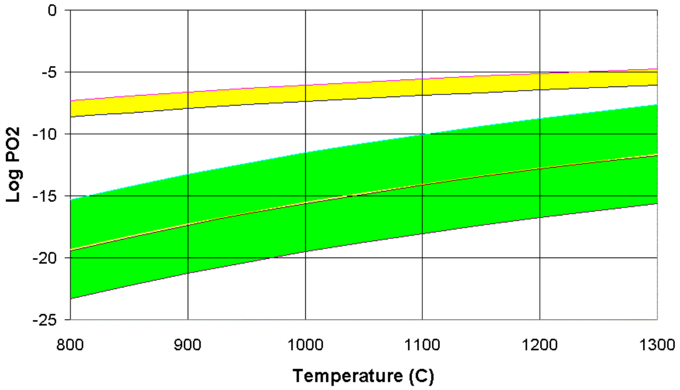

Figure A-1. pO_2 values obtainable from a 50sccm H_2 and 500sccm N_2 mass flow controller through a room temperature water bubbler (green area) and flow of N_2 through a H_2O bubbler only (yellow area).

The limited pO_2 range is an experimental limitation. Gas flowmeters have a maximum and minimum specified flow rate and therefore limit the range of deliverable pH_2 and pH_2O. The high-pO_2 range can be extended if pre-mixed gasses are used to source H_2 (e.g. replacing pure H_2 flow for 5% H_2/Ar forming gas). One must be careful in this scenario, however. Mass flow controllers are calibrated for a specific gas as the flow measurement depends on the heat capacity and thermal conductivity of the flowing gas [242]. Care must be taken to accurately recalibrate individual mass flow controllers for different gasses. The high-pO_2 range can also be extended by heating up the water in the bubbler to increase the amount of water delivered into the system at the same flow rate. As the pH_2O is introduced into the gas via a bubbler, the delivery of pH_2O depends on the saturated vapor pressure of liquid water at the temperature of the bubbler. As anyone with itchy skin from the dry winter air knows, the saturation limit of water changes drastically with temperature. The saturation vapor pressure of a liquid is given via the Clausius-Clapeyron equation, but near room temperature it is common to use the empirically determined Antoine equation:

$$log_{10} p = A - \frac{B}{C + T} \tag{A.7}$$

where p is the vapor pressure, T is temperature, and A, B, and C are material-specific constants. The Antoine equation constants for water are: A=8.07131, B=1730.63, and C=233.426 for T=1 to 100°C. If extending the high-pO_2 range via the above techniques is not enough, then gas mixtures of CO and CO_2 may be used. The ΔG^o of the reaction allows for higher pO_2 control at the cost of using poisonous gas. If this is the only route available, then CO sensors must be placed in the room to protect against CO poisoning. Extending the controllable pO_2 range toward the lower pO_2 values is limited by the mount of possible H_2 flow based on safety concerns and the lowest controllable flow rate for gas through the bubbler. If the H_2O source is turned off lower pO_2

values may be reached using pure forming gas, but the actual pO_2 will no longer be controllable and will depend on the humidity in the gas lines or source gas, leaks in the system, or other unknown sources of humidity. In this scenario the pO_2 must be measured directly.

Appendix B: Seebeck Coefficient Measurements

From a surface level appreciation, Seebeck coefficient measurements are simple. The Seebeck coefficient is simply as a voltage which results from a certain temperature gradient:

$$S = \frac{V}{\Delta T} \tag{A.8}$$

Therefore, in principle all that would be required is a measurement of both the temperature gradient, $\Delta T,$ and the corresponding voltage, V. In practice, the small size of the voltages being measured both across the samples and from the thermocouples leads to large propagated errors. J. Martin et al. from the National Institute of Standards and Technology say it best, "Measurement of the Seebeck coefficient is an exhaustive exercise in low voltage metrology, requiring meticulous attention to the thermal and electric contact interfaces between the probes and the sample, as well as to the instrumentation." [215] Many errors will accumulate in the process of measuring the Seebeck coefficient, although many can be mitigated to a large degree. This section summarizes some of the main error sources and proper measurement of the Seebeck coefficient to minimize these errors. Commercialized Seebeck Coefficient measurement systems will often ignore large sources of error, so one must understand the physics and intricacies of measuring the Seebeck coefficient and avoid treating commercial systems as black boxes.

The four-point-probe measurement arrangement for Seebeck coefficient measurements is shown in Figure A-2.

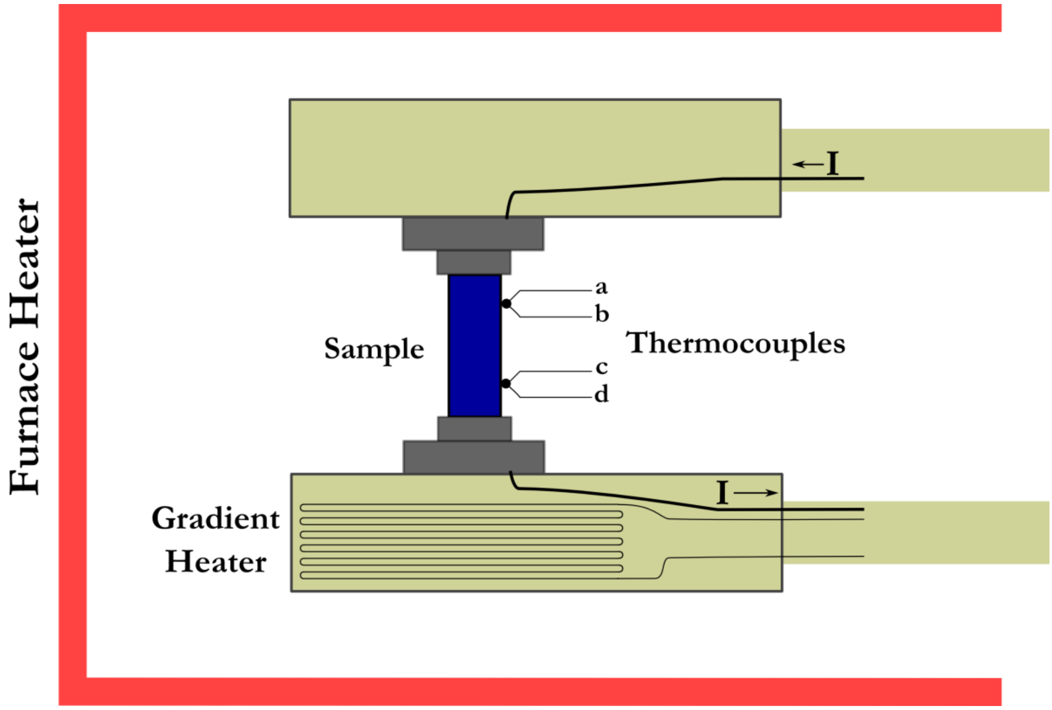

Figure A-2. Schematic of the four point probe Seebeck coefficient measurement technique. The sample is held between block electrodes which supply current for resistivity measurements and two thermocouples are pushed onto the sample surface to measure both the Seebeck voltage and temperature gradient. The background temperature of the furnace is controlled by a global heater, and the temperature gradient on the sample is controlled via a secondary gradient heater. Voltages V_{ac}, V_{ab}, and V_{cd} are necessary for the calculation of the Seebeck coefficient.

From above, an individual measurement of Seebeck voltage (V_{ac}) and temperature gradient (from V_{ab} and V_{cd}) can be used to calculate the Seebeck coefficient via Equation (A.1). The problem with this method is clear when one considers that a finite Seebeck voltage is often measurable when the temperature gradient is measured to be zero. This zero-gradient voltage, or offset voltage, is often on the order of a ~100µV and will be added to the Seebeck voltage, causing a significant error. The offset voltage likely comes from errors in the thermocouple measurements which result in a zero measured temperature gradient but an actual gradient over the sample which is finite. The best strategy is not to minimize this offset voltage but instead to measure the Seebeck voltage at multiple temperature gradients and obtain the Seebeck coefficient from a best fit line of the dV vs dT curve, as shown in Figure A-3.

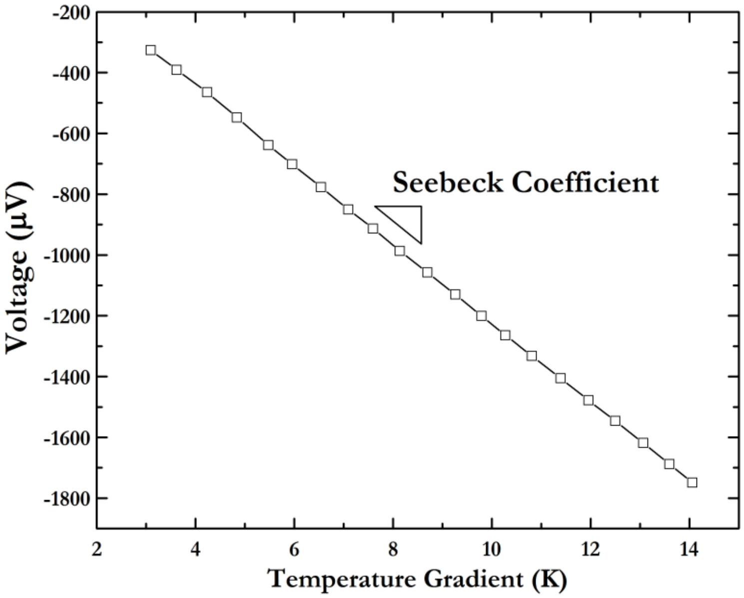

Figure A-3. Temperature difference vs. Seebeck voltage plot. The Seebeck coefficient is given by the slope.

Some commercial systems do not do this, instead opting for measuring a single Seebeck voltage and temperature gradient. The LSR-3 system used in the present performs in this manner, and additional data analysis must be performed to output Seebeck coefficients calculated from dV vs dT curves.

There are two common ways to measure multiple Seebeck voltages and temperature gradients. The first is via a steady state (or DC) approach where an applied temperature gradient is allowed to stabilize for a set dwell time, and then the required voltage measurements are taken (Vac, Vab, and Vcd). This is the most accurate method, but takes a long time as a dV/dT line usually contains ~10-20 points and the entire line must be measured at each temperature gradient, resulting in measurements which take nearly an entire day. An alternative method is quasi-steady state (or qDC) measurements. In a qDC measurement the temperature gradient is steadily ramped at a slow rate and the three required voltages are measured during the ramp. This obviously introduces errors as Vac, Vab, and Vcd are not measured simultaneously (bar the investment of three nanovoltmeters) and therefore error is introduced in the temporal inequivalence. The magnitude of this error has been quantified by J. Martin et al. at NIST (by investing in three nanovoltmeters).[215] For a 2.3 second delay between voltage measurements at 23mK/s heating rate the error in the Seebeck coefficient is ~9.5%. Due to the significant speed up in the measurement, qDC is often the preferred technique, but minimization of this error with quick sequential measurements or heating rates is desirable. Due to software limitations the LSR-3 system used in this thesis cannot measure qDC measurements, but accurate values were obtainable using DC measurements.

As the Seebeck coefficient of the lead wires is finite, the measured Seebeck voltage is the Seebeck voltage of the circuit and includes contributions both from the sample and the lead wires. Knowledge of the Seebeck coefficient of the lead wires as a function of temperature is required to correct for this error. Many Seebeck systems use platinum wiring as the Seebeck coefficient of platinum is well known [243]. The uncorrected Seebeck coefficient of the sample from the circuit is called the ‘relative Seebeck coefficient’ (RSC) while the Seebeck coefficient of the sample alone is the ‘absolute Seebeck coefficient’ (ASC). The absolute Seebeck coefficient of the sample can be obtained by adding the absolute Seebeck coefficient of the wiring, or:

$$ASC_{Sample} = RSC_{Sample} + ASC_{Wiring}$$

Additional errors come from improper measurement of the sample temperature via the thermocouple. Once source of error of this type is due to the thermocouple-sample interface. This interface is important as the thermocouple will measure the temperature not of the sample but of the thermocouple bead, and therefore the thermocouple bead should be in good thermal contact with the sample. A good thermal contact between the thermocouple bead and the sample can be achieved in a couple ways. The atmosphere of the chamber may be filled with a gas which allows for good thermal transfer. Measuring under a vacuum will allow for a larger thermal gradient over the sample, but will increase the thermal contact resistance of the sample-thermocouple interface. This can be minimized by using a large heat capacity, large thermal conductivity gas such as helium. The Seebeck coefficient measured as a function of gas pressure is shown in Figure A-4 from Ref. [215].

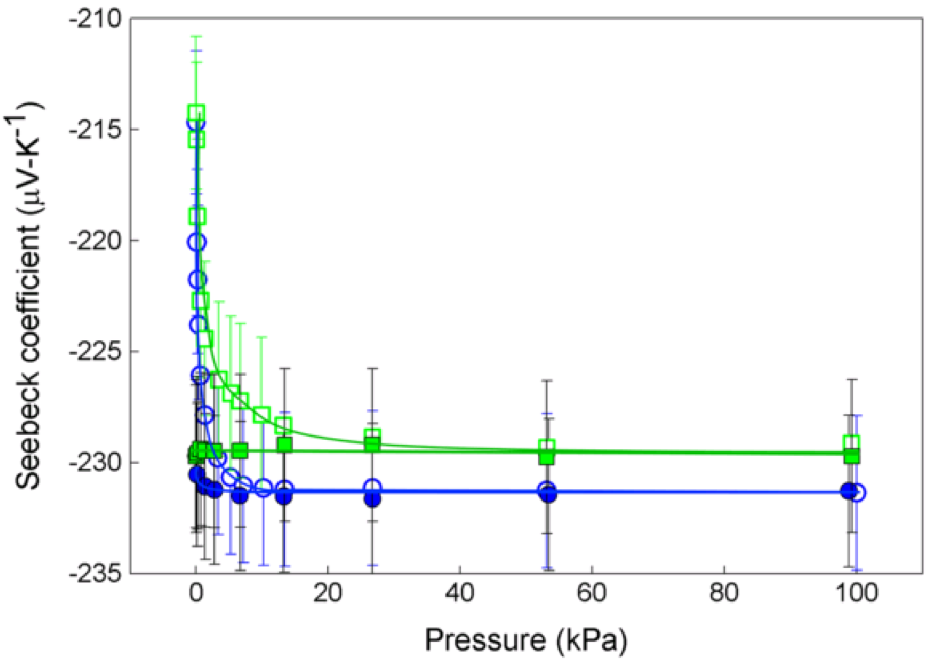

Figure A-4. Seebeck coefficient measured in a Four point probe system under Nitrogen (Green) and Helium (Blue) at different total gas pressures. Filled lines were samples measured with graphite foil placed in between the thermocouple and sample to decrease the thermal barrier resistance. Placing the graphite foil decreased the error from low gas pressures. [215]

Above a gas pressure of 20kPa the Seebeck coefficients level off, but lower gas pressures are not advised. The thermal contact resistance can also be lowered by placing a high thermal conductivity barrier between the thermocouple bead and the sample such as graphite foil. The large thermal conductivity leads to a decreased thermal contact resistance and therefore an increased accuracy in the temperature measurement. Samples measured with this graphite foil barrier are shown in Figure A-4 and result in good thermal contact even at low atmospheric pressures.

Another source of thermocouple error is the ‘cold-finger effect’. This effect is where the thermocouple will pull heat out of the sample and therefore not give an exact measurement of the sample surface. This can be minimized by using thermocouples will small beads, small diameter thermocouple wiring, and low thermal conductivity thermocouple material. This effect cannot be eliminated entirely, however. Additionally, the magnitude of the error increases at high temperatures due to the increased radiative heat transfer to the surroundings [244]. This increases the uncertainty in the four point probe technique at high temperatures at larger temperature gradients. This is shown in Figure A-5 ,which plots the modeled uncertainty for ΔT at different furnace temperatures and temperature gradients.

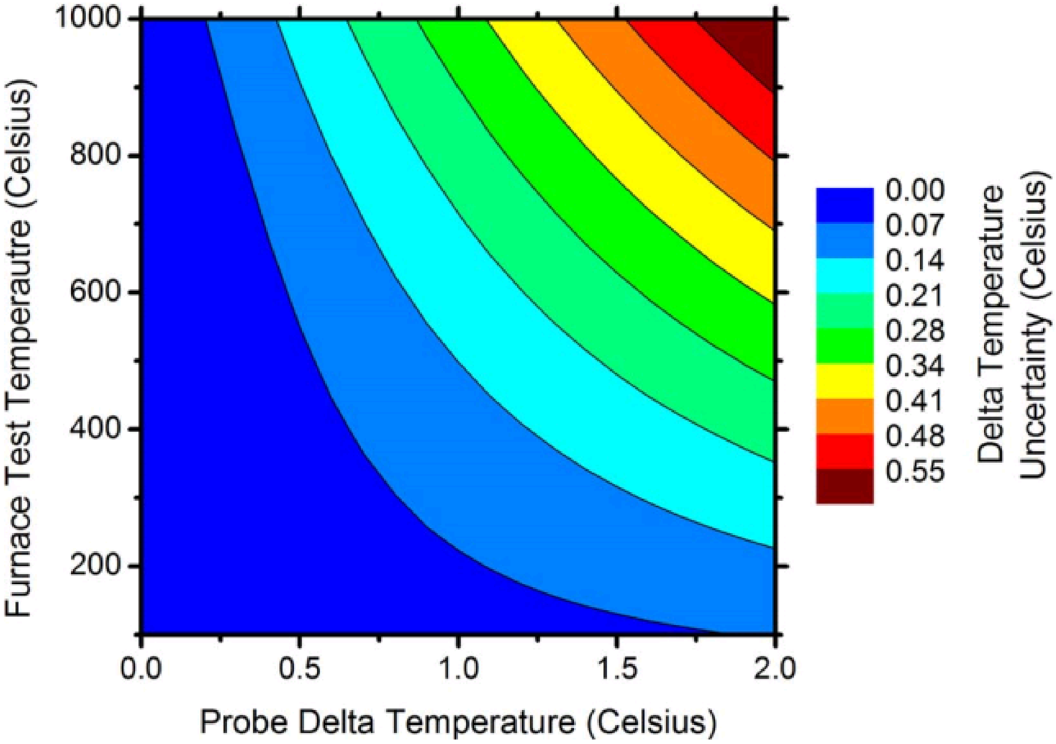

Figure A-5. Values of the ΔT uncertainty at various furnace temperatures and temperature gradients modeled via finite element analysis. The model was performed for a thermal contact conductance of 33,000 W/mK^2 and thermocouple emissivity of 0.7. The large errors at high temperatures and temperature gradients occur primarily due to the cold finger effect. [244]

This increase in the Delta T uncertainty in the upper right hand corner of Figure A-5 can be explained as follows. Under a temperature gradient, both the upper and lower thermocouple are at different temperatures and therefore the cold finger effect will affect the upper and lower thermocouples differently. The hotter thermocouple has a larger cold finger effect due to increased radiative heat transfer to the surroundings at high temperatures. This results in an underestimate of the temperature gradient and an overestimate of the Seebeck coefficient. This has been worked out in detail in reference [244] and the error source is shown to be only ~±1% at room temperature, but can increase to +1.0%/−13.1% at 900°C. At high temperatures the four point probe measurement therefore will tend to overestimate the Seebeck coefficient.

References

[1] D. of Energy, *Quadrennial Technology Review 2015 Direct Thermal Energy Conversion Materials, Devices and Systems*. 2015.

[2] J. Yang and F.R. Stabler, "Automotive Applications of Thermoelectric Materials," *J. Electron. Mater.*, **38** [7] 1245–1251 (2009).

[3] D.J. Anderson, *NASA Radioisotope Power Conversion Technology NRA Overview*. 2005.

[4] F.W. Dynys, M.-H. Berger, and A. Sehirlioglu, "Thermoelectric Properties of Undoped and Doped $(Ti_{0.75}Sn_{0.25})O_2$," *J. Am. Ceram. Soc.*, **95** [2] 619–626 (2012).

[5] T. Tsubota, M. Ohtaki, K. Eguchi, and H. Arai, "Thermoelectric Properties of ZnO Doped with the Group 13 Elements;" pp. 240–243 in *16th Int. Conf. Thermoelectr.* 1997.

[6] D. Berardan, E. Guilmeau, A. Maignan, and B. Raveau, "In_2O_3:Ge, a Promising n-type Thermoelectric Oxide Composite," *Solid State Commun.*, **146** 97–101 (2008).

[7] J.F. Ihlefeld, B.M. Foley, D.A. Scrymgeour, J.R. Michael, B.B. McKenzie, D.L. Medlin, M. Wallace, S. Trolier-McKinstry, *et al.*, "Room-Temperature Voltage Tunable Phonon Thermal Conductivity via Reconfigurable Interfaces in Ferroelectric Thin Films," *Nano Lett.*, **15** 1791–1795 (2015).

[8] M.A. Weilert, M.E. Msall, A.C. Anderson, and J.P. Wolfe, "Phonom Scattering from Ferroelectric Domain Walls: Phonom Imaging in KDP," *Phys. Rev. Lett.*, **71** [5] 735–740 (1993).

[9] S. Lee, R.H.T. Wilke, S. Trolier-McKinstry, S. Zhang, and C.A. Randall, "$Sr_xBa_{1-x}Nb_2O_{6-\delta}$ Ferroelectric-thermoelectrics: Crystal Anisotropy, Conduction Mechanism, and Power Factor," *Appl. Phys. Lett.*, **96** [3] 031910 (2010).

[10] C.L. Choy, W.P. Leung, T.G. Xi, Y. Fei, and C.F. Shao, "Specific Heat and Thermal

Diffusivity of Strontium Barium Niobate ($Sr_{1-x}Ba_xNb_2O_6$) Single Crystals," *J. Appl. Phys.*, **71** [1] 170 (1992).

[11] P. Drude, "Zur Elektronentheorie der Metalle," *Ann. Phys.*, **306** [3] 566 (1900).

[12] N.W. Ashcroft and N.D. Mermin, *Solid State Physics*. Cengage Learning, Saunders, Philadelphia, 1976.

[13] N.W. Ashcroft and N.D. Mermin, "Failures of the Free Electron Model;" pp. 57–63 in *Solid State Phys.* Cengage Learning, Saunders, Philadelphia, 1976.

[14] C. Kittel, "The Nearly Free Electron Model;" pp. 164–167 in *Introd. to Solid State Phys.*, 8th ed. New York, NY, 2004.

[15] P.A. Cox, "The Hubbard Model;" pp. 82–87 in *Transit. Met. Oxides An Introd. to their Electron. Struct. Prop.* Oxford University Press, Oxford, New York, 1992.

[16] J.K. Burdett, *Chemical Bonding in Solids*. Oxford University Press, New York, NY, 1995.

[17] T. Brown, H. LeMay, B. Bursten, C. Murphy, P. Woodward, and M. Stoltzfus, *Chemistry: The Central Science*, 13th ed. Prentice Hall, Bergen County, 2014.

[18] G.K. Wertheim and S. Hüfner, "X-Ray Photoemission Band Structure of Some Transition-Metal Oxides," *Phys. Rev. Lett.*, **28** [16] 1028–1031 (1972).

[19] P.A. Cox, *Transition Metal Oxides: An Introduction to their Electronic Structure and Properties*. Oxford Univeristy Press, Oxford, New York, 1992.

[20] C.J. Ballhausen, *Ligand Field Theory*. McGrow Hill, New York, 1962.

[21] P.W. Anderson, "Absence of Diffusion in Certain Random Lattices," *Phys. Rev.*, **109** [5] 1492–1505 (1958).

[22] D.S. Wiersma, P. Bartolini, A. Lagendijk, and R. Righini, "Localization of Light in a Disordered Medium," *Nature*, **390** 671–673 (1997).

[23] J. Billy, V. Josse, Z. Zuo, A. Bernard, B. Hambrecht, P. Lugan, D. Clément, L. Sanchez-Palencia, *et al.*, "Direct Observation of Anderson Localization of Matter Waves in a

Controlled Disorder," *Nature*, **453** 891–894 (2008).

24 H. Kamimura and H. Aoki, *The Physics of Interacting Electrons in Disordred Systems*. Oxford University Press, New York, 1989.

25 V.F. Gantmakher, "Metal-Insulator Transitions;" pp. 74–100 in *Electrons Disord. Solids*. Oxford Univeristy Press, New York, NY, 2005.

26 N.F. Mott and E.A. Davis, "Theory of Electrons in a Non-Crystalline Medium;" pp. 7–62 in *Electron. Process. Non-Crystalline Mater.*, 2nd ed. Oxford Univeristy Press, New York, NY, 1979.

27 P.A. Cox, "Anderson Localization;" pp. 91–92 in *Transit. Met. Oxides An Introd. to their Electron. Struct. Prop.* Oxford University Press, Oxford, New York, 1992.

28 N.F. Mott and E.A. Davis, "The Fermi Glass and the Anderson Transition;" pp. 98–160 in *Electron. Process. Non-Crystalline Mater.*, 2nd ed. 1979.

29 N.F. Mott and E.A. Davis, "Non-Crystalline Semiconductors;" pp. 199–314 in *Electron. Process. Non-crystalline Mater.*, 2nd ed. Oxford Univeristy Press, New York, NY, 1979.

30 C. Kittel, *Introduction to Solid State Physics*, 8th ed. Wiley, New York, NY, 2004.

31 I.G. Austin and N.F. Mott, "Polarons in Crystalline and Non-Crystalline Materials," *Adv. Phys.*, **18** [71] 41–102 (1969).

32 S. Lee, J.A. Bock, S. Trolier-McKinstry, and C.A. Randall, "Ferroelectric-Thermoelectricity and Mott Transition of Ferroelectric Oxides with High Electronic Conductivity," *J. Eur. Ceram. Soc.*, **32** [16] 3971–3988 (2012).

33 D. Nuzhnyy, J. Petzelt, M. Savinov, T. Ostapchuk, V. Bovtun, M. Kempa, J. Hlinka, V. Buscaglia, *et al.*, "Broadband Dielectric Response of Ba(Zr,Ti)O_3 Ceramics: From Incipient via Relaxor and Diffuse up to Classical Ferroelectric Behavior," *Phys. Rev. B - Condens. Matter Mater. Phys.*, **86** [1] 1–9 (2012).

34 O.K. Andersen and O. Jepsen, "Explicit, First-Principles Tight-Binding Theory," *Phys.*

Rev. Lett., **53** [27] 2571–2574 (1984).

[35] V.F. Gantmakher, *Electrons and Disorder in Solids*. Oxford Science Publications, New York, 2005.

[36] L.R. Friedman and D.P. Tunstall, "The Metal Non-Metal Transiiton in Disordered Systems," *Scottish Univ. Summer Sch. Phys. Publ.*, (1974).

[37] P.P. Edwards and M.J. Sienko, "Universality Aspects of the Metal-Nonmetal Transition in Condensed Media," *Phys. Rev. B*, **17** [6] 2575–2581 (1978).

[38] E. Salje and B. Guttler, "Anderson Transition and Intermediate Polaron Formaiton in WO_{3-x} Transport Properties and Optical Absorption," *Philos. Mag. Part B*, **50** [5] 607–620 (1984).

[39] W. Wunderlich, H. Ohta, and K. Koumoto, "Enhanced Effective Mass in Doped $SrTiO_3$ and Related Perovskites," *Phys. B Condens. Matter*, **404** 2202–2212 (2009).

[40] C. Lee, J. Destry, and J.L. Brebner, "Optical Absorption and Transport in Semiconducting $SrTiO_3$," *Phys. Rev. B*, **11** [6] 2299–2310 (1975).

[41] P.P. Edwards, T. V Ramakrishnan, and C.N.R. Rao, "The Metal-Nonmetal Transition: A Global Perspective," *J. Phys. Chem.*, **99** 5228–5239 (1995).

[42] E. Buixaderas, M. Savinov, M. Kempa, S. Veljko, S. Kamba, J. Petzelt, R. Pankrath, and S. Kapphan, "Infrared and Dielectric Spectroscopy of the Relaxor Ferroelectric $Sr_{0.61}Ba_{0.39}Nb_2O_6$," *J. Phys. Condens. Matter*, **17** [4] 653–666 (2005).

[43] D. Emin, "Strong Coupling: Self Trapping;" pp. 21–41 in *Polarons*. Oxford University Press, Cambridge, NY, 2013.

[44] D. Emin, *Polarons*. Cambridge University Press, Cambridge, UK, 2013.

[45] D. Emin, "Small-Polaron Transport;" pp. 95–123 in *Polarons*. Cambridge Univeristy Press, Cambridge, UK, 2013.

[46] P.A. Cox, "Transport Properties;" pp. 160–169 in *Transit. Met. Oxides An Introd. to their*

Electron. Struct. Prop. Oxford University Press, Oxford, New York, 1992.

47 D. Emin, "Phonon-Assisted Jump Rate in Noncrystalline Solids," *Phys. Rev. Lett.*, **32** [6] 303–307 (1974).

48 N.F. Mott and E.A. Davis, "Hopping and Variable-Tange Hopping;" pp. 32–37 in *Electronc Process. Non-Crystalline Mater.*, Second. Edited by D.H.W. W. Marshall. Oxford University Press, New York, NY, 2012.

49 H. Kamimura and H. Aoki, "Hopping Conduction and Related Phenomena;" pp. 121–147 in *Phys. Interact. Electrons Disord. Syst.* Oxford University Press, New York, NY, 1989.

50 N.F. Mott, "Conduction in Non-Crystalline Materials: III. Localized States in a Pseudogap and Near Extremities of Conduciton and Valence Bands," *Philos. Mag.*, **10** [160] 835–852 (1969).

51 F. Reif, *Fundamentals of Statistical and Thermal Physics*, 1st ed. McGraw-Hill Higher Education, 1965.

52 C. Kittel, "Free Electron Fermi Gas;" pp. 133–157 in *Introd. to Solid State Phys.*, 8th ed. Edited by S. Johnson, P. McFadden and M. Batey. John Wiley & Sons, Inc., New York, NY, 2005.

53 C. Kittel, "Thermal Conductivity of Metals;" pp. 156–157 in *Introd. to Solid State Phys.*, 8th ed. Edited by S. Johnson, P. McFadden and M. Batey. John Wiley & Sons, Inc., New York, NY, 2005.

54 C. Kittel, "Electrical Conductivity and Ohm's Law;" pp. 147–148 in *Introd. to Solid State Phys.*, 8th ed. Edited by S. Johnson, P. McFadden and M. Batey. John Wiley & Sons, Inc., New York, 2005.

55 J. Yang, "Electronic Thermal Conduction;" pp. 3–9 in *Therm. Conduct. Theory, Prop. Appl.* Edited by T.M. Tritt. Plenum Publishers, New York, NY, 2004.

56 T.M. Tritt, *Thermal Conductivity: Theory, Properties, and Applications*. Kluwer

Academic/Plenum publishers, New York, NY, 2004.

57 F.J. Blatt, P.A. Schroeder, C.L. Foiles, and D. Greig, *Thermoelectric Power of Metals*. Plenum Press, New York, NY, 1976.

58 C. Kittel, “Two Atoms Per Primative Basis;” pp. 95–99 in *Introd. to Solid State Phys.*, 8th ed. Edited by S. Johnson, P. McFadden and M. Batey. John Wiley & Sons, Inc., New York, NY, 2005.

59 C. Kittel, “Vibrations of Crystals with Monatomic Basis;” pp. 91–95 in *Introd. to Solid State Phys.*, 8th ed. Edited by S. Johnson, P. McFadden and M. Batey. John Wiley & Sons, Inc., New York, NY, 2005.

60 M. Christensen, A.B. Abrahamsen, N.B. Christensen, F. Juranyi, N.H. Andersen, K. Lefmann, J. Andreasson, C.R.H. Bahl, *et al.*, “Avoided Crossing of Rattler Modes in Thermoelectric Materials,” *Nat. Mater.*, **7** [10] 811–815 (2008).

61 C. H. Lee, I. Hase, H. Sugawara, H. Yoshizawa, and H. Sato, “Low-Lying Optical Phonon Modes in the Filled Skutterudite $CeRu_4Sb_{12}$,” *J. Phys. Soc. Japan*, **75** [12] 123602 (2006).

62 P.D. Maycock, “Thermal Conductivity of Silicon, Germanium, III–V Compounds and III–V Alloys,” *Solid. State. Electron.*, **10** 161–168 (1967).

63 E.S. Toberer, L.L. Baranowski, and C. Dames, “Advances in Thermal Conductivity,” *Annu. Rev. Mater. Res.*, **42** 179–209 (2012).

64 G.A. Slack, “The Thermal Conductivity of Nonmetallic Crystals;” pp. 1–77 in *Solid State Physics, Vol 34*. Academic Press, New York, NY, 1979.

65 D.R. Gaskell, *Introduction to the Thermodynamics of Materials*, 4th ed. Taylor & Francis Group, LLC, New York, NY, 2003.

66 C. Kittel, “Phonon Heat Capacity;” pp. 107–121 in *Introd. to Solid State Phys.*, 8th ed. Edited by S. Johnson, P. McFadden and M. Batey. John Wiley & Sons, Inc., New York, NY, 2005.

[67] W.D. Kingery, H.K. Bowen, and D.R. Uhlmann, “Heat Capacity;” pp. 586–589 in *Introd. to Ceram.*, Second. Edited by E. Burke, B. Chalmers and J. Krumhansl. John Wiley & Sons, Inc., 1960.

[68] S.S. Todd and R.E. Lorenson, “Heat Capacities at Low Temperatures and Entropies at 298.16K of Metatitanates of Barium and Strontium,” *J. Am. Chem. Soc.*, **74** [8] 2043–2045 (1952).

[69] W. Cochran, *The Dynamics of Atoms in Crystals*. Crane Russak & Co., 1973.

[70] A. Kumar, U.C. Naithani, and B.S. Semwal, “Sound Velocity Change in $Ba_xSr_{1-x}TiO_3$ Perovskites,” **42** 18–24 (2004).

[71] M. Tachibana, T. Kolodiazhnyi, and E. Takayama-Muromachi, “Thermal Conductivity of Perovskite Ferroelectrics,” *Appl. Phys. Lett.*, **93** [9] 092902 (2008).

[72] R.E. Newnham, “Acoustic Waves I + II;” pp. 249–270 in *Prop. Mater. Anisotropy, Symmetry, Struct.* Oxford University Press, New York, 2005.

[73] M.E. Manley, J.W. Lynn, D.L. Abernathy, E.D. Specht, O. Delaire, A.R. Bishop, R. Sahul, and J.D. Budai, “Phonon Localization Drives Polar Nanoregions in a Relaxor Ferroelectric,” *Nat. Commun.*, **5** 3683 (2014).

[74] M.E. Manley, “Impact of Intrinsic Localized Modes of Atomic Motion on Materials Properties,” *Acta Mater.*, **58** [8] 2926–2935 (2010).

[75] M.E. Manley, “Intrinsic Localized Lattice Modes and Thermal Transport: Potential Application in a Thermal Rectifier,” *Mater. Res. Soc. Proc.*, 1172–T09–02 (2009).

[76] R.E. Cohen, “Origin of Ferroelectricity in Perovskite Oxides,” *Nature*, **358** 136–138 (1992).

[77] M. Yamamoto, H. Ohta, and K. Koumoto, “Thermoelectric Phase Diagram in a $CaTiO_3$-$SrTiO_3$-$BaTiO_3$ System,” *Appl. Phys. Lett.*, **90** [7] 072101 (2007).

[78] “An American National Standard IEEE Standard Definitions of Terms Associated With

Ferroelectric and Related Materials," *IEEE Trans. Ultrason. Ferroelectr. Freq. Control,* **50** [12] 1–32 (2003).

79 J. Fousek and V. Janovec, "The Orientation of Domain Walls in Twinned Ferroelectric Crystals," *J. Appl. Phys.,* **40** 135 (1969).

80 T. Sluka, A.K. Tagantsev, D. Damjanovic, M. Gureev, and N. Setter, "Enhanced Electromechanical Response of Ferroelectrics Due to Charged Domain Walls," *Nat. Commun.*, **3** 748 (2012).

81 T. Sluka, A.K. Tagantsev, P. Bednyakov, and N. Setter, "Free-Electron Gas at Charged Domain Walls in Insulating $BaTiO_3$," *Nat. Commun.,* **4** 1–6 (2013).

82 L.E. Cross, "Relaxor Ferroelectrics," *Ferroelectrics,* **76** 241–267 (1987).

83 A.A. Bokov and Z.-G. Ye, "Recent Progress in Relaxor Ferroelectrics with Perovskite Structure," *J. Mater. Sci.,* **41** 31–52 (2006).

84 A. Bussmann-Holder, A.R. Bishop, and T. Egami, "Relaxor Ferroelectrics and Intrinsic Inhomogeneity," *Europhys. Lett.*, **71** [2] 249–255 (2005).

85 R.R. Heikes and R.W. Ure, *Thermoelectricity: Science and Engineering*. Interscience Publishers, New York, NY, 1961.

86 C. Kittel, "Thermoelectric Effects;" pp. 214–215 in *Introd. to Solid State Phys.,* 8th ed. Edited by S. Johnson, P. McFadden and R. Smith. John Wiley & Sons, Inc., New York, NY, 2005.

87 D.M. Rowe, "Thermoelectric and Thermomagnetic Effects;" pp. 1–2 in *Thermoelectr. Handb. Macro to Nano*. Edited by D.M. Rowe. Taylor & Francis Group, LLC, Boca Raton, FL, 2006.

88 H.J. Goldsmid, "The Thermoelectric and Related Effects;" pp. 1–6 in *Introd. to Thermoelectr.* Edited by R. Hull, J. Parisis, R.M. Osgood and W. Hans. Springer - Verlage Berlin Heidelberg, Berlin, 2010.

89 G.S. Nolas, J. Sharp, and H.J. Goldsmid, “Peltier Cooling and Thermoelectric Figure of Merit;” pp. 1–13 in *Thermoelectr. Basic Princ. New Mater. Dev.* Edited by R. Hull, R.M. Osgood, H. Sakaki and A. Zunger. 2001.

90 D.M. Rowe, “Thermoelectric Generation and the Figure-of-Merit;” pp. 1–3 in *Thermoelectr. Handb. Macro to Nano*. Edited by D.M. Rowe. Taylor & Francis Group, LLC, Boca Raton, FL, 2006.

91 G.J. Snyder and E.S. Toberer, “Complex Thermoelectric Materials.,” *Nat. Mater.*, **7** 105–114 (2008).

92 A.F. Ioffe, *Semiconductor Thermoelements and Thermoelectric Cooling*. Infosearch, London, UK, 1957.

93 A. Bulusu and D.G. Walker, “Review of Electronic Transport Models for Thermoelectric Materials,” *Superlattices Microstruct.*, **44** 1–36 (2008).

94 N.F. Mott and E.A. Davis, “Thermopower;” pp. 52–56 in *Electron. Process. Non-Crystalline Mater.*, Second. Edited by W. Marshall and D.H. Wilkinson. Claredon Press, Oxford, UK, 1979.

95 M. Jonson and G.D. Mahan, “Mott’s Formula for the Thermopower and the Wiedemann-Franz Law,” *Phys. Rev. B*, **21** [10] 4223–9 (1980).

96 Y. Pei, H. Wang, and G.J. Snyder, “Band Engineering of Thermoelectric Materials,” *Adv. Mater.*, **24** 6125–6135 (2012).

97 R.R. Heikes and R.W. Ure, “Distribution Treatment of Transport Properties;” pp. 47–53 in *Thermoelectr. Sci. Eng.* Interscience Publishers, New York, NY, 1961.

98 C. Kittel, “Semiconducting Crystals;” pp. 186–217 in *Introd. to Solid State Phys.*, 8th ed. Edited by S. Johnson, P. McFadden and M. Batey. John Wiley & Sons, Inc., New York, NY, 2005.

99 G.S. Nolas and H.J. Goldsmid, “Multiband Effects;” pp. 42–44 in *Thermoelectr. Basic*

Princ. New Mater. Dev. Edited by A. Zunger, R. Hull, R.M. Osgood and H. Sakaki. Springer-Verlag Berlin Heidelberg, Berlin, 2001.

[100] H.J. Goldsmid, "Thermoelectric Properties of Metals and Semiconductors;" pp. 23–41 in *Introd. to Thermoelectr.* Edited by R. Hull, J. Parisi, R.M.J. Osgood and H. Warlimont. Springer-Verlag Berlin Heidelberg, Berlin, 2010.

[101] H.J. Goldsmid, "Extension of The Temperature Range;" pp. 93–95 in *Introd. to Thermoelectr.* Edited by R. Hull, J. Parisi, R.M. Osgood and H. Warlimont. Springer - Verlage Berlin Heidelberg, Berlin, 2010.

[102] H.J. Goldsmid, "The Electrical Conductivity and Thermoelectric Power of Bismuth Telluride," *Proc. Phys. Soc.*, **71** 633–646 (1958).

[103] D. Emin, "The Seebeck Coefficient;" pp. 5–2 in *Thermoelectr. Handb. Macro to Nano*. Edited by D.M. Rowe. Taylor & Francis Group, LLC, Boca Raton, FL, 2006.

[104] S. Hébert, S. Lambert, D. Pelloquin, and A. Maignan, "Large Thermopower in a Metallic Cobaltite: The Layered Tl-Sr-Co-O Misfit," *Phys. Rev. B*, **64** [17] 172101 (2001).

[105] A. Maignan, S. Hébert, L. Pi, D. Pelloquin, C. Martin, C. Michel, M. Hervieu, and B. Raveau, "Perovskite Manganites and Layered Cobaltites: Potential Materials for Thermoelectric Applications," *Cryst. Eng.*, **5** 365–382 (2003).

[106] K. Berggold, M. Kriener, C. Zobel, A. Reichl, M. Reuther, R. Müller, A. Freimuth, and T. Lorenz, "Thermal Conductivity, Thermopower, and Figure of Merit of $La_{1-x}Sr_xCoO_3$," *Phys. Rev. B*, **72** [15] 155116 (2005).

[107] J.-P. Doumerc, "Thermoelectric Power for Carriers in Localized States: A Generalization of Heikes and Chaikin-Beni Formulae," *J. Solid State Chem.*, **110** 419–420 (1994).

[108] W. Koshibae, K. Tsutsui, and S. Maekawa, "Thermopower in Cobalt Oxides," *Phys. Rev. B*, **62** [11] 6869–6872 (2000).

[109] K. Fujita, T. Mochida, and K. Nakamura, "High-Temperature Thermoelectric Properties

of $Na_xCoO_{2-\delta}$ Single Crystals," *Jpn. J. Appl. Phys.*, **40** 4644–4647 (2001).

[110] H. Muta, K. Kurosaki, and S. Yamanaka, "Thermoelectric Properties of Rare Earth Doped $SrTiO_3$," *J. Alloys Compd.*, **350** 292–295 (2003).

[111] K. Takahata, Y. Iguchi, D. Tanaka, and T. Itoh, "Low Thermal Conductivity of the Layered Oxide $(Na,Ca)Co_2O_4$: Another Example of a Phonon Glass and an Electron Crystal," *Phys. Rev. B.*, **61** [19] 12551–55 (2000).

[112] T. Tsubota, M. Ohtaki, K. Eguchi, and H. Arai, "Thermoelectric Properties of Al-Doped ZnO as a Promising Oxide Material for High-Temperature Thermoelectric Conversion," *J. Mater. Chem.*, **7** [1] 85–90 (1997).

[113] M. Shikano and R. Funahashi, "Electrical and Thermal Properties of Single-Crystalline $(Ca2CoO3)_{0.7}CoO_2$ with a $Ca_3Co_4O_9$ Structure," *Appl. Phys. Lett.*, **82** [12] 1851–1854 (2003).

[114] M. Ohtaki, K. Araki, and K. Yamamoto, "High Thermoelectric Performance of Dually Doped ZnO Ceramics," *J. Electron. Mater.*, **38** [7] 1234–1238 (2009).

[115] G. Xu, R. Funahashi, M. Shikano, I. Matsubara, and Y. Zhou, "Thermoelectric Properties of the Bi- and Na-Substituted $Ca_3Co_4O_9$," *Appl. Phys. Lett.*, **80** [20] 3760 (2002).

[116] J. Son, P. Moetakef, B. Jalan, O. Bierwagen, N.J. Wright, R. Engel-Herbert, and S. Stemmer, "Epitaxial $SrTiO_3$ Films with Electron Mobilities Exceeding $30{,}000 cm^2V^{-1} s^{-1}$," *Nat. Mater.*, **9** 482–484 (2010).

[117] S. Ohta, T. Nomura, H. Ohta, and K. Koumoto, "High-Temperature Carrier Transport and Thermoelectric Properties of Heavily La- Or Nb-Doped $SrTiO_3$ Single Crystals," *J. Appl. Phys.*, **97** 034106 (2005).

[118] D.C. Look, "Recent Advances in ZnO Materials and Devices," *Mater. Sci. Eng. B,* **80** 383–387 (2001).

[119] M. Ohtaki, T. Tsubota, and K. Eguchi, "Thermoelectric Properties of Oxide Solid

Solutions Based on Al-Doped ZnO;" pp. 610–613 in *Seventeenth Int. Conf. Thermoelectr.* 1998.

120 P.B. Jamieson, S.C. Abrahams, and J.L. Bernstein, "Ferroelectric Tungsten Bronze-Type Crystal Structures. I. Barium Strontium Niobate $Ba_{0.27}Sr_{0.75}Nb_2O_{5.78}$," *J. Chem. Phys.,* **48** [11] 5048–57 (1968).

121 M.P. Trubelja, E. Ryba, and D.K. Smith, "A Study of Positional Disorder in Strontium Barium Niobate," *J. Mater. Sci.,* **31** 1435–1443 (1996).

122 H. Fan, L. Zhang, and X. Yao, "Relaxation Characteristics of Strontium Barium Niobate Ferroelectric Ceramics," *J. Mater. Sci.,* **33** 895–900 (1998).

123 W.H. Huang, D. Viehland, and R.R. Neurgaonkar, "Anisotropic Glasslike Characteristics of Strontium Barium Niobate Relaxors," *J. Appl. Phys.,* **76** [1] 490–496 (1994).

124 C.J. Huang, K. Li, X.Q. Liu, X.L. Zhu, and X.M. Chen, "Effects of A1/A2-Sites Occupancy upon Ferroelectric Transition in $Sr_xBa_{1-x}Nb_2O_6$ Tungsten Bronze Ceramics," *J. Am. Ceram. Soc.,* **97** [2] 507–512 (2014).

125 M.E. Lines and A.M. Glass, "Semiconducting Ferroelectrics;" pp. 503–524 in *Princ. Appl. Ferroelectr. Relat. Mater.* Oxford University Press, Oxford, New York, 1977.

126 V.M. Fridkin, *Ferroelectric Semiconductors*. Consultants Bureau, New York, NY, 1980.

127 W. Heywang, "Semiconducting Barium Titanate," *J. Mater. Sci.,* **6** 1214–1224 (1971).

128 J. Seidel, L.W. Martin, Q. He, Q. Zhan, Y.-H. Chu, A. Rother, M.E. Hawkridge, P. Maksymovych, *et al.*, "Conduction at Domain Walls in Oxide Multiferroics.," *Nat. Mater.,* **8** 229–234 (2009).

129 V.P. Mineev and Y. Yoshioka, "Optical Activity of Noncentrosymmetric Metals," *Phys. Rev. B,* **81** 094525 (2010).

130 V.M. Edelstein, "Features of Light Reflection Off Metals with Destroyed Mirror Symmetry," *Phys. Rev. B,* **83** 113109 (2011).

[131] P.W. Anderson and E.I. Blount, “Symmetry Considerations on Martensitic Transformation: ‘Ferroelectric’ Metals?,” *Phys. Rev. Lett.*, **14** [7] 217–219 (1965).

[132] J.W. Bennett, K.F. Garrity, K.M. Rabe, and D. Vanderbilt, “Hexagonal ABC Semiconductors as Ferroelectrics,” *Phys. Rev. Lett.*, **109** 167602 (2012).

[133] I.A. Sergienko, V. Keppens, M. McGuire, R. Jin, J. He, S.H. Curnoe, B.C. Sales, P. Blaha, *et al.*, “Metallic ‘Ferroelectricity’ in the Pyrochlore $Cd_2Re_2O_7$,” *Phys. Rev. Lett.*, **92** [6] 065501 (2004).

[134] Y. Shi, Y. Guo, X. Wang, A.J. Princep, D. Khalyavin, P. Manuel, Y. Michiue, A. Sato, *et al.*, “A Ferroelectric-Like Structural Transition in a Metal,” *Nat. Mater.*, **12** 1024–27 (2013).

[135] G. Giovannetti and M. Capone, “Dual Nature of the Ferroelectric and Metallic State in LiOsO3,” *Phys. Rev. B*, **90** 195113 (2014).

[136] D. Puggioni and J.M. Rondinelli, “Designing a Robustly Metallic Noncenstrosymmetric Ruthenate Oxide with Large Thermopower Anisotropy.,” *Nat. Commun.*, **5** 1–9 (2014).

[137] S. Podlozhenov, H.A. Graetsch, J. Schneider, M. Ulex, M. Wöhlecke, and K. Betzler, “Structure of Strontium Barium Niobate $Sr_xBa_{1-x}Nb_2O_6$ (SBN) in the Composition Range $0.32 \leq x \leq 0.82$,” *Acta Crystallogr. Sect. B Struct. Sci.*, **62** 960–965 (2006).

[138] H. Ning, H. Yan, and M.J. Reece, “Piezoelectric Strontium Niobate and Calcium Niobate Ceramics with Super-High Curie Points,” *J. Am. Ceram. Soc.*, **93** [5] 1409–1413 (2010).

[139] E.N. Bunting, G.R. Shelton, and A.S. Creamer, “Properties of Barium-Strontium Titanate Dielectrics,” *J. Natl. Bur. Stand.*, **38** 337–349 (1947).

[140] H.-Y. Lee and R. Freer, “Abnormal Grain Growth and Liquid-Phase Sintering in $Sr_{0.6}Ba_{0.4}Nb_2O_6$ (SBN40) Ceramics,” *J. Mater. Sci.*, **33** [7] 1703–1708 (1998).

[141] S. Lee, G. Yang, R.H.T. Wilke, S. Trolier-McKinstry, and C.A. Randall, “Thermopower in Highly Reduced n-type Ferroelectric and Related Perovskite Oxides and the Role of

Heterogeneous Nonstoichiometry," *Phys. Rev. B*, **79** [13] 134110 (2009).

142 J.A. Bock, S. Trolier-McKinstry, G.D. Mahan, and C.A. Randall, "Polarization-Based Perturbations to Thermopower and Electronic Conductivity in Highly Conductive Tungsten Bronze Structured (Sr,Ba)$Nb_2O_{6-\delta}$," *Phys. Rev. B*, **90** [11] 115106 (2014).

143 A. Ziębińska, D. Rytz, K. Szot, M. Górny, and K. Roleder, "Birefringence Above T_C in Single Crystals of Barium Titanate," *J. Phys. Condens. Matter*, **20** 142202 (2008).

144 J.-H. Ko, T.H. Kim, K. Roleder, D. Rytz, and S. Kojima, "Precursor Dynamics in the Ferroelectric Phase Transition of Barium Titanate Single Crystals Studied by Brillouin Light Scattering," *Phys. Rev. B*, **84** 094123 (2011).

145 D.F. Rushman and M.A. Strivens, "The Permittivity of Polycrystals of the Perovskite Type," *Trans. Faraday Soc.*, **42** A231–A238 (1946).

146 S. Kisaka, S. Ikegami, and H. Sasaki, "Dielectric Properties of Mixed Crystals of Barium-Strontium Titanate," *J. Phys. Soc. Japan*, **14** [12] 1680–1685 (1959).

147 I.-K. Jeong, S. Lee, S.-Y. Jeong, C.J. Won, N. Hur, and A. Llobet, "Structural Evolution Across the Insulator-Metal Transition in Oxygen-Deficient $BaTiO_{3-\delta}$ Studied Using Neutron Total Scattering and Rietveld Analysis," *Phys. Rev. B*, **84** [6] 064125 (2011).

148 I. Levin, V. Krayzman, and J.C. Woicik, "Local Structure in Perovskite (Ba, Sr)TiO_3: Reverse Monte Carlo Refinements From Multiple Measurement Techniques," *Phys. Rev. B*, **89** [2] 024106 (2014).

149 A.S. Bhalla, R. Guo, L.E. Cross, G. Burns, F.H. Dacol, and R.R. Neurgaonkar, "Measurements of Strain and the Optical Indicies in the Ferroelectric $Ba_{0.4}Sr_{0.6}Nb_2O_6$: Polarization Effects," *Phys. Rev. B*, **36** [4] 2030–2035 (1987).

150 C.S. Pandey, J. Schreuer, M. Burianek, and M. Mühlberg, "Relaxor Behavior of $Ca_xBa_{1-x}Nb_2O_6$ (0.18<x<0.35) Tuned by Ca/Ba Ratio and Investigated by Resonant Ultrasound Spectrocopy," *Phys. Rev. B*, **87** [9] 094101 (2013).

[151] K. Uchino, *Ferroelectric Devices*. Marcel Dekker, Inc., New York, NY, 2000.

[152] P. Muralt, R.G. Polcawich, and S. Trolier-McKinstry, "Piezoelectric Thin Films for Sensors, Actuators, and Energy Harvesting," *MRS Bull.*, **34** 658–664 (2009).

[153] N. Setter, D. Damjanovic, L. Eng, G. Fox, S. Gevorgian, S. Hong, A. Kingon, H. Kohlstedt, *et al.*, "Ferroelectric Thin Films: Review of Materials, Properties, and Applications," *J. Appl. Phys.*, **100** [5] 051606 (2006).

[154] R. Thomas, J.F. Scott, D.N. Bose, and R.S. Katiyar, "Multiferroic Thin-Film Integration onto Semiconductor Devices.," *J. Phys. Condens. Matter*, **22** [42] 423201 (2010).

[155] R.W. Whatmore, "Pyroelectric Devices and Materials," *Reports Prog. Phys.*, **49** 1335–1386 (1986).

[156] R.E. Jones, P.D. Maniar, R. Moazzami, P. Zurcher, J.Z. Witowski, Y.T. Lii, P. Chu, and S.J. Gillespie, "Ferroelectric Non-Volatile Memories for Low-Voltage, Low-Power Applications," *Thin Solid Films*, **270** 584–588 (1995).

[157] G. V. Lewis, C.R.A. Catlow, and R.E.W. Casselton, "PTCR Effect in $BaTiO_3$," *J. Am. Ceram. Soc.*, **68** [10] 555–558 (1985).

[158] S.Y. Yang, J. Seidel, S.J. Byrnes, P. Shafer, C.-H. Yang, M.D. Rossell, P. Yu, Y.-H. Chu, *et al.*, "Above-Bandgap Voltages from Ferroelectric Photovoltaic Devices," *Nat. Nanotechnol.*, **5** [2] 143–147 (2010).

[159] H. Huang, "Solar Energy: Ferroelectric Photovoltaics," *Nat. Photonics*, **4** [3] 134–135 (2010).

[160] V.M. Fridkin and B.N. Popov, "Anomalous Photovoltaic Effect in Ferroelectrics," *Sov. Phys. Usp.*, **21** [12] 991 (1978).

[161] S. Lee, S. Dursun, C. Duran, and C.A. Randall, "Thermoelectric Power Factor Enhancement of Textured Ferroelectric $Sr_xBa_{1-x}Nb_2O_{6-\delta}$ Ceramics," *J. Mater. Res.*, **26** [1] 26–30 (2011).

162 R.K. Vasudevan, W. Wu, J.R. Guest, A.P. Baddorf, A.N. Morozovska, E.A. Eliseev, N. Balke, V. Nagarajan, *et al.*, “Domain Wall Conduction and Polarization-Mediated Transport in Ferroelectrics,” *Adv. Funct. Mater.*, **23** 2592–2616 (2013).

163 M. Schröder, A. Haußmann, A. Thiessen, E. Soergel, T. Woike, and L.M. Eng, “Conducting Domain Walls in Lithium Niobate Single Crystals,” *Adv. Funct. Mater.*, **22** 3936–3944 (2012).

164 J. Guyonnet, I. Gaponenko, S. Gariglio, and P. Paruch, “Conduction at Domain Walls in Insulating $Pb(Zr_{0.2}Ti_{0.8})O_3$ Thin Films,” *Adv. Mater.*, **23** 5377–5382 (2011).

165 T. Kolodiazhnyi, M. Tachibana, H. Kawaji, J. Hwang, and E. Takayama-Muromachi, “Persistence of Ferroelectricity in $BaTiO_3$ through the Insulator-Metal Transition,” *Phys. Rev. Lett.*, **104** [14] 147602 (2010).

166 T. Kolodiazhnyi, “Insulator-Metal Transition and Anomalous Sign Reversal of the Dominant Charge Carriers in Perovskite $BaTiO_{3-\delta}$,” *Phys. Rev. B*, **78** [4] 045107 (2008).

167 B.T. Matthias, “Ferroelectricity,” *J. Appl. Phys.*, **38** [3] 928–930 (1967).

168 P.E. Hopkins, C. Adamo, L. Ye, B.D. Huey, S.R. Lee, D.G. Schlom, and J.F. Ihlefeld, “Effects of Coherent Ferroelastic Domain Walls on the Thermal Conductivity and Kapitza Conductance in Bismuth Ferrite,” *Appl. Phys. Lett.*, **102** [12] 121903 (2013).

169 J. Hlinka, S. Kamba, J. Petzelt, J. Kulda, C.A. Randall, and S.J. Zhang, “Origin of the ‘Waterfall’ Effect in Phonon Dispersion of Relaxor Perovskites.,” *Phys. Rev. Lett.*, **91** [10] 107602 (2003).

170 O. Delaire, J. Ma, K. Marty, A.F. May, M.A. McGuire, M.-H. Du, D.J. Singh, A. Podlesnyak, *et al.*, “Giant Anharmonic Phonon Scattering in PbTe.,” *Nat. Mater.*, **10** [8] 614–619 (2011).

171 K. Uchino, “Relaxor Ferroelectrics,” *J. Ceram. Soc. Japan*, **99** [1] 829–835 (1991).

172 R.F. Janninck and D.H. Whitmore, “Electrical Conductivity and Thermoelectric Power of

Niobium Dioxide," *J. Phys. Chem. Solids.*, **27** 1183–1187 (1966).

173 A.B. Kuzmenko, "Kramers-Kronig Constrained Variational Analysis of Optical Spectra," *Rev. Sci. Instrum.*, **76** [8] 083108 (2005).

174 N.E. Brown, S.M. Swapp, C.L. Bennett, and A. Navrotsky, "High-Temperature X-ray Diffraction: Solutions to Uncertanties in Temperature and Sample Position," *J. Appl. Crystallogr.*, **26** 77–81 (1993).

175 A.S. Bhalla, R. Guo, L.E. Cross, G. Burns, F.H. Dacol, and R.R. Neurgaonkar, "Glassy Polarization in the Ferroelectric Tungsten Bronze (Ba,Sr)Nb_2O_6," *J. Appl. Phys.*, **71** [11] 5591–5595 (1992).

176 C.S. Dandeneau, T.W. Bodick, R.K. Bordia, and F.S. Ohuchi, "Thermoelectric Properties of Reduced Polycrystalline $Sr_{0.5}Ba_{0.5}Nb_2O_6$ Fabricated Via Solution Combustion Synthesis," *J. Am. Ceram. Soc.*, **96** [7] 2230–2237 (2013).

177 L. Yi, L. Jian, W. Chun-Lei, S. Wen-Bin, Z. Yuan-Hu, L. Ji-Chao, and M. Liang-Mo, "Thermoelectric Properties of $Sr_{0.61}Ba_{0.39}Nb_2O_{6-\delta}$ Ceramics in Different Oxygen-Reduction Conditions," *Chinese Phys. B*, **24** [4] 047201 (2015).

178 C.S. Dandeneau, Y. Yang, B.W. Krueger, M.A. Olmstead, R.K. Bordia, and F.S. Ohuchi, "Site Occupancy and Cation Binding Sites in Reduced Polycrystalline $Sr_xBa_{1-x}Nb_2O_6$," *Appl. Phys. Lett.*, **104** 101607 (2014).

179 D. Emin, "Optical Properties of Large and Small Polarons and Bipolarons," *Phys. Rev. B*, **48** [18] 13691–13702 (1993).

180 S. Uchida, T. Ido, H. Takagi, T. Arima, Y. Tokura, and S. Tajima, "Optical Spectra of $La_{2-x}Sr_xCuO_4$: Effect of Carrier Doping on the Electronic Structure of the CuO_2 Plane," *Phys. Rev. B*, **43** [10] 7942–7954 (1991).

181 J.L.M. van Mechelen, D. van der Marel, C. Grimaldi, A.B. Kuzmenko, N.P. Armitage, N. Reyren, H. Hagemann, and I.I. Mazin, "Electron-Phonon Interaction and Charge Carrier

Mass Enhancement in $SrTiO_3$," *Phys. Rev. Lett.*, **100** [22] 226403 (2008).

182 T. Zhao, Z.-H. Chen, F. Chen, H.-B. Lu, G.-Z. Yang, and H.-S. Cheng, "Electrical and Optical Properties of Strongly Reduced Epitaxial $BaTiO_{3-x}$ Thin Films," *Appl. Phys. Lett.*, **77** [26] 4338 (2000).

183 J. Hwang, T. Kolodiazhnyi, J. Yang, and M. Coullard, "Doping and Temperature Dependent Optical Properties of Reduced $BaTiO_{3-\delta}$," *Phys. Rev. B*, **82** 214109 (2010).

184 C.N. Berglund and H.J. Braun, "Optical Absorption in Single-Domain Ferroelectric Barium Titanate," *Phys. Rev.*, **164** [2] 790–799 (1967).

185 Y. Li, J. Liu, Y. Hou, Y. Zhang, Y. Zhou, W. Su, Y. Zhu, J. Li, *et al.*, "Thermal Conductivity and Thermoelectric Performance of $Sr_xBa_{1-x}Nb_2O_6$ Ceramics at High Temperatures," *Scr. Mater.*, **109** 80–83 (2015).

186 V. V. Shvartsman, W. Kleemann, T. Łukasiewicz, and J. Dec, "Nanopolar Structure in $Sr_xBa_{1-x}Nb_2O_6$ Single Crystals Tuned by Sr/Ba Ratio and Investigated by Piezoelectric Force Microscopy," *Phys. Rev. B*, **77** [5] 054105 (2008).

187 K.L.I. Kobayashi, Y. Kato, Y. Katayama, and K.F. Komatsubara, "Carrier-concentration-dependent phase transition in SnTe," *Phys. Rev. Lett.*, **37** [12] 772–774 (1976).

188 I. Henning, M. Mertig, R. Plath, G. Pompe, E. Heganbarth, and R. Schalge, "Glass-Like Behavior of $Sr_{1-x}Ba_xNb_2O_6$ (SBN) Single Crystals Demonstrated by Heat Capacity Measurements," *Phys. Status Solidi*, **73** K105–K109 (1982).

189 E. Gorham-Bergeron and D. Emin, "Phonon-Assisted Hopping Due to Interaction with Both Acoustical and Optical Phonons," *Phys. Rev. B*, **15** [8] 3667–3680 (1977).

190 S.T. Liu and L.E. Cross, "Primary Pyroelectricity in Strontium Barium Niobate ($Sr_{0.5}Ba_{0.5}Nb_2O_6$) Single Crystals," *Phys. Status Solidi*, **41** K83–K87 (1977).

191 C.S. Dandeneau, Y. Yang, M.A. Olmstead, R.K. Bordia, and F.S. Ohuchi, "Polaronic Conduction and Anderson Localization in Reduced Strontium Barium Niobate," *Appl.*

Phys. Lett., **107** [23] 232901 (2015).

192 C. David, A. Tunyagi, K. Betzler, and M. Wöhlecke, “Compositional Dependence of Optical and Vibrational Properties of Strontium Barium Niobate ($Sr_xBa_{1-x}Nb_2O_6$),” *Phys. Status Solidi Basic Res.*, **244** [6] 2127–2137 (2007).

193 M. Cutler and N.F. Mott, “Observation of Anderson Localization in an Electron Gas,” *Phys. Rev.*, **181** 1336–1340 (1969).

194 M.D. Ewbank, R.R. Neurgaonkar, W.K. Cory, and J. Feinberg, “Photorefractive Properties of Strontium-Barium Niobate,” *J. Appl. Phys.*, **62** [2] 374–380 (1987).

195 S. Sakamoto and T. Yazaki, “Anomalous Electro-Optic Properties of Ferroelectric Strontium Barium Niobate and Their Device Applications,” *Appl. Phys. Lett.*, **22** [9] 429–431 (1973).

196 J.G. Carrio, Y.P. Mascarenhas, W. Yelon, I.A. Santos, D. Garcia, and J.A. Eiras, “Structure Refinement of $(Sr,Ba)Nb_2O_6$ Ceramic Powder from Neutron and X-Rays Diffraction Data,” *Mater. Res.*, **5** [1] 57–62 (2002).

197 S.C. Abrahams, P.B. Jamieson, and J.L. Bernstein, “Ferroelectric Tungsten Bronze-Type Crystal Structures. III. Potassium Lithium Niobate $K_{6-x-y}Li_{4+x}Nb_{10+y}O_{30}$,” *J. Chem. Phys.*, **54** [6] 2355 (1971).

198 P.B. Jamieson, S.C. Abrahams, and J.L. Bernstein, “Ferroelectric Tungsten Bronze-Type Crystal Structures. II. Barium Sodium Niobate $Ba_{(4+x)}Na_{(2-2x)}Nb_{10}O_{30}$,” *J. Chem. Phys.*, **50** 4352 (1969).

199 X. Zhu, M. Fu, M.C. Stennett, P.M. Vilarinho, I. Levin, C.A. Randall, J. Gardner, F.D. Morrison, *et al.*, “A Crystal-Chemical Framework for Relaxor versus Normal Ferroelectric Behavior in Tetragonal Tungsten Bronzes,” *Chem. Mater.*, **27** [9] 3250–3261 (2015).

200 Y. Chang, S. Lee, S. Poterala, C.A. Randall, and G.L. Messing, “A Critical Evaluation of Reactive Templated Grain Growth (RTGG) Mechanisms in Highly [001] Textured

$Sr_{0.61}Ba_{0.39}Nb_2O_6$ Ferroelectric-Thermoelectrics," *J. Mater. Res.*, **26** [24] 3044–3050 (2011).

201 T. Kolodiazhnyi, H. Sakurai, O. Vasylkiv, H. Borodianska, and Y. Mozharivskyj, "Abnormal Thermal Conductivity in Tetragonal Tungsten Bronze $Ba_{6-x}Sr_xNb_{10}O_{30}$," *Appl. Phys. Lett.*, **104** [11] 111903 (2014).

202 C.S. Dandeneau, "Defect Chemistry and Thermoelectric Behavior of n-type $(Sr_xBa_{1-x})Nb_2O_6$"; University of Washington, 2015.

203 J.R. Carruthers and M. Grasso, "Phase Equilibria Relations in the Ternary System BaO-SrO-Nb_2O_5," *J. Electrochem. Soc.*, **117** [11] 1426–1430 (1970).

204 C. Nikasch and M. Gobbels, "Phase Relations and Lattice Parameters in the System SrO-BaO-Nb_2O_5 Focusing on SBN $(Sr_xBa_{1-x}Nb_2O_6)$," *J. Cryst. Growth*, **269** [2-4] 324–332 (2004).

205 A.W. Sleight, "The Crystal Structure of $Nb_{16}W_{18}O_{94}$, a Member of a $(MeO)_xMeO_3$ Family of Compounds," *Acta Chem. Scand.*, **20** [4] 1102–1112 (1966).

206 C.P. Heinrich, M. Schrade, G. Cerretti, I. Lieberwirth, P. Leidich, A. Schmitz, H. Fjeld, E. Mueller, *et al.*, "Tetragonal Tungsten Bronzes $Nb_{8-x}W_{9+x}O_{47-\delta}$: Optimization Strategies and Transport Properties of a New n-Type Thermoelectric Oxide," *Mater. Horiz.*, **2** 519–527 (2015).

207 G. Svensson, "X-Ray Diffraction and Electron Microscopy Studies of New Reduced Phases in the Ba-Nb-O System," *Solid State Ionics*, **32** 126–133 (1989).

208 G. Svensson, "$Ba_2Nb_5O_9$ - An Intergrowth of $BaNbO_3$ (Perovskite) and NbO," *Mat. Res. Bull.*, **23** 437–446 (1988).

209 G. Svensson, "HREM Studies of Introgrwoth Between NbO and Perovskite in the Ba,Sr and K-Nb-O Systems," *Micros. Microanal. Microstruct.*, **1** 343–356 (1990).

210 V.M. Zhukovsky and A.L. Podkorytov, "Investigation of s,p,d-Element Niobated and

Their Solid Solution Formation Processes by Thermal Analysis," *J. Therm. Anal. Calorim.*, **60** 523–534 (2000).

211 J. Chan, "Study of Filled Tungsten Bronze Strontium Barium Niobate for Thermoelectric Applicaitons;" The Pennsylvania State University, 2016.

212 Y. Li, J. Liu, C. Wang, W. Su, Y. Zhu, J. Li, and L. Mei, "Effects of Oxygen-Reduction on Thermoelectric Properties of $Sr_{0.61}Ba_{0.39}Nb_2O_6$ Ceramics," *Mater. Sci. Forum,* **787** 210–214 (2014).

213 C. Yu, M.L. Scullin, M. Huijben, R. Ramesh, and A. Majumdar, "Thermal Conductivity Reduction in Oxygen-Deficient Strontium Titanates," *Appl. Phys. Lett.*, **92** [19] 191911 (2008).

214 Y. Li, J. Liu, Y. Zhang, Y. Zhou, J. Li, W. Su, J. Zhai, H. Wang, *et al.*, "Enhancement of Thermoelectric Performance of $Sr_{0.7}Ba_{0.3}Nb_2O_{6-\delta}$ Ceramics by Lanthanum Doping," *Ceram. Int.*, **42** 1128–1132 (2016).

215 J. Martin, W. Wong-Ng, and M.L. Green, "Seebeck Coefficient Metrology: Do Contemporary Protocols Measure Up?," *J. Electron. Mater.*, **44** [6] 1998–2006 (2015).

216 J.A. Bock, S. Lee, S. Trolier-McKinstry, and C.A. Randall, "Metallic-like to Nonmetallic Transitions in a Variety of Heavily Oxygen Deficient Ferroelectrics," *Appl. Phys. Lett.*, **107** [9] 092902 (2015).

217 T. Tsubota, M. Ohtaki, K. Eguchi, and H. Arai, "Thermoelectric Properties of Al-Doped ZnO as a Promising Oxide Material for High-Temperature Thermoelectric Conversion," *J. Mater. Chem.*, **7** 85–90 (1997).

218 A.J. Bosman and H.J. van Daal, "Small-Polaron Versus Band Conduction in Some Transition-Metal Oxides," *Adv. Phys.*, **19** [77] 1–117 (1970).

219 I. Levin, M.C. Stennett, G.C. Miles, D.I. Woodward, A.R. West, and I.M. Reaney, "Coupling Between Octahedral Tilting and Ferroelectric Order in Tetragonal Tungsten

Bronze-Structured Dielectrics," *Appl. Phys. Lett.*, **89** [12] 122908 (2006).

220 J. Gardner and F.D. Morrison, "A-site Size Effect in a Family of Unfilled Ferroelectric Tetragonal Tungsten Bronzes: $Ba_4R_{0.67}Nb_{10}O_{30}$(R = La, Nd, Sm, Gd, Dy and Y)," *Dalt. Trans.*, **43** 11687–11695 (2014).

221 M. Imada, A. Fujimori, and Y. Tokura, "Metal-Insulator Transitions," *Rev. Mod. Phys.*, **70** [4] 1039–1263 (1998).

222 J.B. Torrance, P. Lacorre, A.I. Nazzal, E.J. Ansaldo, and C. Niedermayer, "Systematic Study of Insulator-Metal Transitions in Perovskites $RNiO_3$ (R=Pr,Nd,Sm,Eu) Due to Closing of Charge-Transfer Gap," *Phys. Rev. B*, **45** [14] 8209–8212 (1992).

223 X.L. Zhu, K. Li, and X.M. Chen, "Ferroelectric Transition and Low-Temperature Dielectric Relaxations in Filled Tungsten Bronzes," *J. Am. Ceram. Soc.*, **97** [2] 329–338 (2014).

224 H.A. Graetsch, J. Schreuer, M. Burianek, and M. Mühlberg, "Thermally Induced Structural Changes in Incommensurate Calcium Barium Niobate $Ca_{0.28}Ba_{0.72}Nb_2O_6$ (CBN28)," *J. Solid State Chem.*, **196** 255–266 (2012).

225 D.C. Arnold and F.D. Morrison, "B-cation Effects in Relaxor and Ferroelectric Tetragonal Tungsten Bronzes," *J. Mater. Chem.*, **19** [36] 6485 (2009).

226 S.B. Qadri, J.A. Bellotti, A. Garzarella, and D.H. Wu, "Anisotropic Thermal Expansion of Strontium Barium Niobate," *Appl. Phys. Lett.*, **86** [25] 251914 (2005).

227 F. Prokert, "Neutron Scattering Studies on Strontium Barium Niobate," *Phys. Status Solidi*, **113** 239–252 (1982).

228 H. Uchihashi, N. Tohge, and T. Minami, "Preparation of Amorphous Al_2O_3 Thin Films from Stabilized Al-Alkoxides by the Sol-Gel Method," *Nippon Seramikkusu Kyokai Gakujutsu Ronbunshi*, **97** [3] 396–99 (1989).

229 R. Nakamura, T. Toda, S. Tsukui, M. Tane, M. Ishimaru, T. Suzuki, and H. Nakajima,

"Diffusion of Oxygen in Amorphous Al_2O_3, Ta_2O_5, and Nb_2O_5," *J. Appl. Phys.*, **116** [3] 033504 (2014).

230 T. Nabatame, T. Yasuda, M. Nishizawa, M. Ikeda, T. Horikawa, and A. Toriumi, "Comparative Studies on Oxygen Diffusion Coefficients for Amorphous and γ-Al_2O_3 Films using ^{18}O Isotope," *Jpn. J. Appl. Phys.,* **42** 7205–7208 (2003).

231 W.D. Kingery, "Density and Thermal Expansion of Crystals;" pp. 467–473 in *Introd. To Ceram.*, 1st ed. John Wiley & Sons, Inc., 1960.

232 J.B. Wachtman, T.G. Scuderi, and G.W. Cleek, "Linear Thermal Expansion of Aluminum Oxide and Thorium Oxide from 100 to 1100K," *J. Am. Ceram. Soc.,* **45** [7] 319–323 (1962).

233 F. Di Fonzo, D. Tonini, A. Li Bassi, C.S. Casari, M.G. Beghi, C.E. Bottani, D. Gastaldi, P. Vena, *et al.*, "Growth Regimes in Pulsed Laser Deposition of Aluminum Oxide Films," *Appl. Phys. A,* **93** [3] 765–769 (2008).

234 T. Maruyama and T. Nakai, "Aluminum Oxide Thin Films Prepared by Chemical Vapor Deposition From Aluminum 2-Ethylhexanoate," *Appl. Phys. Lett.*, **58** [19] 2079–80 (1991).

235 W. Koh, S.-J. Ku, and Y. Kim, "Chemical Vapor Deposition of Al_2O_3 Films Using Highly Volatile Single Sources," *Thin Solid Films,* **304** 222–224 (1997).

236 M. Aguilar-Frutis, M. Garcia, C. Falcony, G. Plesch, and S. Jimenez-Sandoval, "A Study of the Dielectric Characteristics of Aluminum Oxide Thin Films Deposited by Spray Pyrolysis from $Al(acac)_3$," *Thin Solid Films,* **389** 200–206 (2001).

237 S. Maniv and W.D. Westwood, "Discharge Characteristics for Magnetron Sputtering of Al in Ar and Ar/O_2 Mixtures," *J. Vac. Sci. Technol.*, **17** [3] 743 (1980).

238 T. Olding, M. Sayer, and D. Barrow, "Ceramic Sol-Gel Composite Coatings for Electrical Insulation," *Thin Solid Films,* **398-399** 581–586 (2001).

[239] K.R. Murali and P. Thirumoorthy, “Characteristics of Sol-Gel Deposited Alumina Films,” *J. Alloys Compd.*, **500** 93–95 (2010).

[240] C. Jing, X. Zhao, and Y. Zhang, “Sol-Gel Fabrication of Compact, Crack-Free Alumina Film,” *Mater. Res. Bull.*, **42** 600–608 (2007).

[241] Q. Fu, C.-B. Cao, and H.-S. Zhu, “Preparation of Alumina Films From a New Sol–Gel Route,” *Thin Solid Films*, **348** 99–102 (1999).

[242] J.G. Olin, *Capillary Tube Thermal Mass Flow Meters & Controllers A User’s Guide*, (2013).

[243] N. Cusack and P. Kendall, “The Absolute Scale of Thermoelectric Power at High Temperature,” *Proc. Physcial Soc.*, **72** [5] 898–901 (1958).

[244] J. Mackey, F. Dynys, and A. Sehirlioglu, “Uncertainty Analysis for Common Seebeck and Electrical Resistivity Measurement Systems,” *Rev. Sci. Instrum.*, **85** [8] 085119 (2014).

VITA

Jonathan A. Bock

Jonathan Anton Bock was born March 19th 1988 in Jefferson City, Missouri, to Robert and Susan Bock. He attended school at the University of Missouri – Rolla and earned a degree in Ceramic Engineering. Jonathan then went to Penn State to obtain his PhD in Material Science and Engineering while working alongside Clive Randall and Susan Trolier-McKinstry with the goal of studying ferroelectric-based thermoelectrics.